Norwegian Meteorological Institute

METreport

No. 16/2025
ISSN 2387-4201
Meteorology

Analysis of unique measurement data in Gratangen

Observation quality control and model verification

Eirik Mikal Samuelsen, Anna Odh,
Karolina Haraldsson, Sevim Müller-Gulbrandsen

Photo: Eirik Mikal Samuelsen

Norwegian Meteorological Institute

METreport

Title	**Date**
Analysis of unique measurement data in Gratangen. Observation quality control and model verification	August 22, 2025
Section	**Report no.**
Meteorology	16/2025
Authors	**Classification**
Eirik Mikal Samuelsen, Anna Odh, Karolina Haraldsson, Sevim Müller-Gulbrandsen	● Free ○ Restricted
Client	**Client's reference**
Norwegian Research Council	'Multidisiplinary approach for spray icing modelling and decision support in the Norwegian maritime sector' (SPRICE). Grant Number 320843 at NFR, and MET Norway project number is 281570.
Keywords	
sea-spray icing, observations, turbulence, radiation, fluxes, fish farm	

Disciplinary signature

Responsible signature

Abstract

This report presents a detailed evaluation of observation data from a fish farm weather station in Northern Norway, alongside numerical weather prediction output from the Arome Arctic model covering the period from March to November 2023. Parameters analyzed include wind, temperature, pressure, precipitation, turbulent kinetic energy (TKE), heat fluxes, and radiation. All observational variables are compared with model data at 2.5 km horizontal resolution. The findings highlight the importance of accounting for possible disturbances related to the measurement platform, such as the influence of the feeding barge on vertical wind velocity during southwesterly flow. Excluding these disturbances, the remaining parameters show consistent and reliable behavior. The model evaluation indicates a negative bias in temperature, a positive bias in weak wind speeds, a negative bias in strong wind speeds, a negative bias in modelled incoming longwave radiation, and a positive bias in incoming shortwave radiation. Case studies of offshore flow indicate that model limitations related to horizontal resolution and inaccurate representation of land and sea tiles negatively impact the simulation of both TKE and sensible heat flux. Finally, the analysis suggests that applying an emissivity value of 0.7 in the incoming longwave radiation term in the radiative heat flux calculation applied in the MINCOG spray icing model is appropriate during the cold season. On the other hand, using incoming longwave radiation directly from the Arome Arctic model may improve the accuracy of spray-icing estimates.

Norwegian Meteorological Institute
Org.no 971274042
post@met.no
www.met.no / www.yr.no

Oslo
P.O. Box 43, Blindern
0313 Oslo, Norway
T. +47 22 96 30 00

Bergen
Allégaten 70
5007 Bergen, Norway
T. +47 55 23 66 00

Tromsø
P.O. Box 6314, Langnes
9293 Tromsø, Norway
T. +47 77 62 13 00

Contents

1 Introduction

The research project "Multidisplinary approach for spray icing modelling and decision support in the Norwegian maritime sector" (SPRICE) which is funded by the Research Council of Norway (RCN) are running from 2021 to 2025. One of the goals of the project is to measure parameters that are relevant for sea-spray-icing modelling on a fish farm in order to refine the operational ship-icing model MINCOG (Samuelsen et al., 2017) currently applied at MET Norway to be applicable for fish-farm icing modelling. For that reason a full scale weather station was mounted in March 2023 by MET Norway in Gratangen in Northern Norway in strong collaboration with the fish farming company Gratanglaks and UiT - The Arctic University of Norway. Firstly, a WS600-UMB Smart Weather Sensor has been mounted on a feeding barge in Skjærvika approximately at N68.73 E17.24 (Figure 1) in order to measure atmospheric variables like temperature, humidity, precipitation, air pressure, and horizontal wind. Secondly, a Thies Clima

Figure 1: *A map showing the position of the measurement site in Northern Norway. Source: The Norwegian Mapping Authority.*

3D ultrasonic anemometer is mounted on the same barge in order to measure the three-dimensional wind fluctuations and turbulence. Furthermore, a CNR4 Net Radiometer from Kipp & Zonen is mounted to measure radiation from the atmosphere and from the sea surface.

An Obscape Buoy 400 is also mounted outside the fish cages in order to measure the wave height, wave period, and wave direction. Finally, horizontal sea spray and rain flux are measured both on the fish rings and the feed barge using a maritime rain gauge with a novel design for the horizontal direction (Dhar et al., 2024). However, the wave data and the spray data are not considered in this report.

To the knowledge of the authors, some of these parameters measured at this station, like vertical wind, turbulence, longwave radiation, and shortwave radiation, have never been measured regularly before at a stationary position at a location just above the sea surface in Northern Norway. Thus, this report aims to evaluate the current data collected first from the period 15 March to 30 June 2023 and later from the period 1 July to 14 November 2023. Furthermore, the operational model Arome Arctic of the Norwegian Meteorological Institute is verified against these data (Müller et al., 2017; Køltzow et al., 2019).

2 Instrumentation

Most of the instruments are mounted on the feeding barge at a height of approximately 22 m above the mean sea level in calm conditions.

2.1 All weather sensor (AWS)

The WS600-UMB Smart Weather Sensor (Figure 2) is an All-in-One or All weather sensor (AWS) measuring temperature (T), relative humidity (RH), precipitation intensity ($\mathrm{RR_{int}}$), precipitation type ($\mathrm{RR_{type}}$), air pressure (p), horizontal wind direction (DD), and horizontal wind speed (FF). The precipitation measurements are conducted by using Doppler radar technology. The station has a built-in compass which means that the outputted data shows the wind direction relative to magnetic north instead of true north. For air pressure a height correction must be realized in order to measure the air pressure relative to the mean sea level (MSLP) instead of the station pressure. The data output is every minute. More details about the various sensors may be found in Lufft (2022).

Figure 2: *All weather sensor (AWS) with outputs like temperature (T), relative humidity (RH), mean sea level pressure (MSLP), horizontal wind direction (DD), horizontal wind speed (FF), precipitation intensity (RR_{int}), and precipitation type (RR_{type}). Photo: Eirik Mikal Samuelsen.*

2.2 3D sonic anemometer

The Thies Clima 3D ultrasonic anemometer (Figure 3), here referred to as a 3D sonic anemometer, measures wind speed in three directions (u, v, w) with a time resolution of one second, which means that both the horizontal (u', v') and the vertical wind fluctuations (w') are measured. In addition, sonic temperature (T_s) is measured. From the wind and sonic-temperature fluctuations, turbulent kinetic energy (TKE), momentum fluxes, and heat fluxes, e.g. the sonic heat flux ($\overline{w'T_s'}$), may be derived. For more details about the 3D sonic anemometer, the reader is referred to the manual of the instrument (Thies, 2022).

2.3 Net Radiometer

The CNR4 Net Radiometer from Kipp & Zonen (Figure 4) measures incoming shortwave (SW) and longwave (LW) radiation from above and below. The radiometer is mounted on the railing of the feed barge in such a manner that the incoming radiation from below is planned to come mainly from the sea surface. However, since the vertical distance to the sea surface is 22 m , there might be interference of radiation from other surfaces as well, and the evaluation will show whether the placement of the sensor is good enough to serve the purpose of having a radiation signal mainly from the sea. The incoming radiation from above is mainly from the atmosphere, but also here there might be interference from

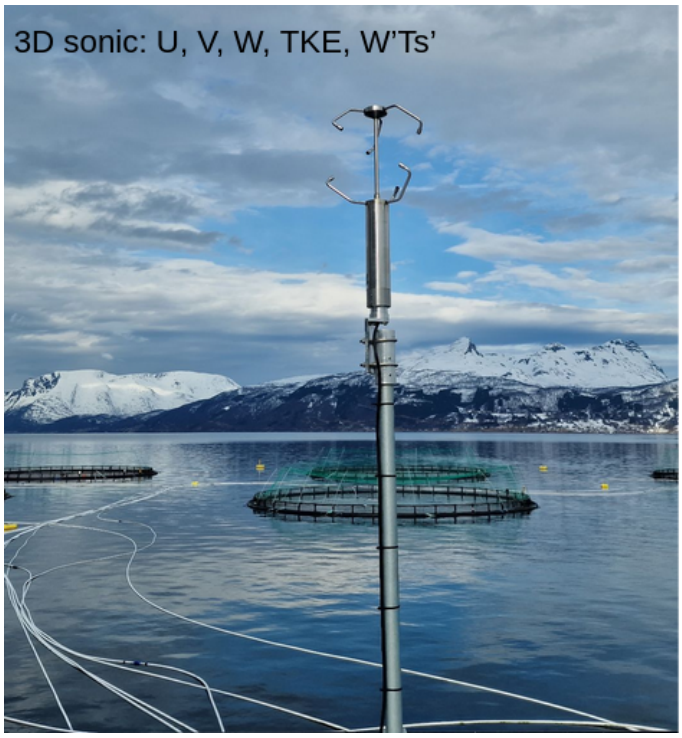

Figure 3: *3D sonic anemometer with outputs like wind speed in three directions (u, v, w), turbulent kinetic energy (TKE), and the sonic heat flux ($\overline{w'T_s'}$). Photo: Eirik Mikal Samuelsen.*

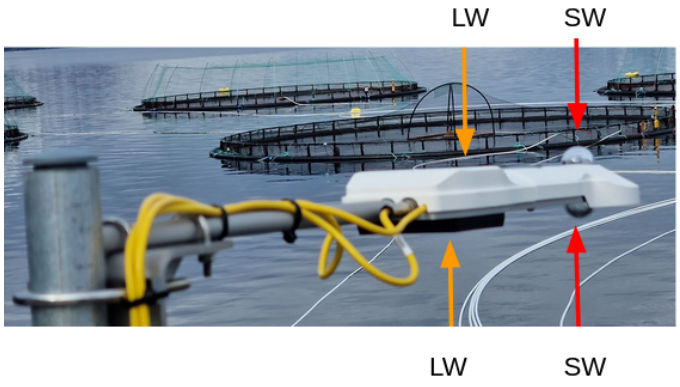

Figure 4: *Radiometer measuring incoming shortwave (SW) and longwave (LW) radiation from above and below. Photo: Eirik Mikal Samuelsen.*

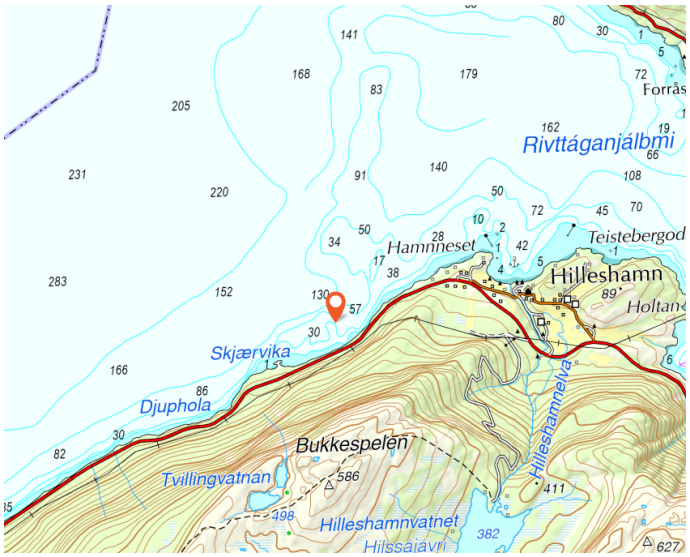

Figure 5: *Zoomed in map of measurement location. Source: The Norwegian Mapping Authority.*

other objects as well. For instance there is a steep mountain just southeast of the location that might affect particularly the incoming shortwave radiation from above (Figure 5). The incoming radiation from the sea is further in the report called "outgoing" longwave radiation.

3 Methods

The observation quality control is done by plotting and inspecting the parameters outputted by the three instruments (Figures 2, 3, and 4). Firstly, the data are analysed monthly, and secondly, over the first time period from 15 March 2023 until 30 June 2023, and later for the period from 1 July to 14 November 2023. Some shorter time periods and cases are also inspected in more detail for investigating interesting correlations between some of the parameters.

3.1 Wind speed, wind gust, and wind direction

Horizontal wind speed is calculated from both the 3D sonic anemometer horizontal wind components and the wind components of the AWS. The wind speed is calculated from u (west-east) and v (south-north) as FF $= \sqrt{\overline{u}^2 + \overline{v}^2}$, where $\overline{u}$ is the 10 minute running average of u and $\overline{v}$ is the 10 minute running average of v. The instantaneous horizontal wind speed, often referred to as wind gust when $u > \overline{u}$, is calculated as FG $= \sqrt{u^2 + v^2}$. The wind direction (DD) is calculated from u and v and presented in degree cardinal coordinates by using the four-quadrant arctangent function, named atan2, in MATLAB (The MathWorks Inc., 2023) in the following manner:

$$\begin{aligned} \text{DD} &= \left(\text{atan2}(u,v) \times \frac{180.0}{\pi} \right) + 180, \quad && \text{for } (u,v) \neq (0,0) \\ \text{DD} &= 0, && \text{for } (u,v) = (0,0) \end{aligned} \tag{1}$$

The vertical wind speed is calculated as the 10 minute running average of the absolute value of the vertical wind component ($\overline{|w|}$), but also the 10 minute average of the vertical wind component ($\overline{w}$) is calculated with an on average positive or negative value.

3.2 TKE

The turbulence kinetic energy (TKE) is calculated from the wind components u, v, and w retrieved from the 3D sonic anemometer with the following equation:

$$\text{TKE} = \frac{1}{2} \left(\overline{(u')^2} + \overline{(v')^2} + \overline{(w')^2} \right) \tag{2}$$

where $u' = u - \overline{u}$, $v' = v - \overline{v}$, and $w' = w - \overline{w}$. Here $\overline{u}$, $\overline{v}$, and $\overline{w}$ are the 10 minute running averages of u, v, and w. Moreover, $\overline{(u')^2}$, $\overline{(v')^2}$, and $\overline{(w')^2}$ are the variances of the wind components u, v, and w during the same time period. In aviation forecasting at MET Norway the square root of TKE is commonly presented as a measure of turbulence intensity (Mathisen, 2023). Hence, the observed $\sqrt{\text{TKE}}$ is also presented in this report and compared with the model output of $\sqrt{\text{TKE}}$ from the Arome Arctic model.

3.3 Dry temperature

The 3D sonic anemometer outputs the sonic temperature (T_s) given as (Thies, 2022):

$$T_s = T_d \left(1 + 0.30 \times \frac{e}{p}\right) \tag{3}$$

where T_d is the dry temperature, e is the vapour pressure, and p is the air pressure. $e = \frac{\text{RH}}{100\%} \times e_s$, where RH is the relative humidity in percent and e_s is the saturation vapor pressure. e_s in hPa is calculated from Bolton (1980):

$$e_s = 6.112 \times \exp\left(\frac{17.67T}{T + 243.5}\right) \tag{4}$$

where T is the air temperature in °C with an accuracy of 0.1% for $-30°\text{C} \leq T \leq 35°\text{C}$ (Bolton, 1980). By using humidity measurements from the AWS, T_d is derived from Eq. (3) through an iterative method. The dry temperature calculated by this method, is then compared to the dry temperature outputted by the AWS, by finding the absolute mean difference and mean difference between the parameters.

3.4 Kinematic heat flux and buoyancy flux

The vertical kinematic heat flux is calculated as $\overline{w'T'}$, where $w' = w - \overline{w}$ and $T' = T - \overline{T}$, where $\overline{w}$ and $\overline{T}$ are the 10 minute running averages of the temperature (T) and the vertical wind component (w). $\overline{w'T'}$ is the 10 minute running average of $w'T'$. Since the 3D sonic anemometer measures the sonic temperature (T_s), the output from the 3D sonic anemometer is the sonic heat flux ($\overline{w'T_s'}$). It is here assumed that the kinematic heat flux is approximately equal to the sonic heat flux $\overline{w'T'} \approx \overline{w'T_s'}$ which is an acceptable assumptions in relatively cold and dry conditions. The buoyancy flux (BF) is found by multiplying the kinematic heat flux with the factor g/T_s, where g is the gravitational acceleration.

$$\text{BF} = \frac{g}{T_v}\overline{w'\theta_v'} \approx \frac{g}{T_s}\overline{w'T_s'} \tag{5}$$

Here, T_v is the virtual temperature and θ_v is the virtual potential temperature.

3.5 Sensible heat flux

The sensible heat flux is calculated as

$$Q_s = \rho_a c_p \overline{w'T'} \tag{6}$$

where $\rho_a = 1.2$ kg m^{-3} is the density of the atmosphere and is for simplification set to a constant, $c_p = 1004$ J kg^{-1}K^{-1} is the specific heat capacity for air at constant pressure, and $\overline{w'T'}$ is the kinematic heat flux as explained in Section 3.4.

3.6 Incoming longwave radiation

The incoming longwave radiation is measured by the upper pyrgeometer on the net radiometer and is compared to the incoming longwave radiation calculated using the Stefan-Boltzmann law:

$$\mathrm{LW_{in}} = \varepsilon \times \sigma T^4 \tag{7}$$

where ε is the emissivity, σ is the Stefan-Boltzmann constant, and T is the temperature in Kelvin. For this calculation the dry temperature (T_d) derived from the 3D sonic anemometer and the humidity from the AWS is applied. In order to investigate the validity of the parameterization of longwave radiation applied in the operational spray-icing model MINCOG (Samuelsen et al., 2017; Samuelsen, 2017), the measured $\mathrm{LW_{in}}$ is compared to the calculated value from Eq. (7). In the operational settings an on average emissivity of 0.7 is assumed for the atmosphere in the cold season, but also an emissivity of 1 is applied in the literature (Lozowski et al., 2000). Finally, an optimal emissivity ($\varepsilon_{\mathrm{optimal}}$) is derived by finding the smallest mean absolute error (MAE) between a range of ε used in Eq. (7) and the output from the upper pyrgeometer.

3.7 Estimated SST

In order to test whether the outgoing longwave radiation from the sea could be applied for sea-surface temperature (SST) estimation, Eq. (7) is rearranged with SST as temperature:

$$\mathrm{SST} = \left(\frac{\mathrm{LW_{up}}}{\varepsilon \sigma} \right)^{\frac{1}{4}} \tag{8}$$

LW_{up} is the outgoing longwave radiation from the pyrgeometer. An ocean emissivity (ε) of approximately 0.96 is applied in the calculations which is in the lower range of the ocean-emissivity values presented in Newman et al. (2005).

3.8 Model verification

Model verification is done by comparing the measured parameters as well as the calculated parameters to model data from the Arome Arctic model. Since the model has one output every full hour UTC-time, the parameters are verified at each full hour output. However, for simplicity, it is assumed that the model UTC time is the same as the observed local time (CET or CEST depending on time of the year) since the difference between UTC and local time is only two hours during summer time and one hour during winter time. Furthermore, the weather station is located at 22 m above sea level (MASL) and the model data are either linearly interpolated between the two lowermost model levels 64 and 65 which has an approximate height of 36 m and 12 m. In some cases, such interpolation is not possible, and the parameters are adjusted to fit the station height in a best possible manner. Some parameters are also verified against other model heights for comparison: at 0 m for pressure, at 2 m for temperature and relative humidity, and at 10 m for horizontal wind speed, wind gust, and wind direction. Mean absolute error (MAE), the mean of the absolute value of the difference between the model and the observed parameter, and the mean error or BIAS, the mean value of the difference between the model and the observed parameter, are calculated for most of the parameters. Moreover, the Pearson correlation coefficient, r, is also calculated in the model verification when relevant. For verification of pressure, the observed pressure is compared to a value derived from the hypsometric equation providing:

$$z_{22} - z_0 = \frac{R_d \overline{T_v}}{g} \ln\left(\frac{p_0}{p_{22}}\right) \tag{9}$$

By assuming that the observed sonic temperature at 22 m (T_s) is equal to the mean virtual temperature in the layer between the surface ($z_0 = 0$ m) and 22 m height ($\overline{T_v}$), one can simplify the calculation of pressure at 22 m height to be:

$$p_{22} = \frac{p_0}{\exp\left(z_{22} g/(R_d T_s)\right)} \tag{10}$$

where p_0 is the pressure at sea level from the model, g is the gravitational constant, $z_{22} = 22$ m is the height at the measurement site, and R_d is the gas constant for dry air.

For the verification of relative humidity, the following equation is utilized to find the modelled relative humidity at 22 m height ($\mathrm{RH_{M22}}$):

$$\mathrm{RH_{M22}} = \frac{q_{\mathrm{M22}} p_{\mathrm{M22}}}{0.622 e_s} \tag{11}$$

where q_{M22} is the specific humidity from the model linearly interpolated to 22 m, p_{M22} is the calculated pressure at 22 m in the model, and e_s is the saturated vapor pressure calculated with Eq. (4). In order to find the observed specific humidity (q), the following relationship is applied:

$$q = 0.622 \times \mathrm{RH}\frac{e_s}{p} \tag{12}$$

where RH and p are observational parameters from the AWS. In the operational Arome models including Arome Arctic wind gusts at 10 m height are parameterized in the following manner:

$$\mathrm{FG}_{10\mathrm{m}} = \mathrm{FF}_{10\mathrm{m}} + 3.5 \times \sqrt{\mathrm{TKE}_{20\mathrm{m}}} \tag{13}$$

For the modelled wind gust at the Skjærvika location the following relationship is implemented to find the gust at 22 m:

$$\mathrm{FG}_{M22} = \mathrm{FF}_{M22} + 3.5 \times \sqrt{\mathrm{TKE}_{M22}} \tag{14}$$

where FF_{M22} is the model horizontal wind speed linearly interpolated to 22 m and TKE_{M22} is the model TKE interpolated to 22 m. In contrast to the wind gust parameterization in the operational model, here, all parameters are applied from the same height.

For the verification of the precipitation and radiation data, an hourly mean at each full hour, in mm h^{-1} and W m^{-2}, respectively, are found from the model and the measurement data.

4 Results from 15 March 2023 to 30 June 2023

4.1 Raw data from the three instruments

The raw data of the three wind components and the sonic temperature is plotted in Figure 6 and Figure 7. Here it is apparent that there are periods of strong winds with horizontal wind components above 10 m/s from mid-March until mid-June (Figure 6). It is noticeable that the positive vertical wind component is surprisingly strong, compared to the horizontal components and the negative component of the vertical velocity (w). In addition, it is apparent that the temperature is increasing throughout the period with some distinct cold periods in March, in the beginning of April, in the beginning of May, and also in the beginning of June, with some milder or warmer periods in the end of April, end of May, and particularly in the end of June (Figure 7).

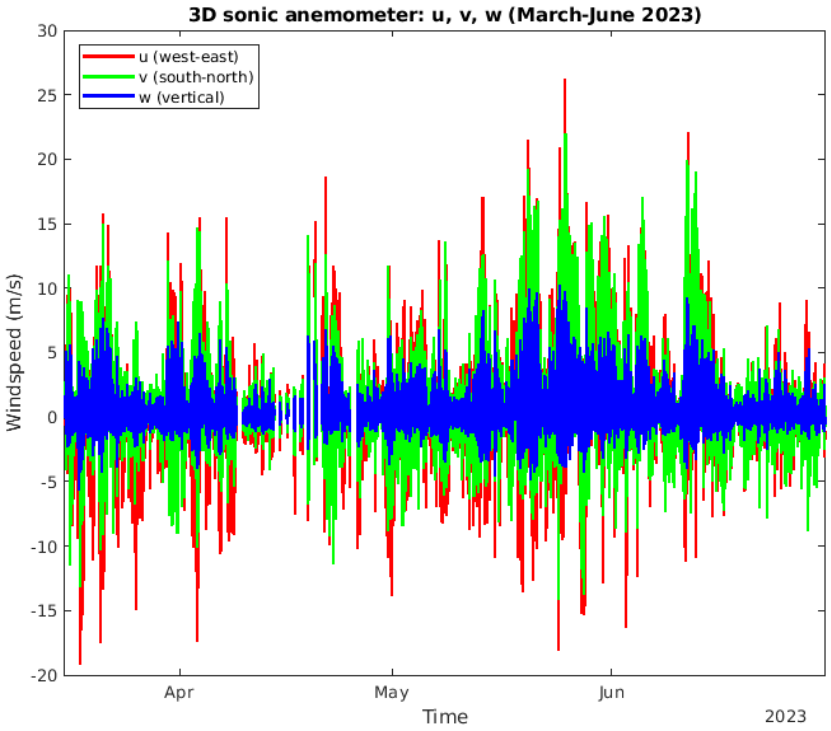

Figure 6: *u (in red), v (in green), and w (in blue) from the 3D sonic anemometer from 15 March 2023 to 30 June 2023.*

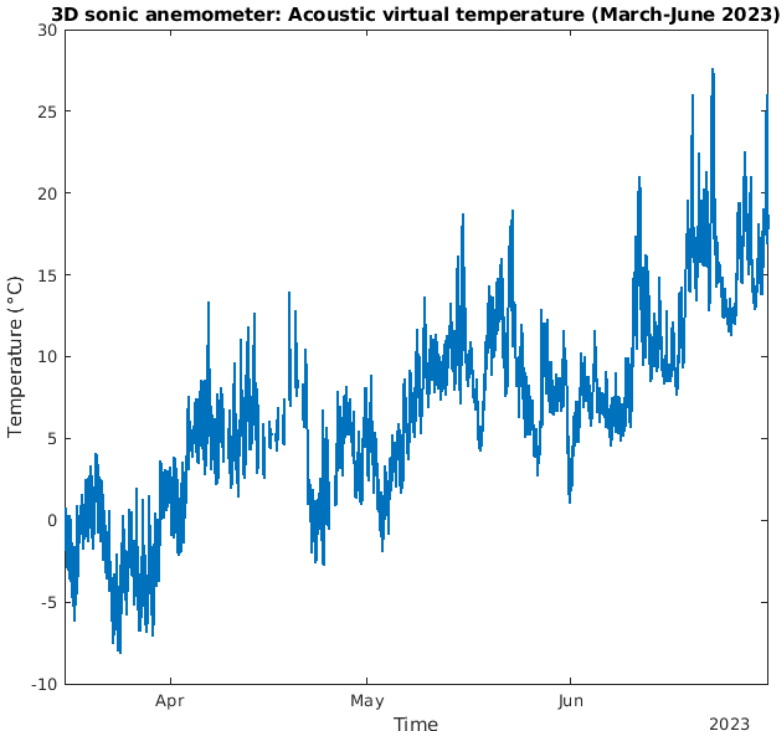

Figure 7: *Acoustic or sonic temperature from the 3D sonic anemometer from 15 March 2023 to 30 June 2023.*

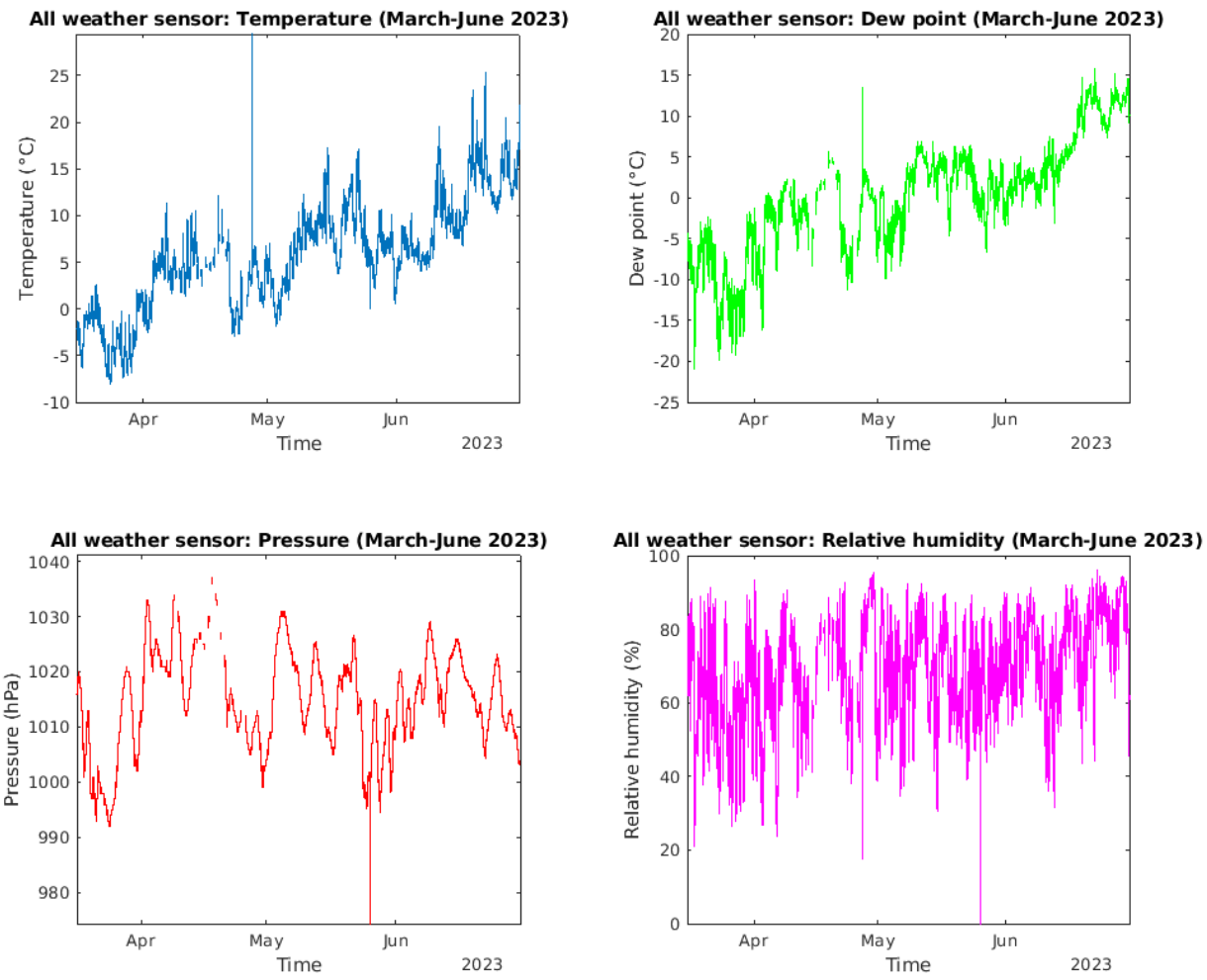

Figure 8: *Temperature (in blue), dew-point temperature (in green), air pressure (in red), and relative humidity (in pink) from the AWS (15 March to 30 June 2023).*

Figure 8 shows the temperature, the dew-point temperature, the air pressure, and the relative humidity from the AWS. It is apparent that the temperature and also in part the dew-point temperature follow the 3D sonic temperature trends from March to June (Figure 7) which strengthens the trustworthiness of the data from both instruments. In addition, the plots show the necessity to do some filtering of the data in order to remove some of the spikes noticeable in Figure 8.

Figure 9 visualizes the longwave radiation and shortwave radiation from the net radiometer together with the temperature and relative humidity from the AWS. As is apparent from Figure 9 some radiation data in April are missing and this should be considered

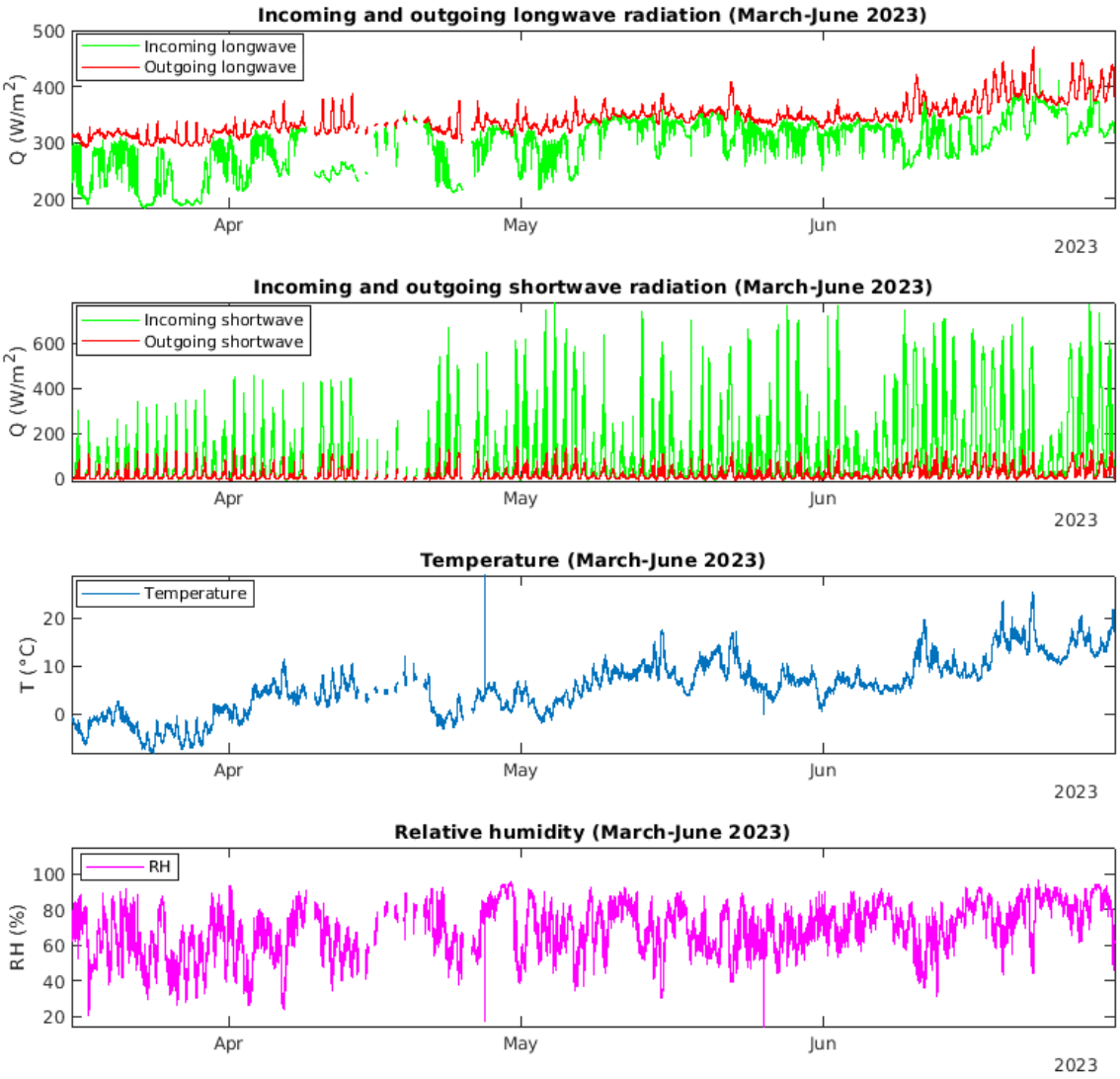

Figure 9: *Longwave radiation and shortwave radiation from the net radiometer, along with temperature and relative humidity from the AWS from 15 March 2023 to 30 June 2023.*

when using the data. Furthermore, Figure 9 shows that the longwave radiation from the sea is mostly higher than the longwave radiation from the atmosphere. There are only a few periods in the end of June in combination with a warm and humid atmosphere that the incoming longwave radiation from the atmosphere is higher than the longwave radiation from the sea. However, it is concluded when estimating the sea-surface temper-

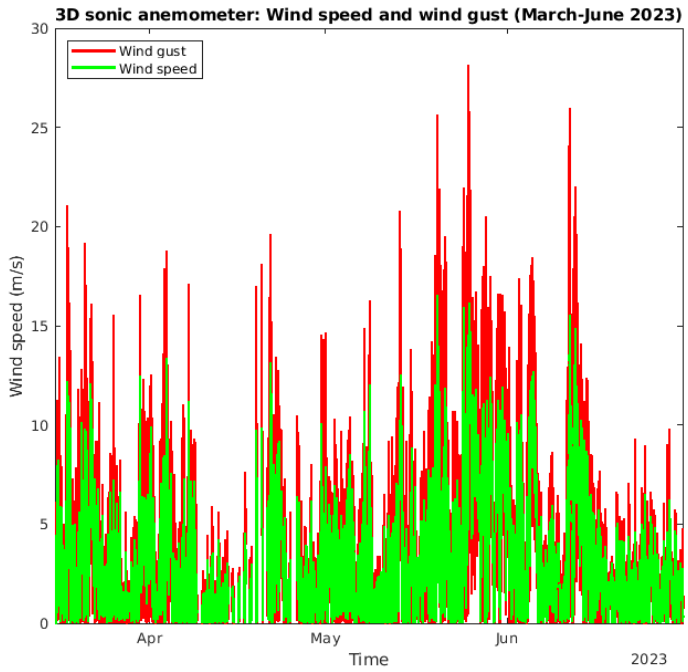

Figure 10: *Horizontal mean wind speed (in green) and instantaneous wind speed or wind gust (in red) during the period 15 March to 30 June 2023.*

ature (SST) in later sections (Section 4.8) that the outgoing radiation measurements are affected by other surfaces than only the sea surface, resulting in an unrealistic high SST in the calculations. This is also apparent from Figure 9 as the outgoing longwave radiation is fluctuating more than the the signal from a pure sea surface should provide with a more constant radiation value throughout the period. For the incoming shortwave radiation it is apparent that there are higher values in May and June than in the beginning of the period in conjunction with a higher sun elevation angle in May and June compared to March and April.

4.2 Horizontal and vertical winds

Figure 10 depicts the 10 minute average horizontal wind speed together with the instantaneous horizontal wind speed derived from the 3D sonic anemometer. The instantaneous wind speed is called wind gust when it is higher than the mean wind speed. Although the measurements indicate that there are no observations with a mean wind speed above 20 m/s, there are several instances with wind gusts above 10 m/s. The relatively large difference between the gust and the mean wind speed indicates quite turbulent conditions,

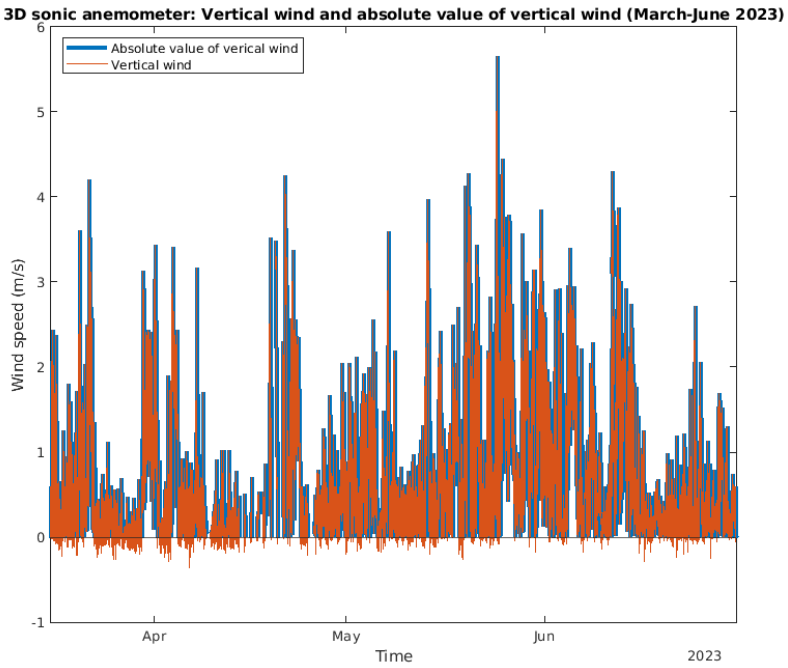

Figure 11: *Vertical wind component (w, in red) and absolute value of vertical wind ($|w|$, in blue) from 15 March to 30 June 2023.*

with a gust factor of above 1.5 under certain conditions.

Figure 11 illustrates the vertical wind component and absolute value of the vertical wind speed from the 3D sonic anemometer. Both from Figure 6 and 11 it is apparent how much larger in absolute value the positive vertical component is, compared to the absolute value of the negative vertical component. This might be related to a positive buoyancy in conditions with unstable static stability, but may also be an effect of strong horizontal wind being lifted towards the sonic anemometer when hitting the feeding barge. For this reason, an investigation of the wind direction along with the vertical wind component is applied. Figure 12 shows the wind direction and vertical wind speed plotted together. Due to large variations in wind direction throughout the period, it is difficult to extract meaningful details from the figure. However, some large-scale signatures are apparent at some instances. In the end of March, where there is a high frequency of winds between 100 and 150 degrees, there are also lower positive values (from 1 m/s and below) of the vertical wind component. Moreover, in the end of May and in the beginning of June there is a period with mostly winds between 200 and 250 degrees, and in this period there is also a high frequency of strong positive vertical velocity (from 2 m/s and above). This result

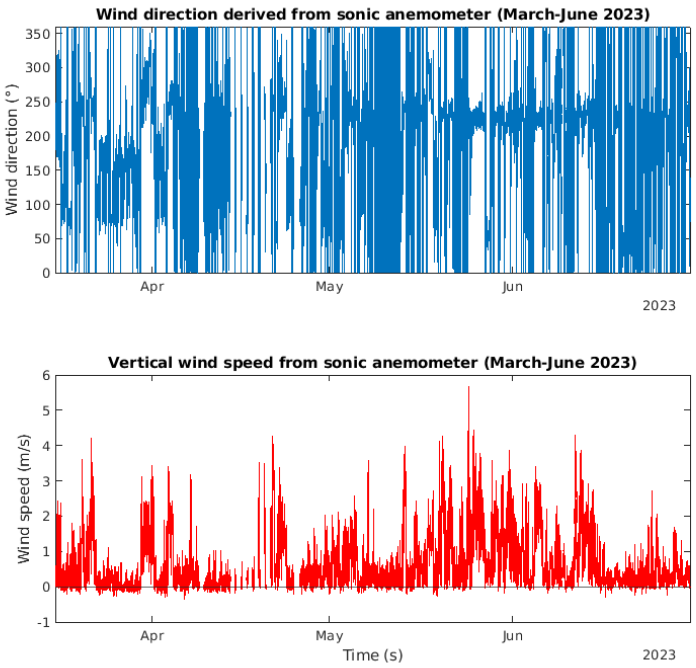

Figure 12: *Wind direction (DD, upper panel) and vertical wind component (w, lower panel) from 15 March to 30 June 2023.*

strengthens the hypothesis that the measured vertical velocities might be influenced by the feeding barge, and that the data are not necessarily representing the vertical velocities in the atmosphere. Thus, in the following section a total of four interesting time periods are examined in greater detail to gain a deeper understanding of the underlying processes.

4.3 Case-based analyses of vertical wind speed

Figures 13, 16, 17, and 19 highlight four interesting time periods correlating the wind direction and the vertical wind gust.

4.3.1 Offshore flow case: 17 and 18 March 2023

In Figure 13, a period with offshore flow is studied in more detail.

An offshore flow is related to mountain waves and downslope winds in the lee of the mountains northeast to southeast of the location (Figures 1 and 5). Thus, the strongest negative velocities are clearly apparent when the wind is between east and northeast (between 50 and 100 degrees) in the end of 17 March 2023 and in the beginning of 18 March 2023. Investigating the flow field of the Arome Arctic model in this particular case, under-

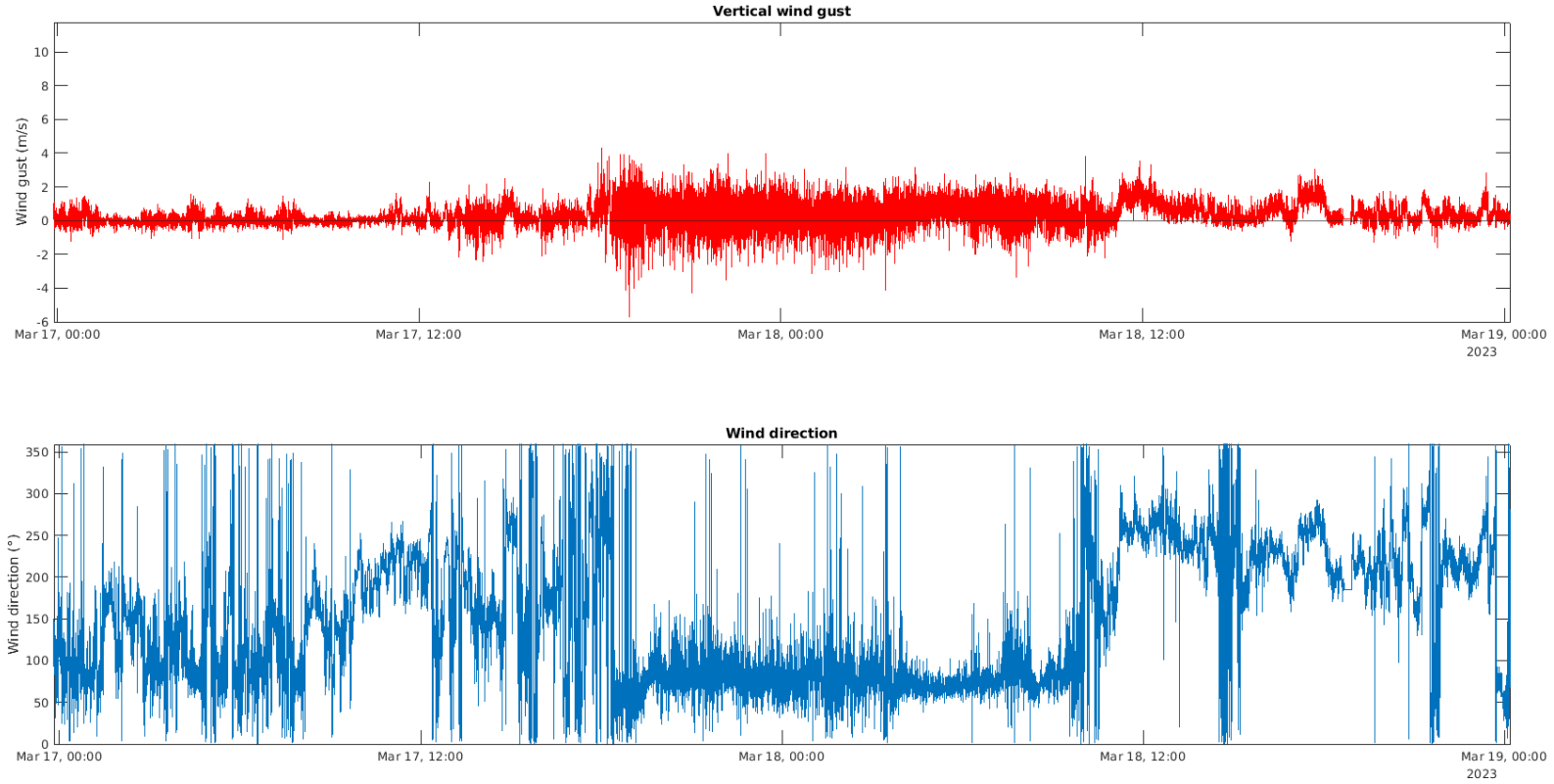

Figure 13: *A case comparison of vertical wind gust (in red, upper panel) and wind direction (in blue, lower panel) during 17 and 18 March 2023.*

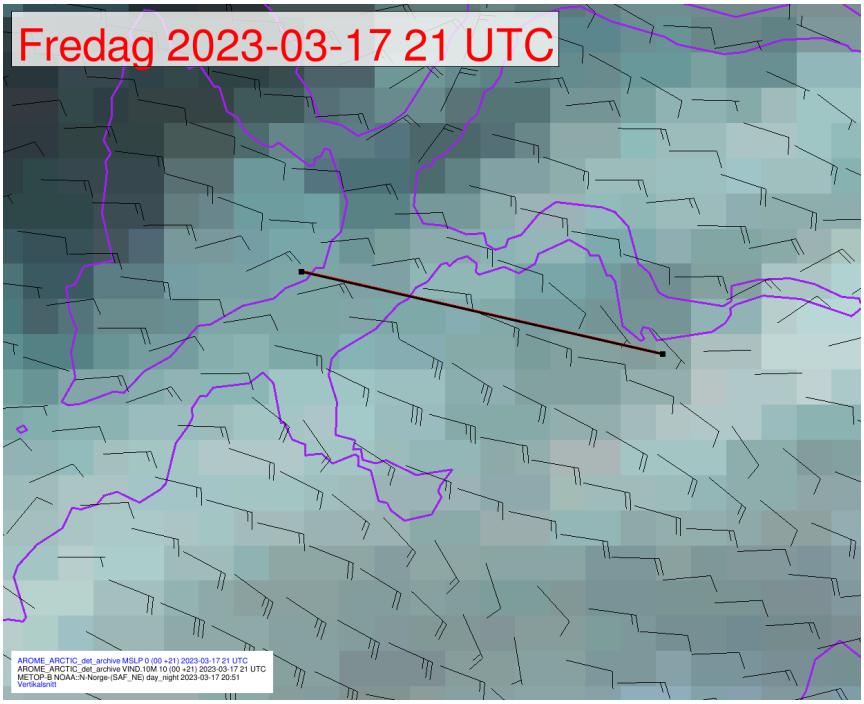

Figure 14: *Polar orbiting visual satellite image (source: Norwegian Meteorological Institute/National Oceanic and Atmospheric Administration (NOAA)) and modelled 10 m wind barbs from Arome Arctic at 17 March 2023 21:00 UTC (21 hour lead time). The black line shows an overview of the location of the vertical cross section in the next figure.*

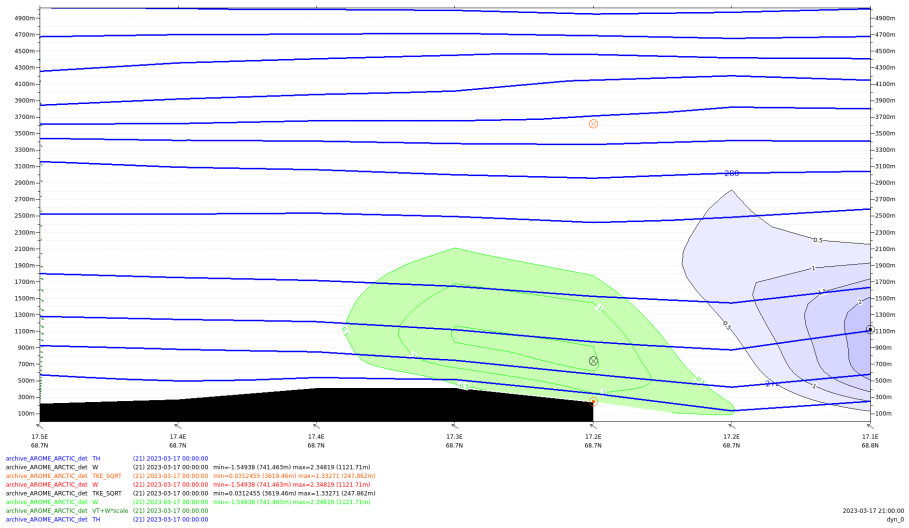

Figure 15: *Vertical cross section from Arome Arctic at 17 March 2023 21:00 UTC (21 hour lead time). Blue lines show the potential temperature with 2K line spacing, green filled contour lines show the negative vertical wind component below* -0.5 *m/s, and blue filled contour lines show the positive vertical wind component above* 0.5 *m/s.*

lines that there were downslope winds in the area resulting from mountain-wave activity (Figures 14 and 15). The modelled vertical wind speeds are however much smaller than the observed ones.

Furthermore, it is discernible that there are also positive vertical velocities in combination with the easterly wind direction in Figure 13. This might be related to variations in vertical velocity in combination with the mountain-wave activity, and it is also apparent that the variations in the positive and negative directions are of a similar magnitude ($\pm$4 m/s). Thus, this case highlights that the positive vertical velocity observed on the feeding barge is not only related to the effect of strong horizontal winds from southwest being lifted when meeting the feeding barge. Hence, the measurement might represent the feeding-barge-undisturbed vertical winds occurring in the atmosphere in such offshore-flow-mountain-wave conditions. It should also be mentioned that the feeding barge is anchored to the sea floor and not rotated or moved by the wind or waves at its location.

4.3.2 Offshore flow case: 27 and 28 May 2023

Another case, with a period of offshore flow, is shown in Figure 16 from mid of 27 May 2023 to beginning of 28 May 2023. Here it is also apparent that the strongest negative velocities are during easterly and northeasterly winds and similar to Figure 13, the variations in Figure 16 in the positive and negative velocities are of similar magnitude which might also be related to mountain-wave activity. These cases are further supported by the data presented in Figures 24 and 25 in Section 4.5, which illustrates stronger TKE during offshore wind conditions.

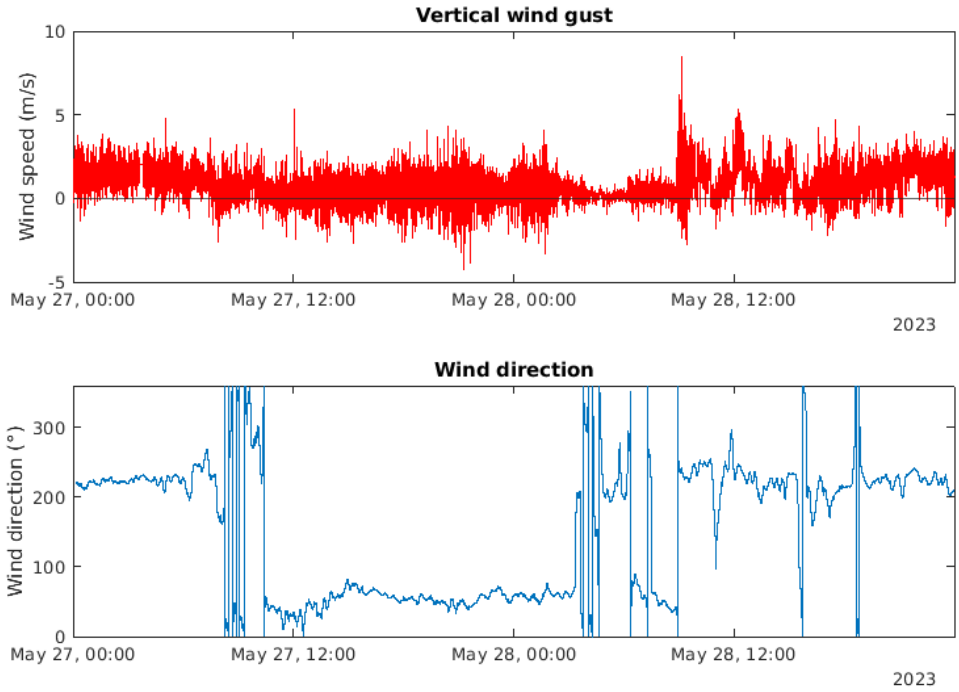

Figure 16: *A case comparison of vertical wind gust (in red, upper panel) and wind direction (in blue, lower panel), 27 to 28 May 2023*

4.3.3 Southwesterly wind case: 3 and 4 April 2023

In Figure 17 a distinct southwesterly flow is apparent from the end of 3 April 2023 until the beginning of 4 April 2023. In conjunction with this southwesterly flow mostly positive vertical velocities are apparent which is quite different from the situations when the winds are coming from the opposite direction. In this case the observed positive vertical velocity may stem from the disturbance induced by the feed barge apparent in Figure 18.

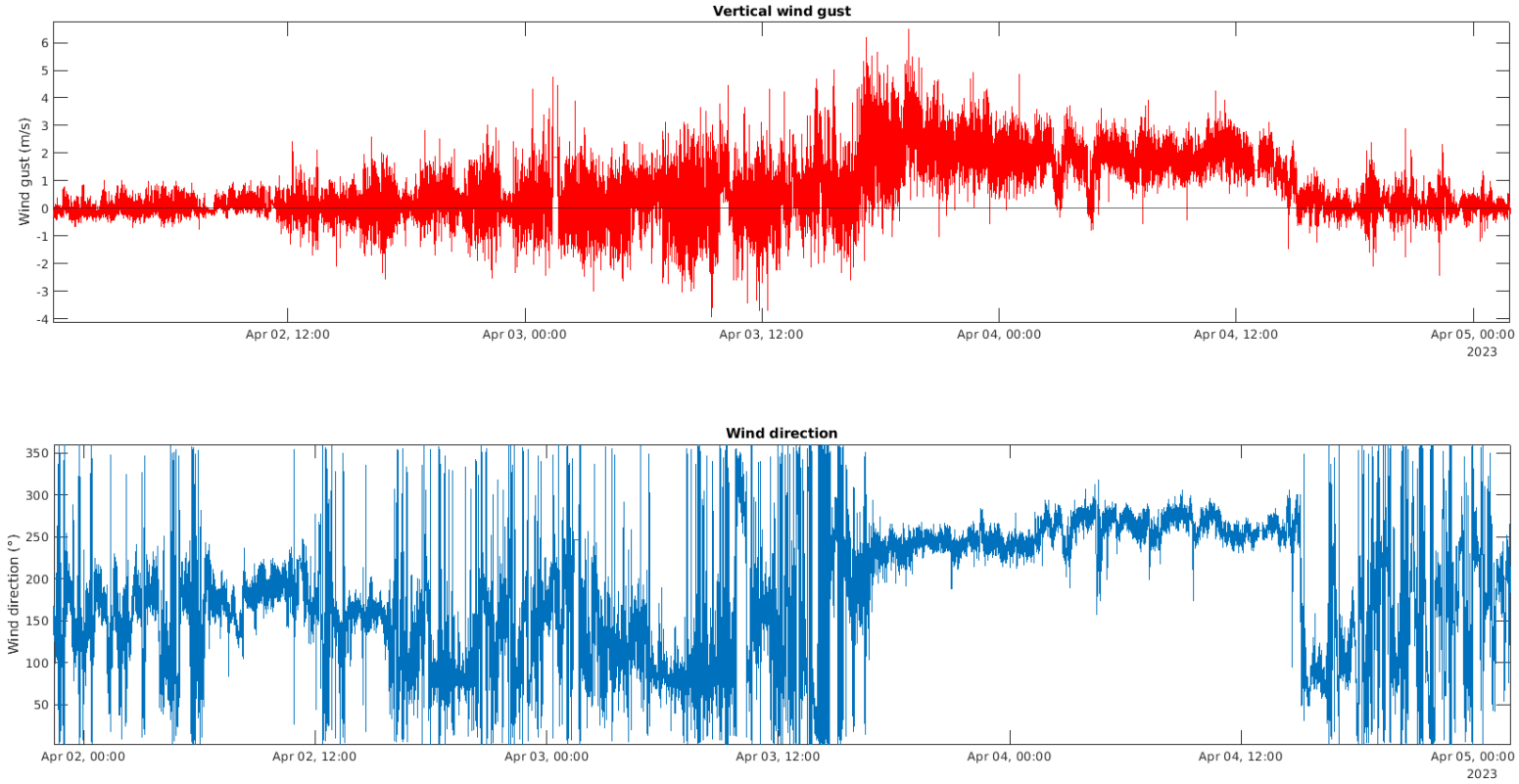

Figure 17: *A case comparison of vertical wind gust (in red, upper panel) and wind direction (in blue, lower panel) during 2 to 4 April 2023*

Figure 18: *Feeding barge affecting the vertical wind velocities during soutwesterly flow. Photo: Eirik Mikal Samuelsen.*

4.3.4 Southwesterly wind case: 24 and 25 May 2023

Finally, Figure 19 also depicts a case with southwesterly winds. In contrast to the case in Figure 17, there are clearly both positive and negative vertical velocities in conjunction with the southwesterly flow at the end of 24 May 2023 and at the beginning of 25 May 2023. However, in contrast to the offshore flow cases (Figures 13 and 16), the positive vertical velocities have higher values up to approximately 6-8 m/s. A satellite image from 25 May at 06 UTC illustrate that there were mountain waves involved also in this southwesterly case (Figure 20). This indicates that part of the positive vertical velocity in this case may stem from mountain waves, and part of it from the feeding-barge disturbance. For this reason one needs to use the vertical velocity data from the 3D sonic anemometer with care when the flow is from the southwest. In future studies, alternative placements of the 3D sonic anemometer should be considered in order to avoid this type of flow disturbance from the feeding barge.

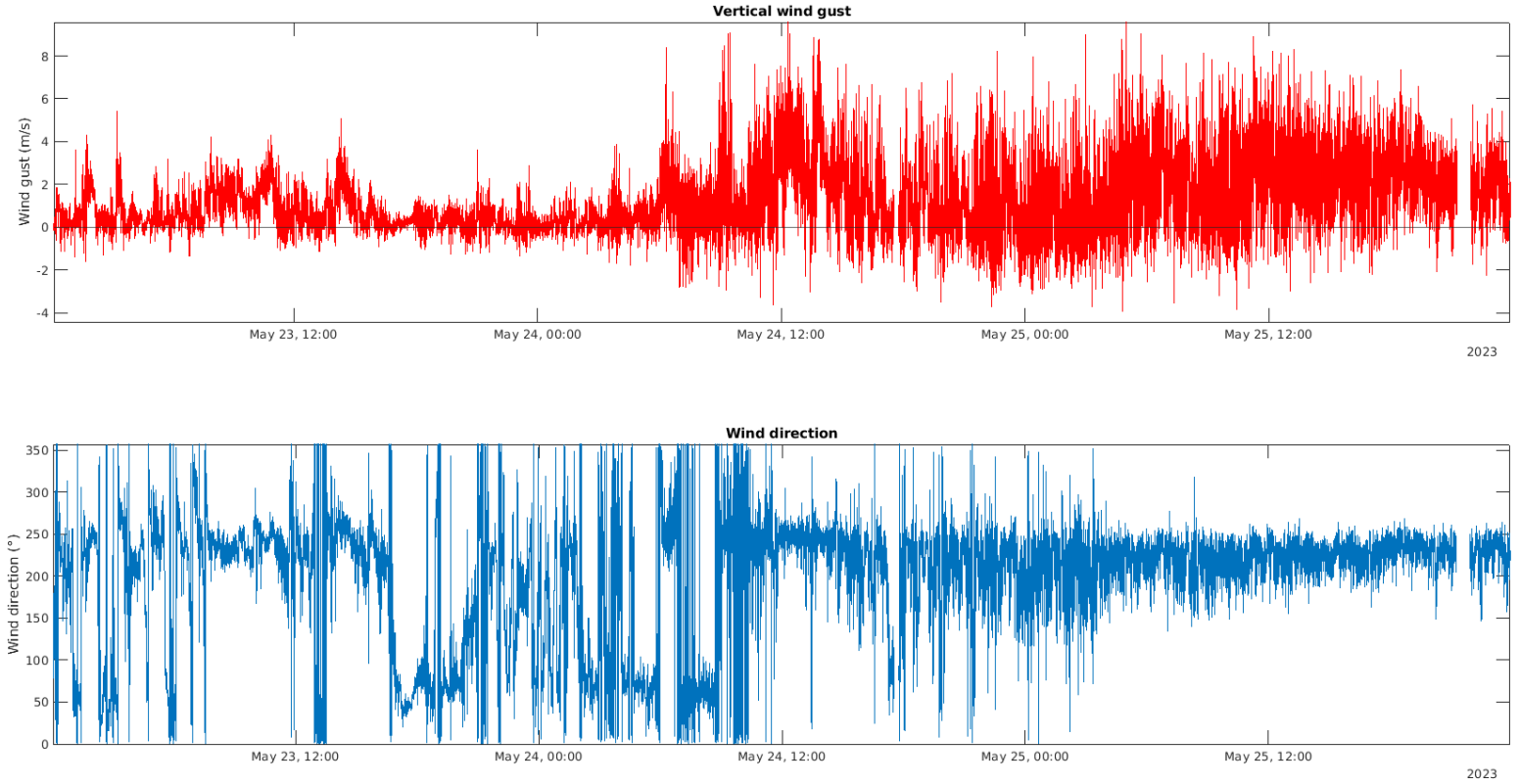

Figure 19: *A case comparison of vertical wind gust (in red, upper panel) and wind direction (in blue, lower panel) from 23 May to 25 May 2023.*

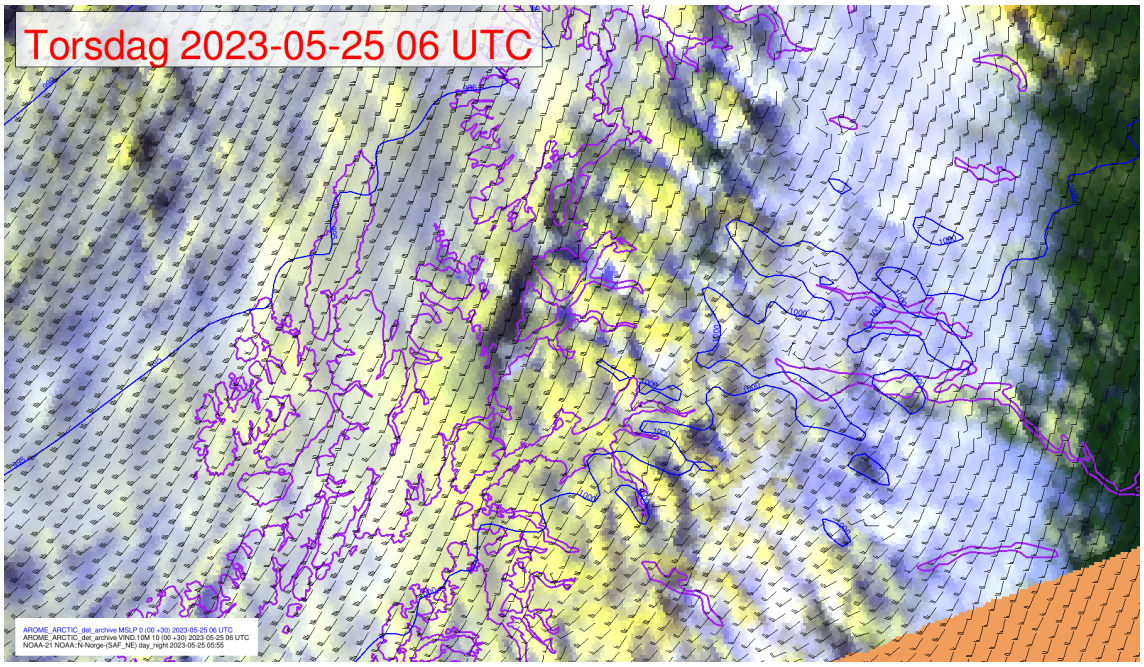

Figure 20: *Satellite image and modelled 10 m wind barbs from Arome Arctic at 25 May 2023 0600 UTC (6 hour lead time).*

4.4 Horizontal wind comparison

Figure 21 shows comparisons of the wind speed and wind direction between the 3D sonic anemometer (Figure 3) and the 2D sonic anemometer of the AWS (Figure 2). For 10 minute average wind-speed comparisons it is perceptible that there are small differences between the wind speed of the AWS compared to that of the 3D sonic anemometer. On average there are 0.4 m/s difference in the comparison period between the two sensors with the AWS having slightly higher values than the 3D sonic anemometer. The correlation between the two instruments are as high as 0.987. For wind-direction comparison the method of Jiménez and Dudhia (2013) is applied in order to assure that the wind direction difference is in the range $[-180°, 180°]$. The BIAS is calculated by taking the direction of the 3D sonic anemometer minus the direction of the AWS. On average the 3D sonic anemometer is veered 23 degrees compared to the wind direction of the AWS. This is further highlighted in Figure 22 where the differences in the direction between the two devices are discernible. The wind roses are retrieved by using the MATLAB (The MathWorks Inc., 2023) function WindRose from Pereira (2023). After inspecting the documentation of the instruments it is perceptible that the 3D sonic anemometer is adjusted towards geographical north, while the AWS has a built-in compass which automatically

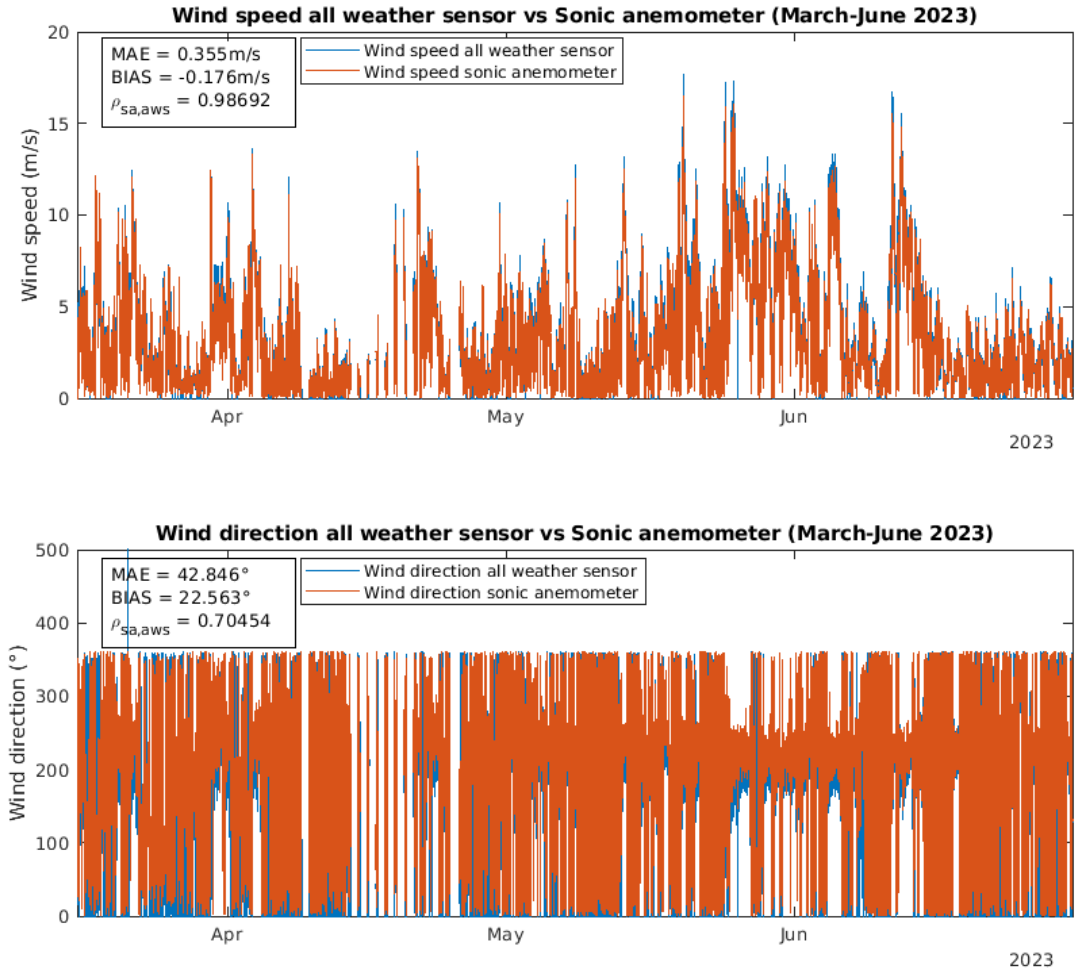

Figure 21: *Wind speed (upper panel) and wind direction (lower panel) comparison between the AWS (in blue) and the 3D sonic anemometer (in red) from 15 March to 30 June 2023.*

shows the direction compared to magnetic north. At this high north the magnetic declination is around 9 degrees, so the magnetic declination is not the sole explanation for the differences between the two sensors with a mean difference of up to 22.6 degrees (Figure 21). Probably the metal of the feed barge is also affecting the compass of the AWS. This underlines that one should be careful of using anemometers with built-in compass when doing measurements on a site like this.

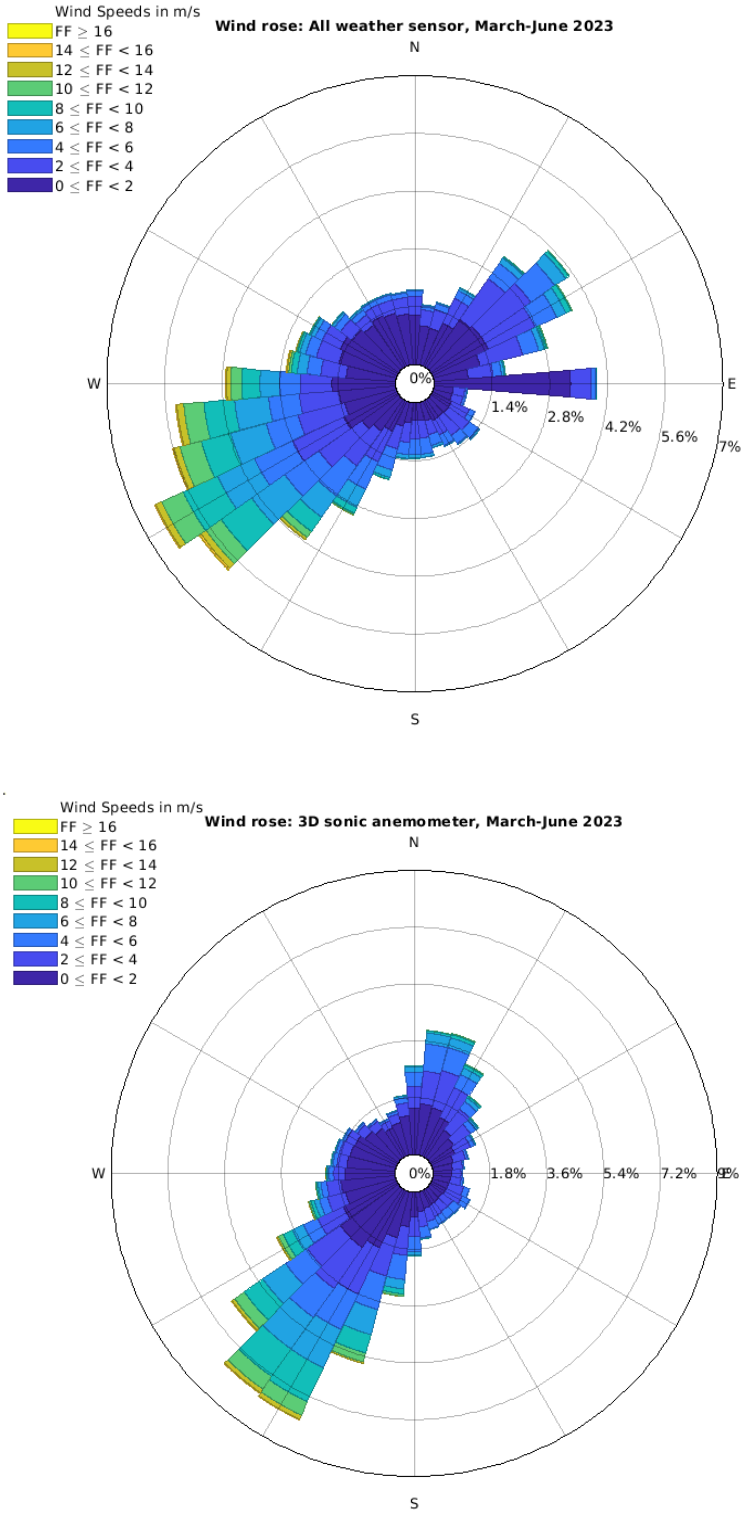

Figure 22: *Wind rose based on wind direction and wind speed from the AWS (upper panel) and the 3D sonic anemometer (lower panel) in the period 15 March to 30 June.*

4.5 TKE

Figure 23 shows the wind direction and wind speed plotted together with TKE. In general, the TKE values presented in the plots are difficult to rely on due to unrealistically high vertical velocities, likely caused by disturbances from the feeding barge. However, the TKE is also investigated during periods of offshore winds as the vertical winds measured by the 3D sonic anemometer might be undisturbed from the feeding barge during such conditions. Figure 24 shows the wind direction and wind speed together with the $\sqrt{\text{TKE}}$ measured during the offshore-flow-mountain-wave conditions during 17 and 18 March 2023 (see Figure 13). It is evident that during this period, both the horizontal wind speed and the turbulence are stronger from the afternoon the 17th until noon the 18th in the period of offshore flow, compared to the period with winds from other directions.

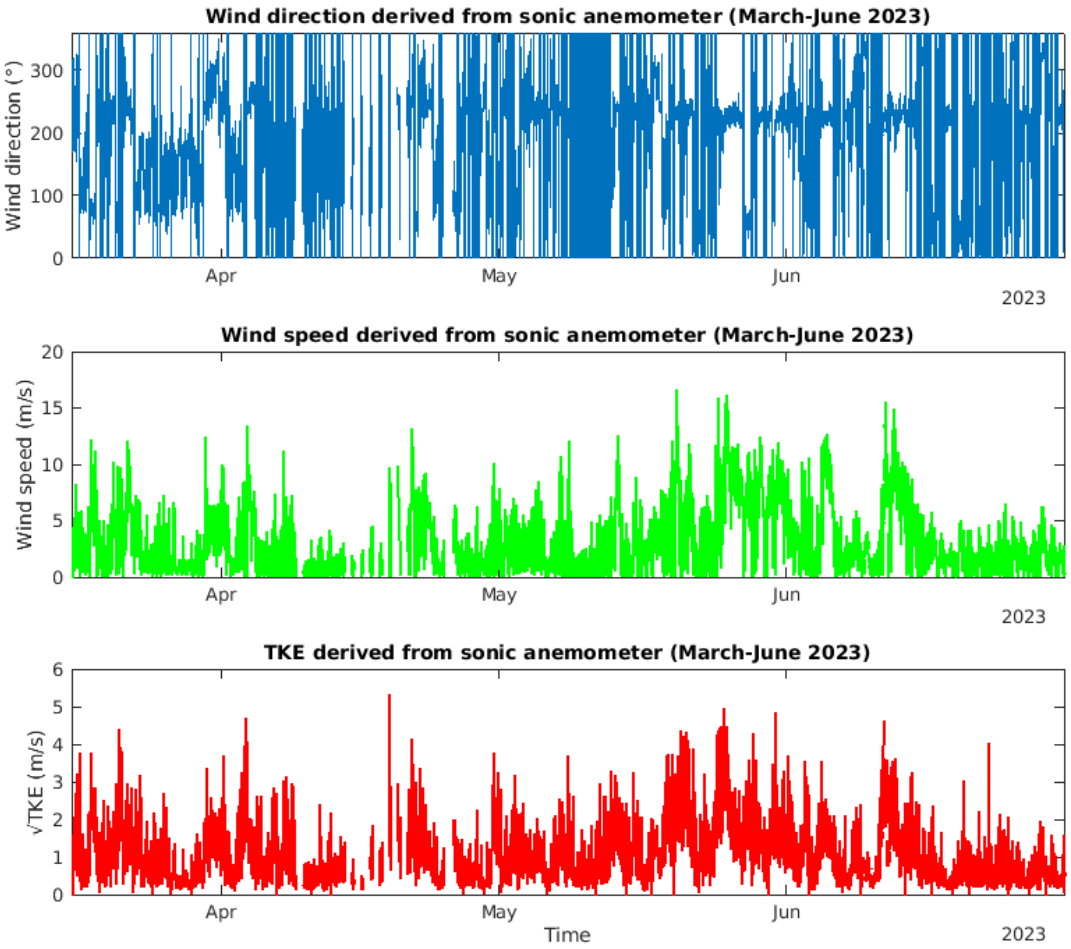

Figure 23: *Wind direction (in blue), wind speed (in green), and $\sqrt{TKE}$ (in red) in the period 15 March to 30 June 2023 derived from the 3D sonic anemometer.*

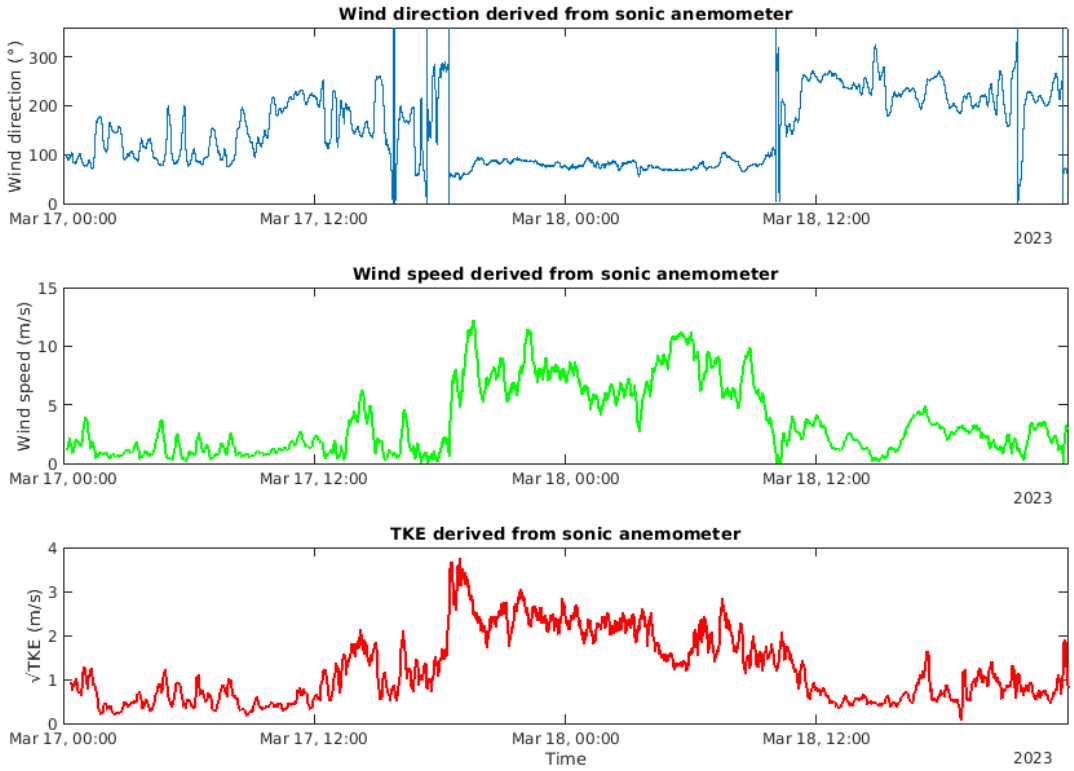

Figure 24: *Wind direction (in blue) and speed (in green) together with* $\sqrt{TKE}$ *(in red) from offshore winds 17 and 18 March 2023.*

Figure 25 shows the wind direction and wind speed together with the $\sqrt{\text{TKE}}$ for the period 27 and 28 May 2023. As already mentioned, this is also a case with offshore flow mountain-wave activity (see Figure 16). Thus, also in this case it appears to be more turbulence and stronger winds during the offshore-wind period compared to the rest of the time series. Thus, feeding barge disturbance is probably not affecting the increased $\sqrt{\text{TKE}}$ apparent from Figure 25. However, there are also some peaks in the winds and $\sqrt{\text{TKE}}$ after this period in the morning of the 28th May, which seems to be connected to southwesterly flow and feeding barge disturbance.

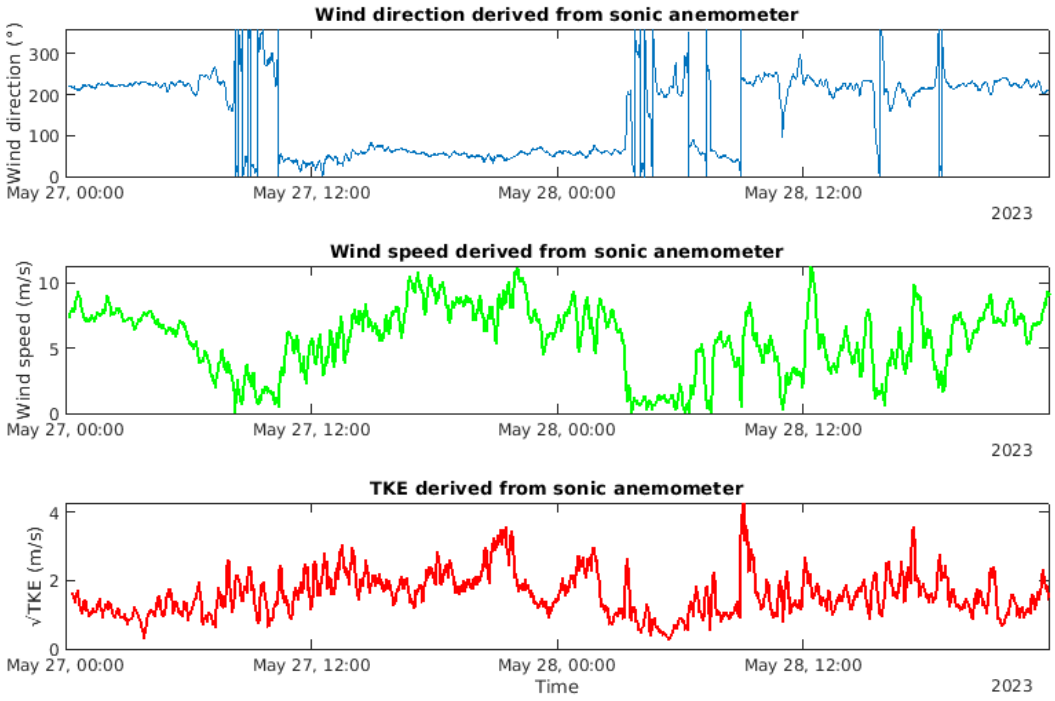

Figure 25: *Wind direction (in blue) and wind speed (in green) together with* $\sqrt{TKE}$ *(in red) from offshore winds 27 and 28 May 2023.*

4.6 Dry temperature comparison

Figure 26 illustrates the calculated dry temperature (T_d) and the temperature measured by the AWS, and the BIAS and the MAE between the calculated and the observed dry temperature (see Section 3.3). The two parameters exhibit a strong correlation, and the mean absolute difference is only 0.34 °C, indicating that the dry temperature derived from sonic temperature measurements by the 3D sonic anemometer, in combination with relative humidity data from the AWS, is accurate.

4.7 Sensible heat flux

Figure 27 shows the sensible heat flux derived from the 3D sonic anemometer data. Only values between [-500,500] W m^{-2} are included in this plot. However, due to the aforementioned challenges with the vertical velocities, the sensible heat-flux data from this station are not reliable when considering winds from all directions.

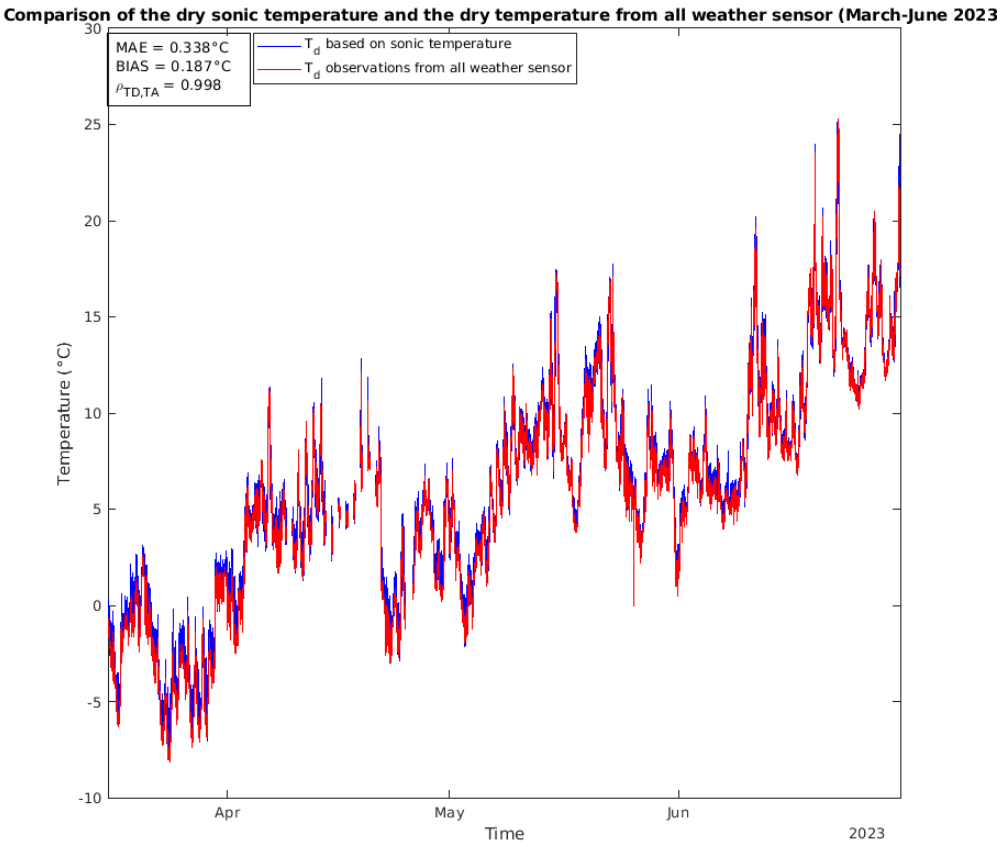

Figure 26: *The dry temperature (T_d) (see Section 3.3) derived from the 3D sonic anemometer and the AWS (in blue) and the measured T from the AWS (in red) compared for the period 15 March to 30 June 2023.*

4.8 Estimated SST

Figure 28 shows the estimated sea-surface temperature from the outgoing longwave radiation data. When comparing this figure with the observed air temperature in Figures 7 and 8, this estimated SST seems to follow the air temperature too closely, showing that an estimated SST from these outgoing longwave radiation measurements are not reliable. The reason for this discrepancy could be that the outgoing radiation measurements are affected in large parts from the radiation from other instruments and parts of the installation of the barge, instead of measuring the radiation from the ocean. A visual inspection of Figure 29 highlights that this is in fact most probably the case.

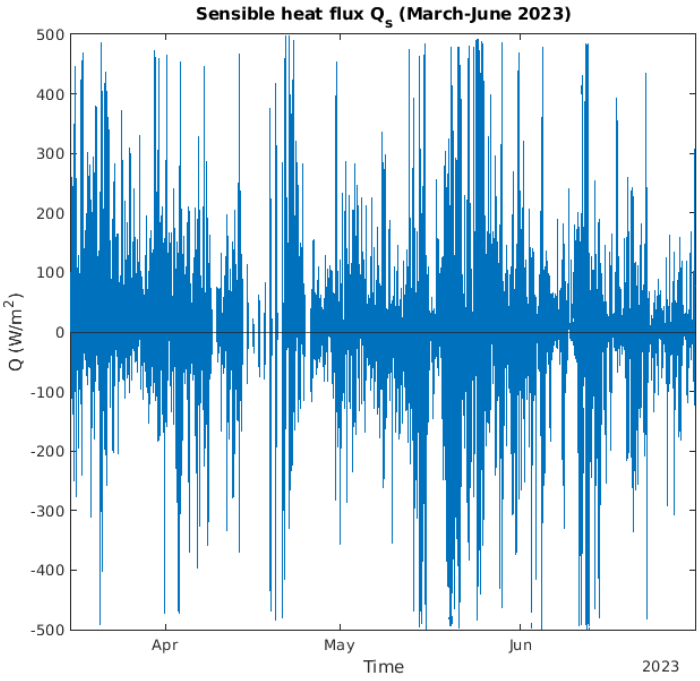

Figure 27: *Sensible heat flux derived from the 3D sonic anemometer data.*

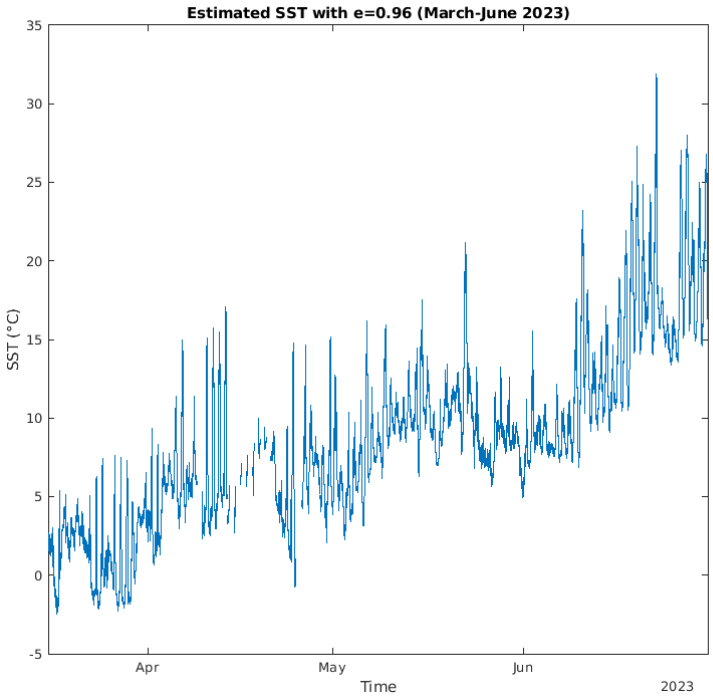

Figure 28: *Estimated SST from outgoing longwave radiation as described in Section 3.7 for the period 15 March to 30 June 2023.*

Figure 29: *Illustration of how the outgoing longwave and shortwave radiation are influenced by the barge. Photo: Eirik Mikal Samuelsen.*

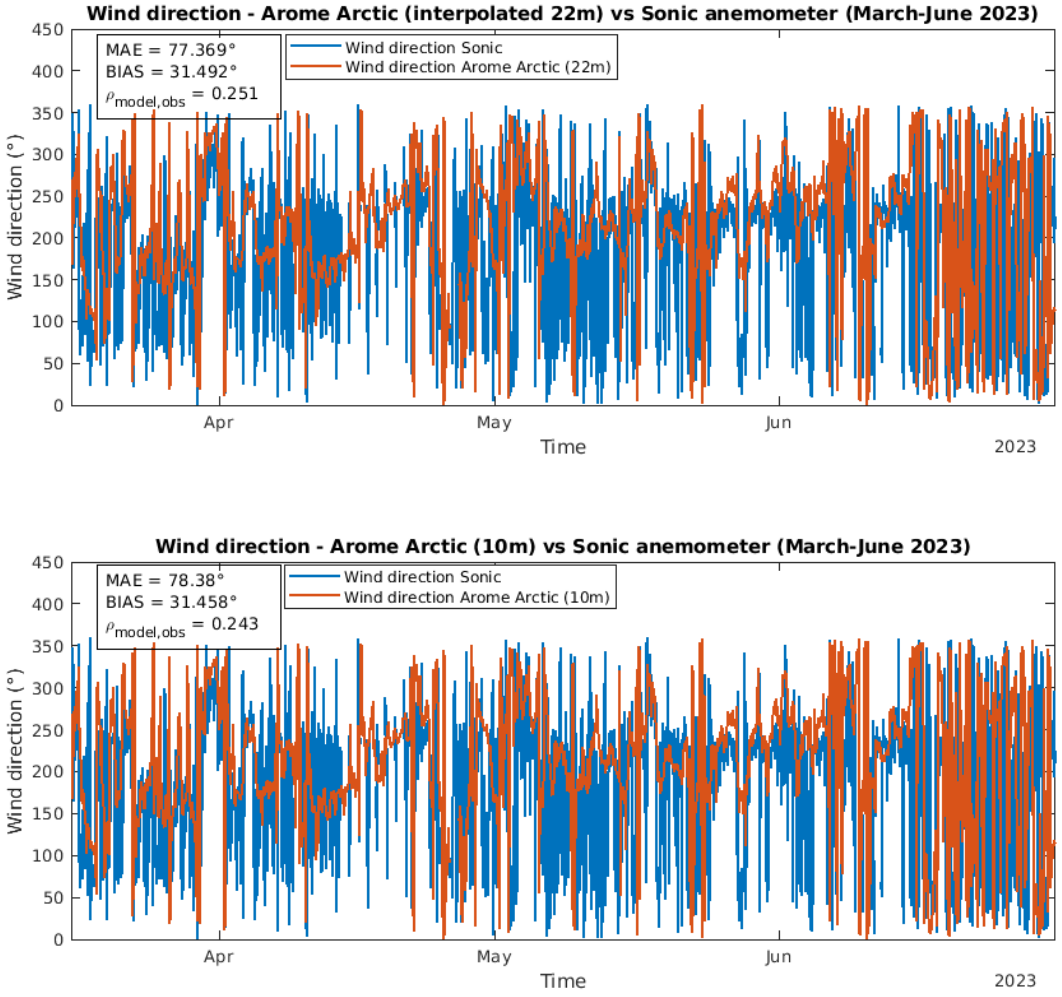

Figure 30: *Wind direction from Arome Arctic (in red) and observations from the 3D sonic anemometer (in blue). Upper panel shows the Arome Arctic wind direction of the vertical interpolated value from the two lowest model levels at 22 m and in the lower panel the wind direction value from the Arome Arctic wind at 10 m is presented.*

4.9 Model verification

4.9.1 Horizontal wind

Figure 30 shows the wind direction from the Arome Arctic model interpolated to 22 m and at 10 m, verified against the wind direction from the 3D sonic anemometer, including MAE, BIAS, and the Pearson correlation coefficient for the period 15 March to 30 June 2023. The 22 m wind direction from Arome Arctic has slightly lower MAE compared to the MAE of the wind direction from the 10 m wind, but in general the differences

between the two wind direction parameters are very small. However, the correlation coefficient shows a very weak linear relationship between the observed and modelled wind directions, as well as a relatively high MAE, for both the 22 m and 10 m Arome Arctic winds. This may be attributed to the horizontal resolution of Arome Arctic being insufficient to resolve topographical effects that induce local variations in wind direction. Likewise, Figure 31 depicts the wind speed from Arome Arctic at 22 m and at 10 m, alongside the observed wind speed. The 22 m wind speed from Arome Arctic exhibits a larger positive BIAS and a higher MAE compared to the 10 m wind speed. However, during certain periods in May and June, the 3D sonic anemometer records higher horizontal wind speeds than those predicted by the model. The locally negative BIAS may result from an underestimation of strong winds by Arome Arctic in topographically influenced flow conditions – such as mountain waves and downslope windstorms – that are likely not sufficiently resolved by the model. In order to examine this in greater detail, the evaluation is limited to cases with observed wind speeds above 8 m/s. Under these conditions,

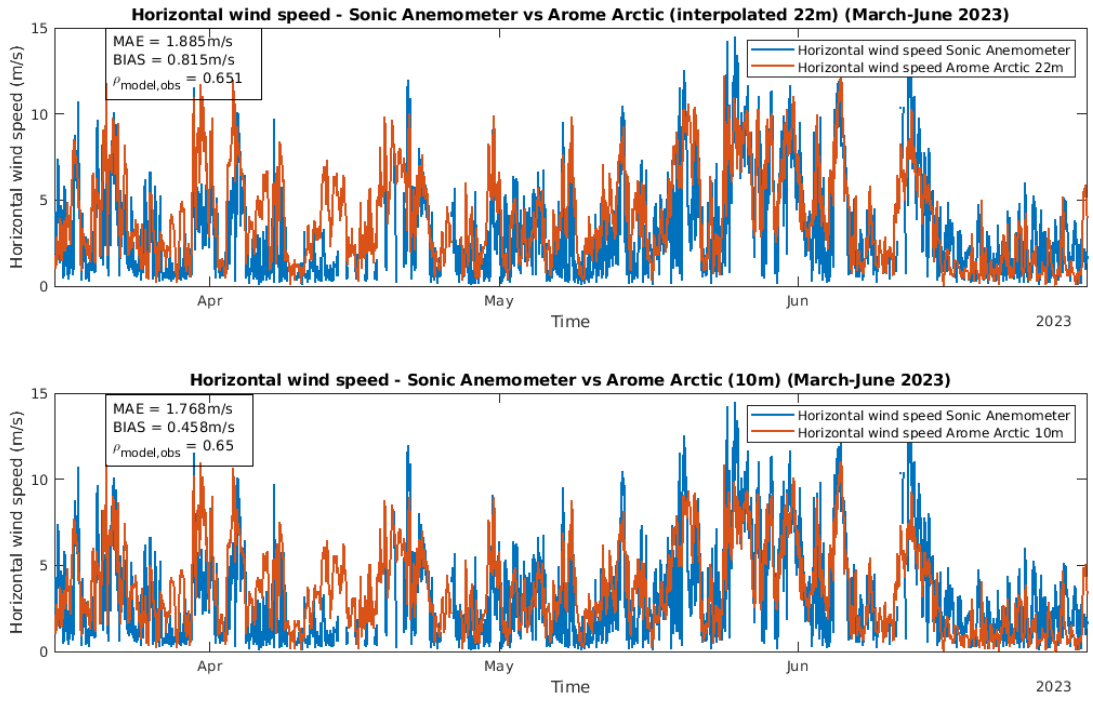

Figure 31: *Wind speed from Arome Arctic (in red) and observations from the 3D sonic anemometer (in blue). Upper panel shows the 22 m interpolated model wind speed together with the observed wind speed, and the lower panel presents 10 m model wind speed as well as the observed wind speed.*

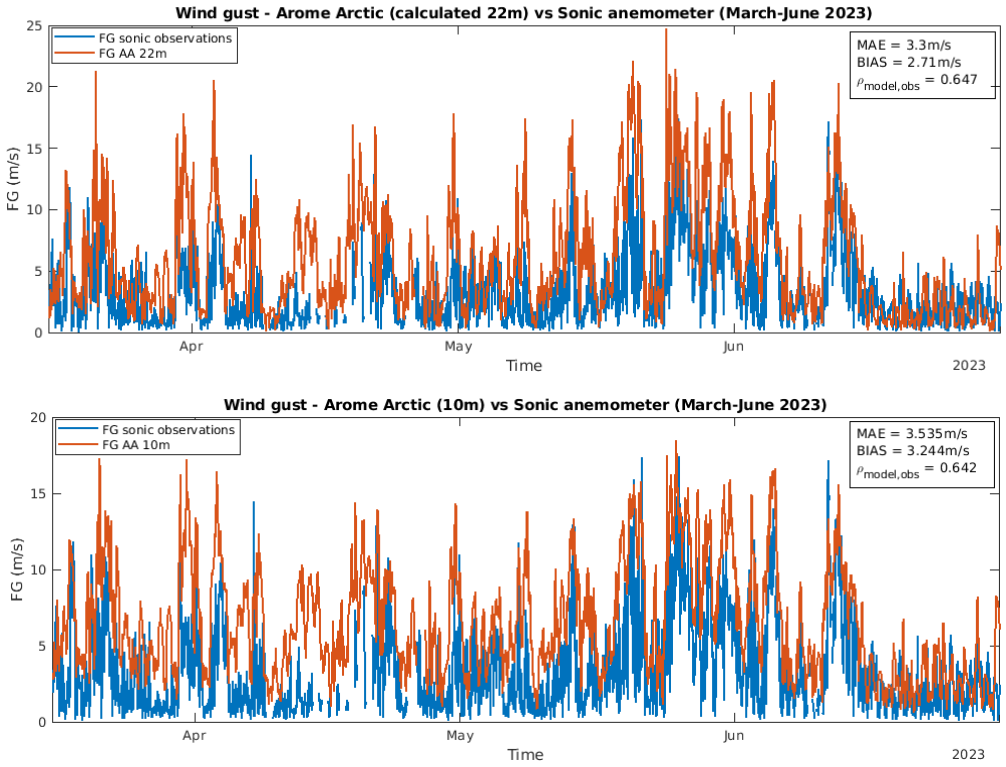

Figure 32: *Wind gust from Arome Arctic (AA, in red) and observations from the 3D sonic anemometer (in blue). Upper panel shows the 22 m AA value and the lower panel shows the 10 m wind gust of AA.*

interpolated model winds at 22 m produce a BIAS of -0.47 m/s and an MAE of 1.27 m/s, while model winds at 10 m yield a BIAS of -0.99 m/s and an MAE of 1.39 m/s.

Figure 32 shows the wind gust from Arome Arctic at 22 m and 10 m, verified against the wind gust from the 3D sonic anemometer, including MAE, BIAS, and r. The results indicate that the model tends to overestimate wind gusts relative to observations. This overestimation may be attributed to the same limitations affecting the mean wind speed, namely the difficulty of the 2.5 km model in resolving topographically induced features due to its limited spatial resolution. However, instead of providing a negative BIAS when the winds are strong, as is the case for the mean winds (Figure 31), the modelled wind gust values appear to be too high for almost all of the cases. Furthermore, a more detailed inspection of individual cases illustrate that particularly the gusts in the model is too high when the wind is coming from the southeast, when the wind in the reality is coming from the east. This is further explained in section 5.8 by inspecting the Figures 85 and 88.

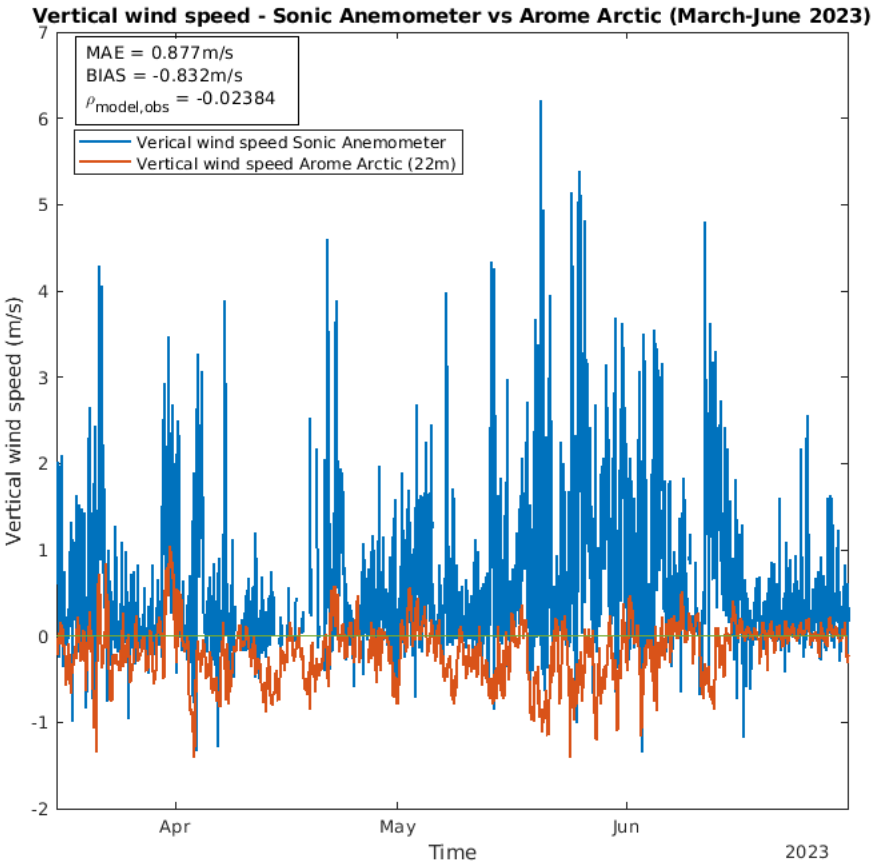

Figure 33: *Vertical wind from Arome Arctic (in red) and observations from the sonic anemometer (in blue).*

4.9.2 Vertical wind

Figure 33 shows the vertical wind component from Arome Arctic interpolated to 22 m verified against the vertical wind component from the 3D sonic anemometer, including the verification scores. Here it is apparent that the 3D sonic anemometer has unrealistic high vertical velocities, most likely due to the feeding barge disturbance during southwesterly winds as earlier mentioned.

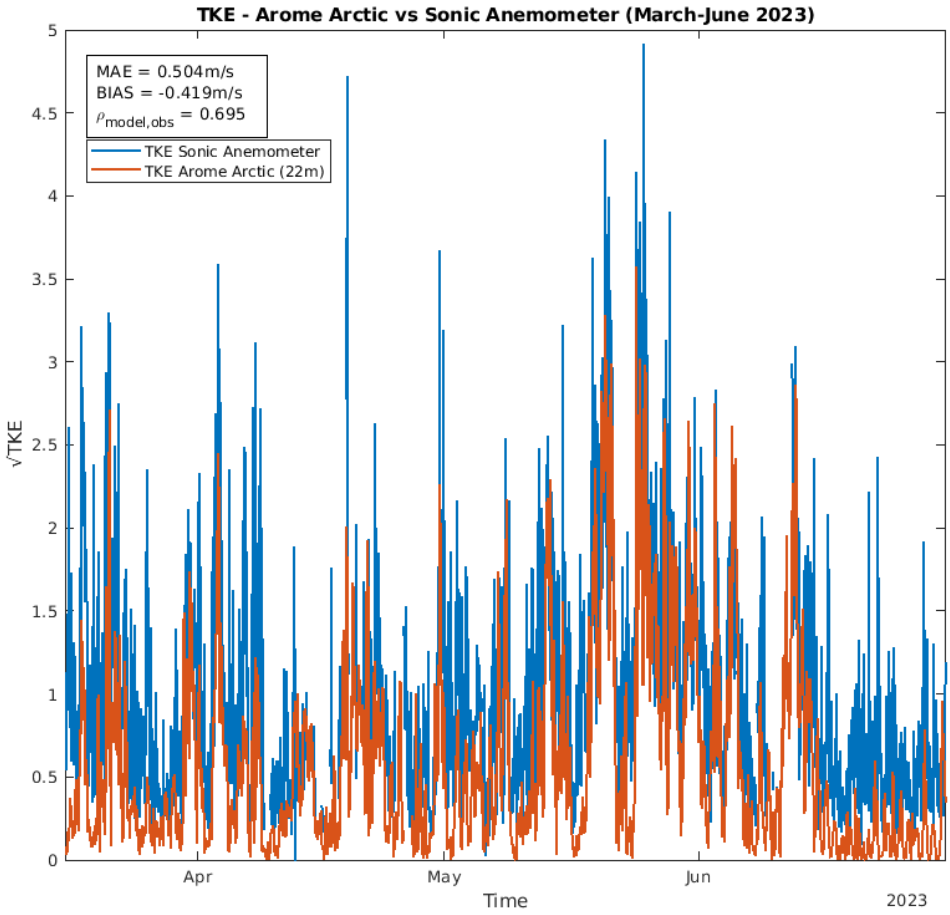

Figure 34: *$\sqrt{TKE}$ from Arome Arctic (in red) and observations from the sonic anemometer (in blue).*

4.9.3 Turbulent kinetic energy

Figure 34 presents the $\sqrt{\text{TKE}}$ from Arome Arctic, interpolated to 22 m height, alongside $\sqrt{\text{TKE}}$ values derived from the 3D sonic anemometer, including corresponding verification statistics. Overall, the 3D sonic anemometer records higher turbulence levels than those predicted by Arome Arctic. However, part of this discrepancy may be attributed to flow disturbances caused by the feeding barge, particularly under southwesterly wind conditions. Consequently, it is challenging to draw definitive conclusions from this comparison alone. A more detailed, case-based analysis of $\sqrt{\text{TKE}}$ under offshore flow conditions is required to provide an adequate assessment of model performance for this parameter (see Section 4.10).

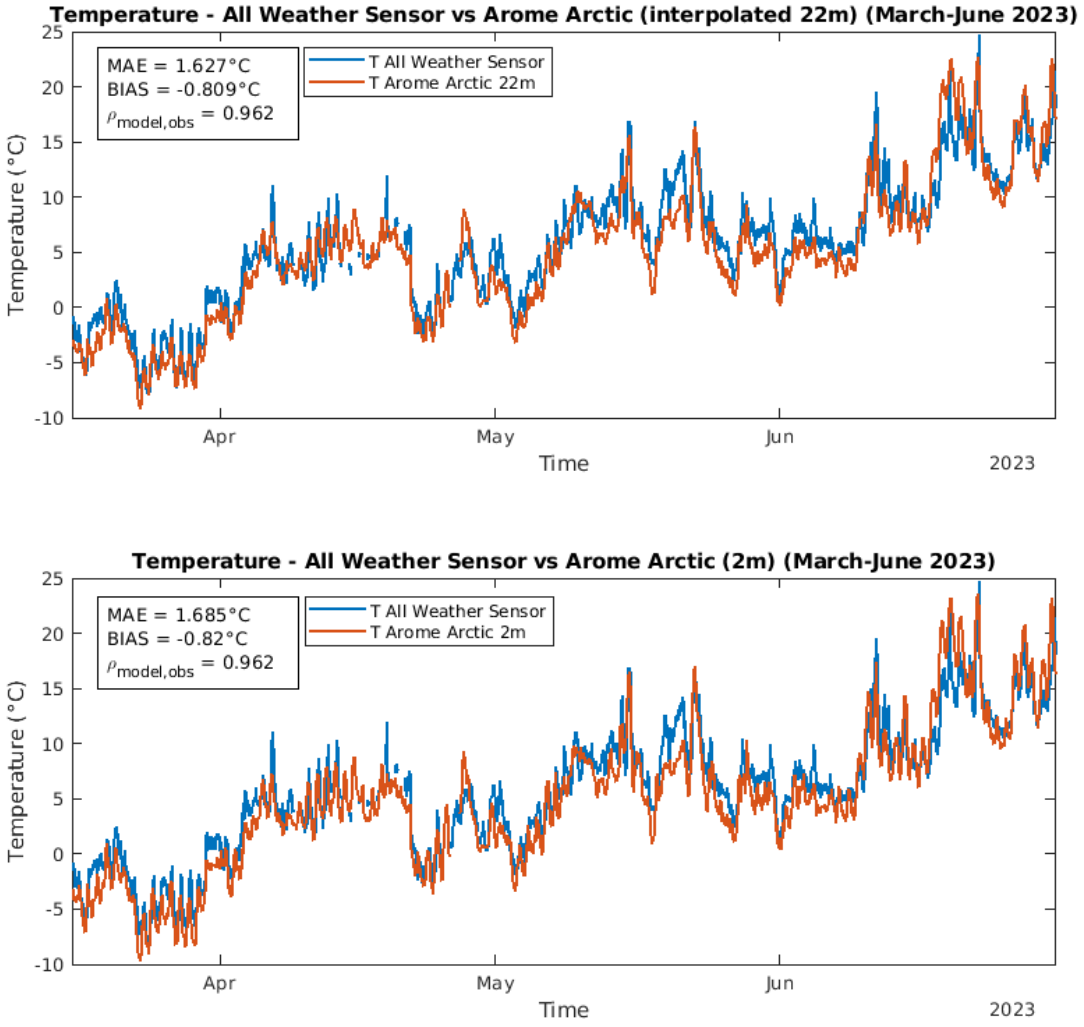

Figure 35: *Temperature from Arome Arctic (in red) and observations from the AWS (in blue) with the upper panel showing the 22 m model temperature, and the lower panel depicting the 2 m model temperature.*

4.9.4 Temperature

Figure 35 shows the temperature from Arome Arctic at 2 m and interpolated to 22 m, verified against the temperature measured from the AWS. The Arome Arctic temperature at 22 m yielded a slightly lower MAE than the 2 m temperature. Moreover, the results show that the AWS measured on average 0.81°C higher temperatures compared to the Arome Arctic temperature at 22 m, leading to a negative temperature BIAS in the model. The MAE of T_{M22} is 1.63°C. On the other hand, the r between the modelled and the measured temperature is as high as 0.96 meaning that the observed temperature fluctuations

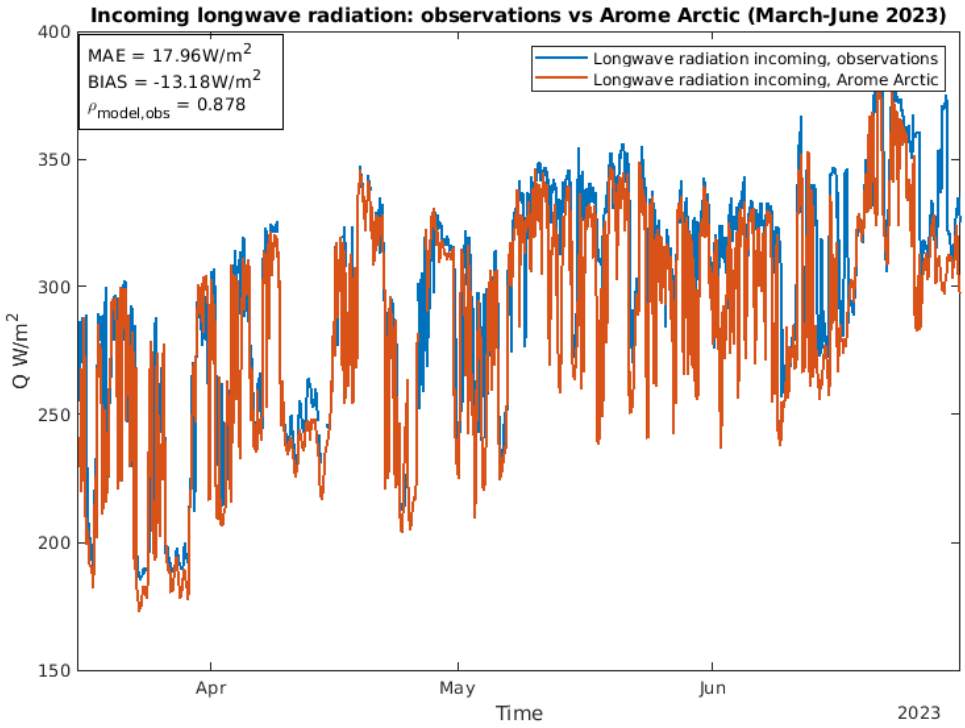

Figure 36: *Incoming longwave radiation from Arome Arctic (in red) and observations from the net radiometer (in blue).*

are accurately captured by the model. This is also apparent from visual inspection of Figure 35.

4.9.5 Incoming longwave radiation

A comparison between incoming longwave radiation from Arome Arctic and corresponding measurements from the net radiometer is presented in Figure 36. The negative BIAS indicates that the model underestimates incoming longwave radiation relative to the observations. This discrepancy may be attributed to an underestimation of atmospheric temperatures in the model (see Figure 35), or to a possible underrepresentation of cloud cover. Figure 37 shows the observed, calculated, and the Arome Arctic output of the incoming longwave radiation, and the MAE between these parameters, respectively. One of the goals is to see if the current parameterization method for incoming longwave radiation used in the spray-icing model MINCOG at MET Norway is working well or could be further optimized as described in Section 3.6. The optimal emissivity ($\varepsilon_{\text{optimal}}$), which provides the smallest MAE between the calculations and the observations, is found to be

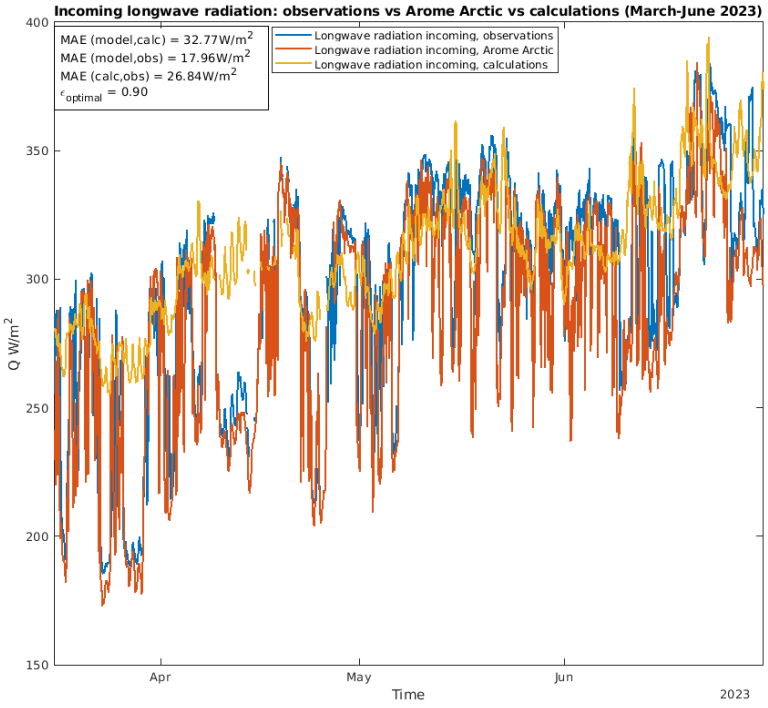

Figure 37: *Incoming longwave radiation; observed (in blue), calculated (in yellow) and from Arome Arctic (in red). MAE and BIAS between these are included, as well as the optimal epsilon used for the calculations.*

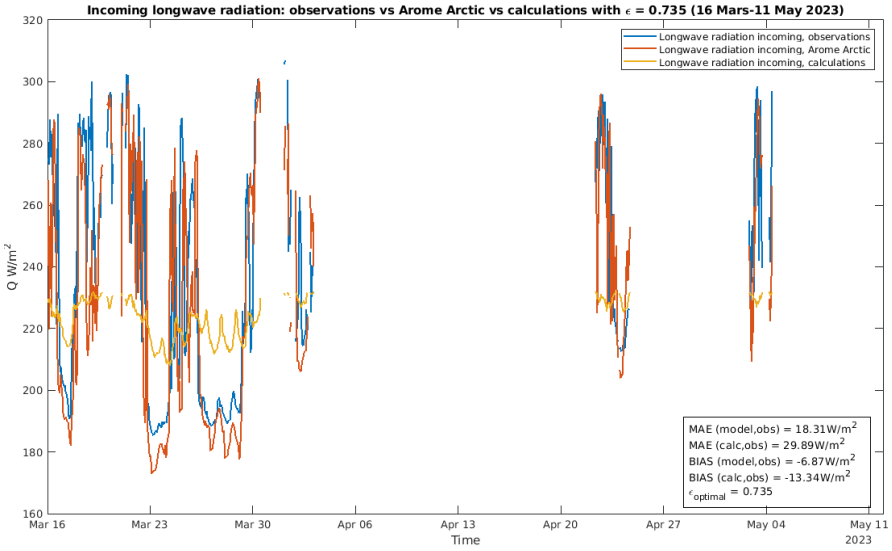

Figure 38: *Optimal emissivity ($\varepsilon_{optimal}$) derived using data with temperatures below 0°C in the period 15 March to 30 June 2023, as well as the corresponding calculated incoming longwave radiation (in yellow), observed LW_{in} (in blue), and LW_{in} Arome Arctic model data (in red).*

$\varepsilon_{\text{optimal}} = 0.90$ for this time period in consideration, according to Eq.(7). A key advantage of using a longwave radiation formulation with a prescribed atmospheric emissivity is that it reduces large variations in the applied longwave radiation flux, thereby minimizing the sensitivity of the icing model to errors in the representation of cloud cover in the atmospheric model. On the other hand, more realistic net radiative cooling (or warming) effect from the atmosphere is expected to be found if using the direct model output of LW from the Arome Arctic model in the spray-icing model MINCOG.

In order to further investigate the optimal emissivity for the MINCOG model, only periods with sub-feezing temperatures are considered. Figure 38 presents the observed and modelled incoming longwave radiation, along with the calculated longwave radiation using an optimal emissivity ($\varepsilon_{\text{optimal}}$) derived by considering only temperatures below 0°C. The resulting optimal emissivity for these cold periods is $\varepsilon_{\text{optimal}} = 0.735$. The MAE of the calculated LW_{in} is higher than the MAE from Arome Arctic. A BIAS of -6.87 W m^{-2} is found between the modelled and observed incoming longwave radiation, confirming that the model underestimates the observed fluxes. When using the calculated longwave radiation, the BIAS becomes more negative, reaching $-13.34\ W\ m^{-2}$.

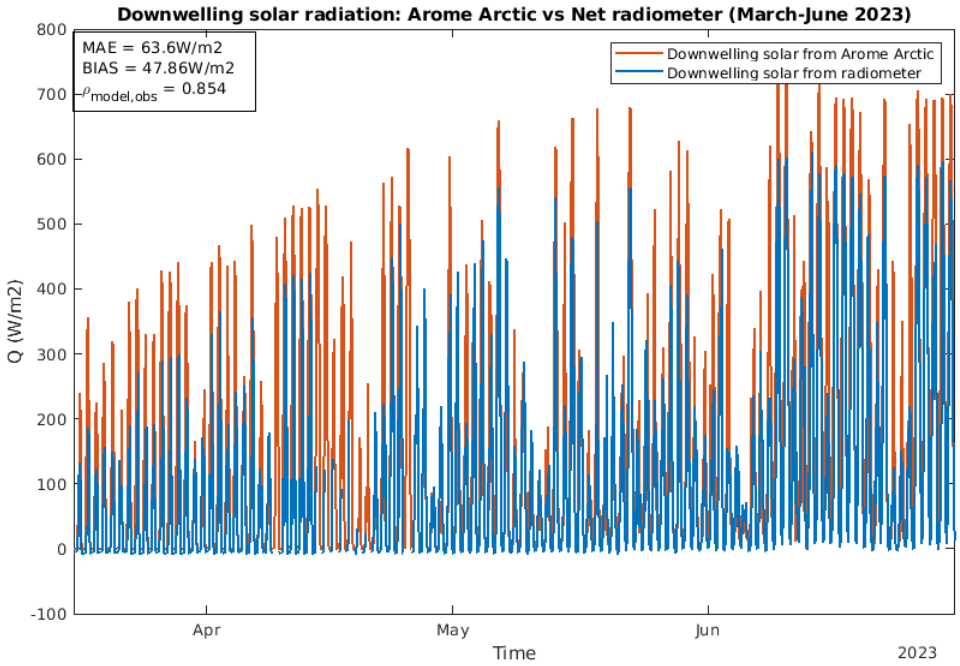

Figure 39: *Incoming shortwave radiation from Arome Arctic (in red) and observations from the net radiometer (in blue) for the period 15 March to 30 June 2023.*

4.9.6 Incoming shortwave radiation

Figure 39 shows the incoming shortwave radiation from Arome Arctic verified against the incoming shortwave radiation from the net radiometer. The positive BIAS reflects an overestimation of shortwave radiation by the model. This may be attributed to an underrepresentation of cloud cover in the model. It may also be related to the fact that the model is not considering the shadow effects from the mountains in the radiation scheme.

4.9.7 Precipitation

Figures 40 and 41 show the hourly and 24-hour accumulated precipitation, respectively, from Arome Arctic and the AWS. The results indicate that the modelled 24-hour accumulated precipitation exhibits a stronger correlation with observations than the modelled hourly precipitation. This is likely due to the lower predictability of short-term (hourly) precipitation fluctuations compared to daily totals. Overall, the model tends to overestimate 24-hour accumulated precipitation at this site. However, an exception is observed in mid-April, where a significantly higher 24-hour precipitation value is recorded by the AWS compared to the model. This suggests that in certain high-precipitation events, the model may underestimate 24-hour totals.

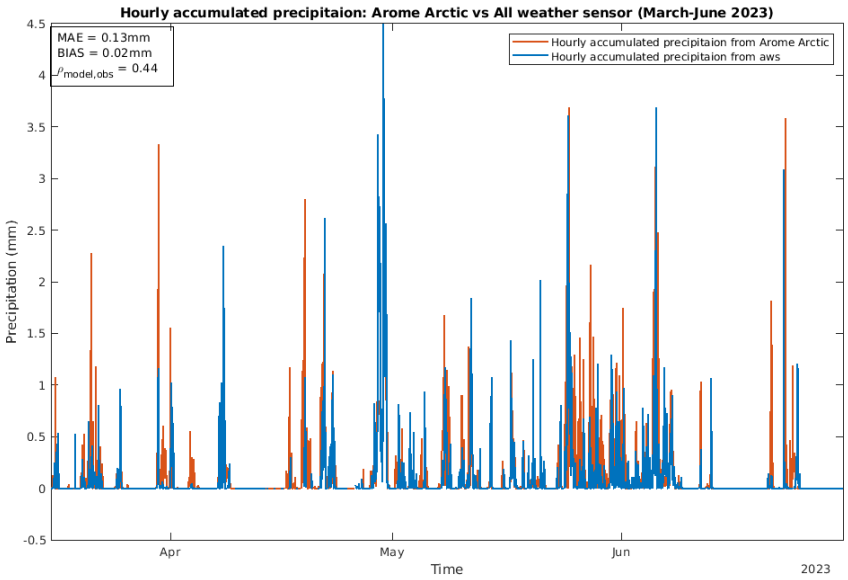

Figure 40: *Precipitation intensity from Arome Arctic (in red) and the AWS (in blue) from 15 March to 30 June 2023.*

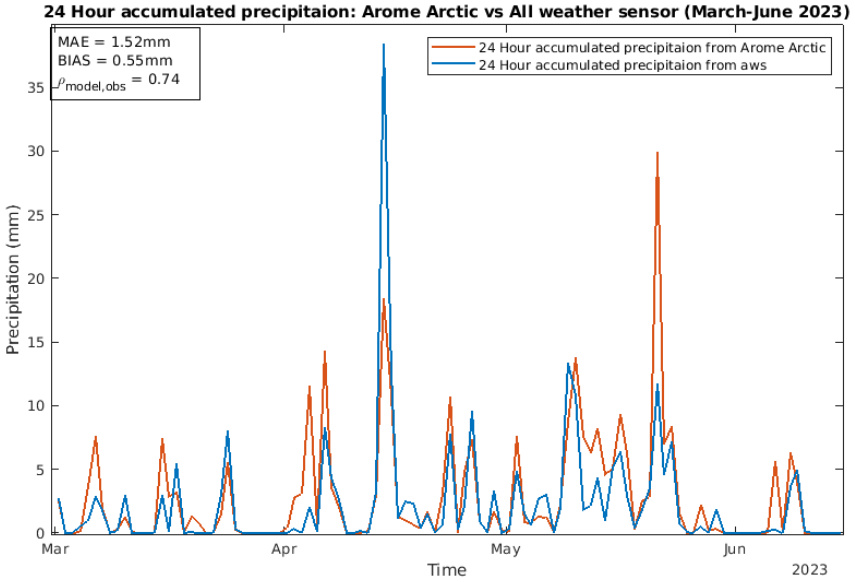

Figure 41: *24-hour accumulated precipitation from Arome Arctic (in red) and the AWS (in blue) from 15 March to 30 June 2023.*

4.9.8 Atmospheric pressure

Figure 42 presents armospheric pressure from Arome Arctic, both at mean sea level and interpolated to 22 m height, compared against observations from the AWS. The relatively low BIAS and MAE, along with a high correlation coefficient of 0.998, indicate that the modelled pressure agrees well with the observed values. However, the pressure interpolated to 22 m is less accurate than the mean sea level pressure (MSLP) when compared with the observed pressure at 22 m. Specifically, the MSLP exhibits a positive bias relative to the observations, while the interpolated 22 m pressure shows a negative bias. One possible explanation for this discrepancy is a higher frequency of downslope wind events in the model than in the observations, as previously discussed in relation to Figure 32.

4.9.9 Relative humidity

Figure 43 presents relative humidity from Arome Arctic at 2 m and 22 m, compared with observations from the AWS. The relatively high MAE of approximately 11% indicates a moderate deviation between the modelled and observed values. At 22 m, the BIAS indicates a 3% overestimation when comparing the modelled relative humidity from Arome Arctic to the observations at the same height. This discrepancy may be related to an un-

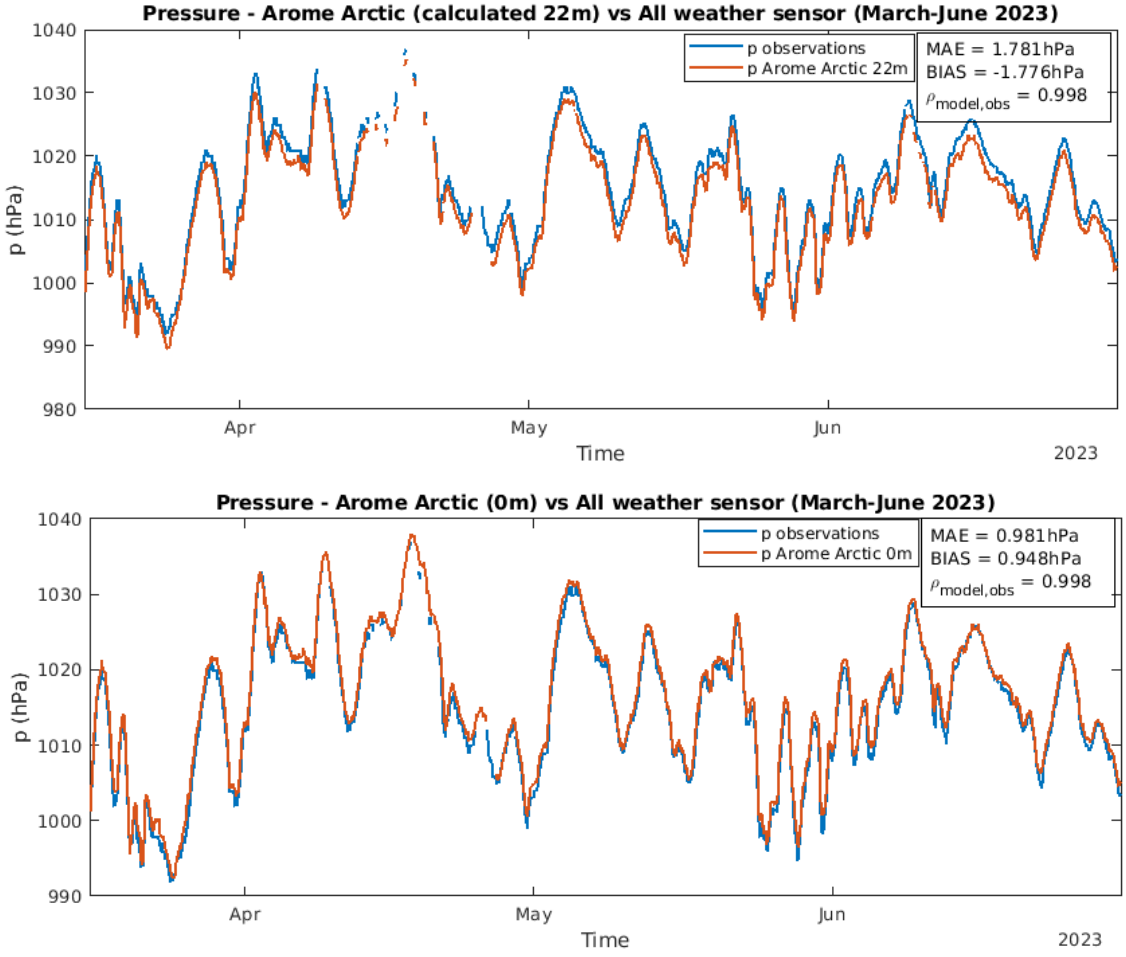

Figure 42: *Pressure from Arome Arctic at 22 m (upper panel) and at the surface (lower panel), compared to the observed pressure from the AWS. Data from Arome Arctic are shown in red lines, data from the AWS in blue lines.*

derestimation of air temperature in the model, as lower temperatures for a given amount of water vapor result in higher relative humidity.

4.10 Model verification of offshore flow case studies

4.10.1 Offshore flow case: 17 and 18 March 2023

Figure 44 shows the $\sqrt{\text{TKE}}$ from Arome Arctic interpolated to 22 m verified against the $\sqrt{\text{TKE}}$ calculated from the 3D sonic anemometer during offshore winds 17 and 18 March 2023. Even though the temporal alignment between the model and the observations are quite correlated, the observations show a relatively higher $\sqrt{\text{TKE}}$ compared to the mod-

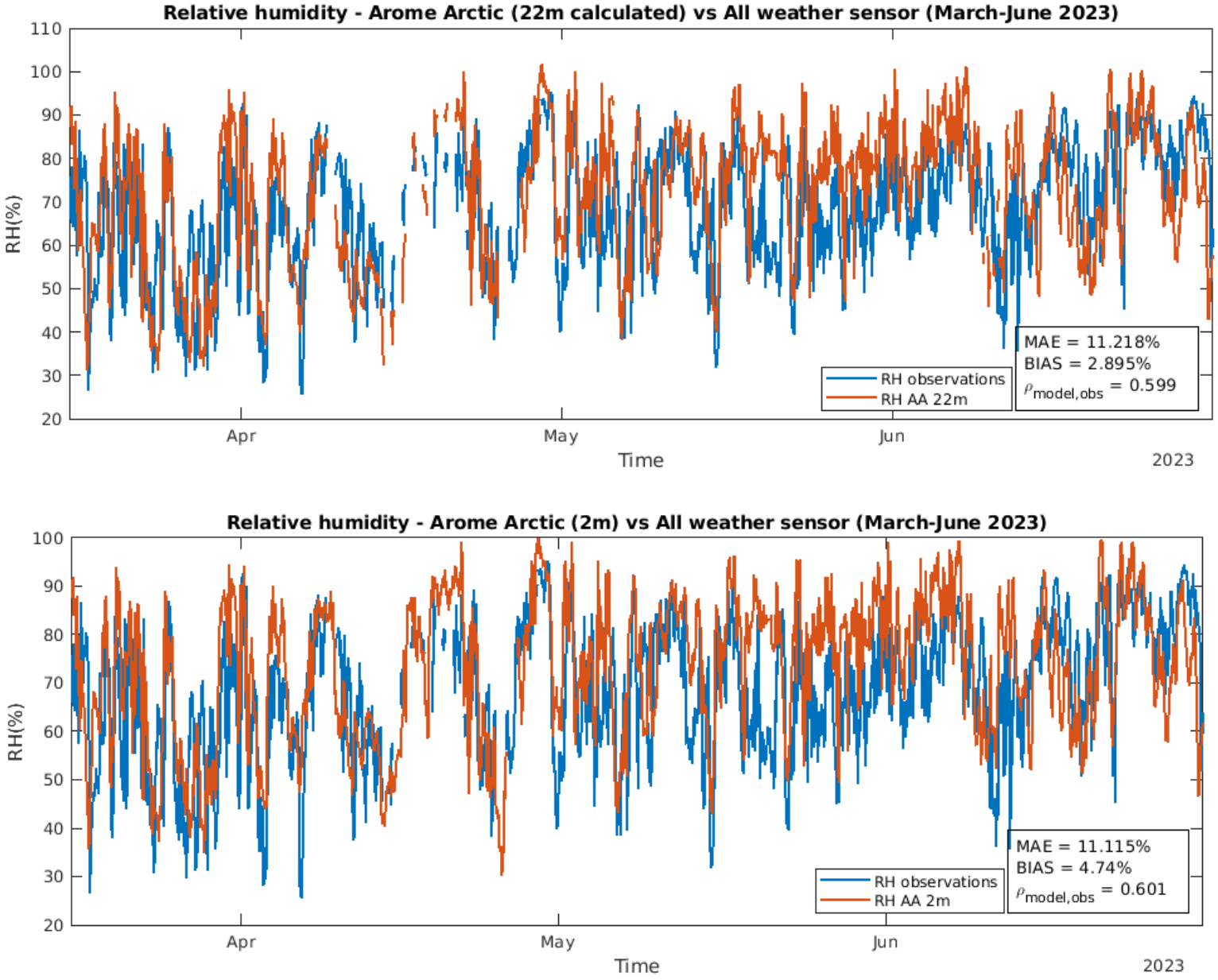

Figure 43: *Relative humidity from Arome Arctic (AA) at 22 m (upper panel) and at 2 m (lower panel), compared to the observed relative humidity from the AWS. Data from Arome Arctic are shown in red lines, data from the AWS in blue lines.*

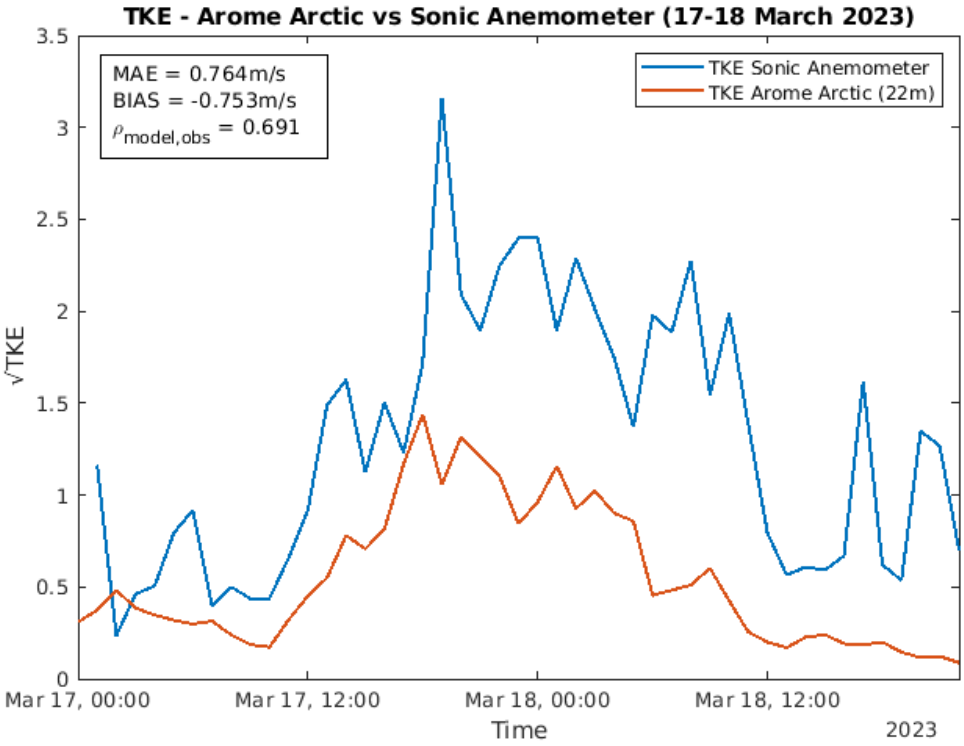

Figure 44: *$\sqrt{TKE}$ from Arome Arctic (in red) and observations from the 3D sonic anemometer (in blue) during offshore winds in the period 17 to 18 March 2023.*

elled $\sqrt{\text{TKE}}$ which is also indicated by the negative BIAS.

Figures 45 and 46 display observed wind direction and wind speed alongside Arome Arctic predictions at 10 m and interpolated to 22 m for the period from 17 to 18 March 2023, during which offshore winds prevailed. As illustrated in Figure 45, the modelled wind direction is predicted to be more southeasterly compared to the observed wind direction, which is oriented more easterly. This discrepancy may influence the $\sqrt{\text{TKE}}$ results, as the spatial resolution of the model might not adequately capture local topographical influences affecting both wind direction and $\sqrt{\text{TKE}}$. Nonetheless, at a broader scale, both model outputs and sensor measurements displayed in Figures 44 and 46 indicate increased $\sqrt{\text{TKE}}$ and wind speed during the period with easterly winds, reflecting turbulent conditions. This suggests that vertical wind velocity measurements may be more reliable under offshore flow conditions than during southwesterly winds, when airflow directed toward the barge likely increases upward vertical wind speeds.

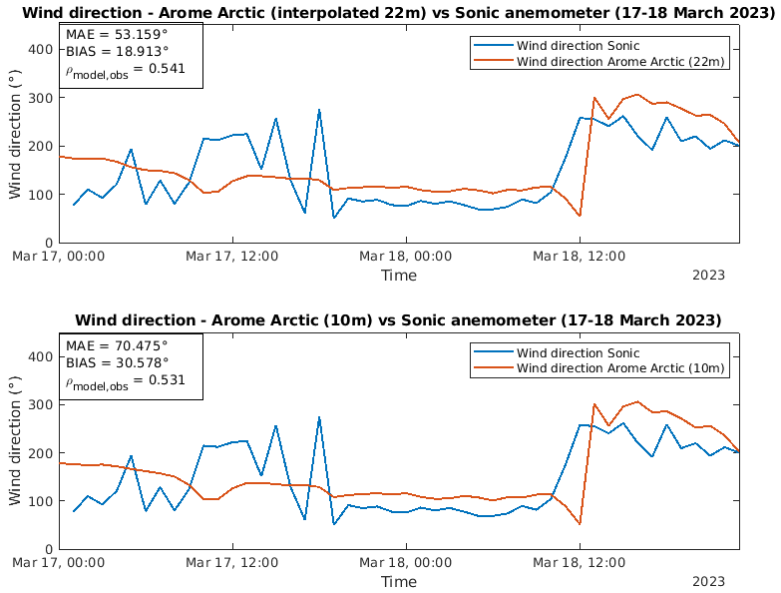

Figure 45: *Wind direction from Arome Arctic at 22 m (upper panel) and at 10 m (lower panel) compared to observed wind direction from the 3D sonic anemometer during offshore winds from 17 to 18 March 2023. Data from Arome Arctic are shown in red lines, data from the 3D sonic anemometer in blue lines. The wind direction comparison method is described in Section 4.4.*

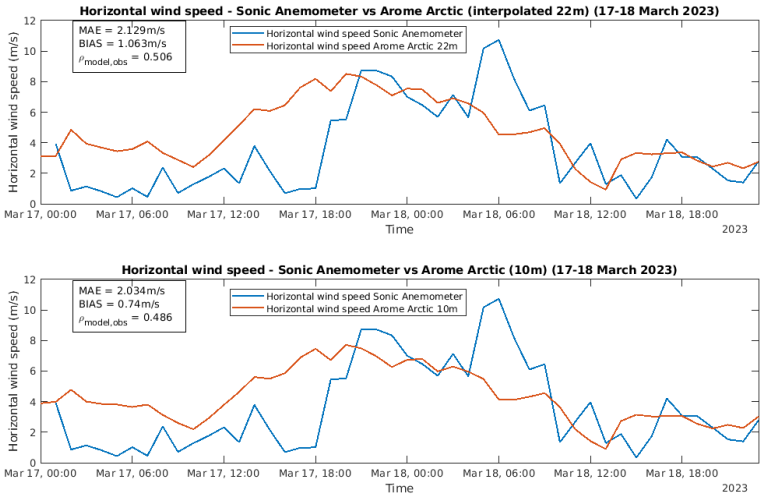

Figure 46: *Wind speed from Arome Arctic at 22 m (upper panel) and at 10 m (lower panel) compared to observed wind speed from the 3D sonic anemometer during offshore winds 17 and 18 March 2023. Data from Arome Arctic are shown in red lines, data from the 3D sonic anemometer in blue lines.*

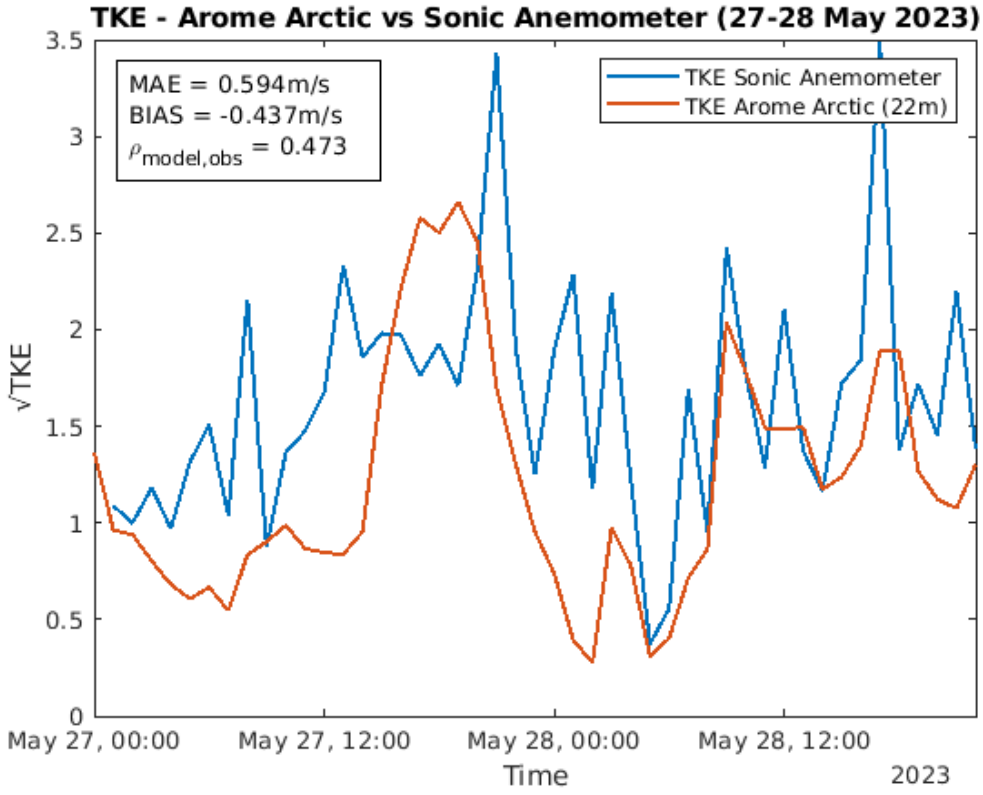

Figure 47: *$\sqrt{TKE}$ from Arome Arctic (in red) and observations from the 3D sonic anemometer (in blue) during offshore winds 27 and 28 May 2023.*

4.10.2 Offshore flow case: 27 and 28 May 2023

Figure 47 compares the $\sqrt{\text{TKE}}$ from Arome Arctic, interpolated to 22 m, with $\sqrt{\text{TKE}}$ calculated from the 3D sonic anemometer during another offshore-flow event from 27 to 28 May 2023. Compared to the previous offshore-flow event, the modelled $\sqrt{\text{TKE}}$ in this case shows a smaller negative BIAS and a reduced MAE. However, the model forecasts the observed peak in $\sqrt{\text{TKE}}$ on the evening of 27 May 2023 earlier than it occurs, which negatively impacts the correlation coefficient in this case.

Figures 48 and 49 present the observed wind direction and wind speed, alongside the Arome Arctic model outputs at 10 m and 22 m heights for 27 and 28 May 2023. As illustrated in Figure 48, the modelled wind direction tends to be more southerly relative to the observed wind direction, which exhibits a more easterly component. Despite the discrepancy in wind direction, the modelled and observed wind speeds, along with the $\sqrt{\text{TKE}}$ depicted in Figures 49 and 47, demonstrate a notable degree of agreement in capturing moderate wind and turbulent conditions. This case thus represents another instance

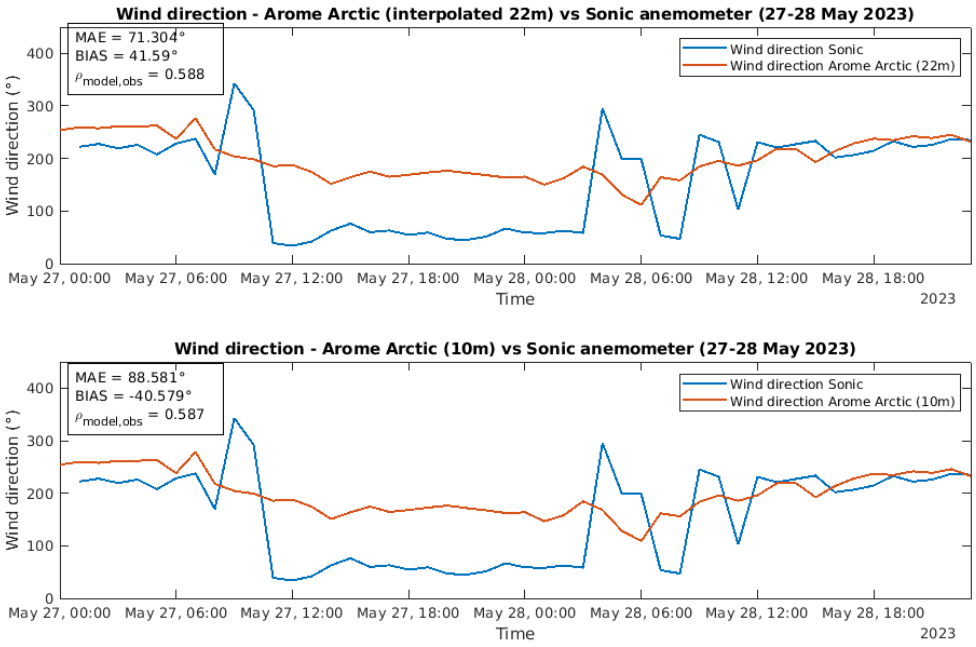

Figure 48: *Wind direction from Arome Arctic at 22 m (upper panel) and at 10 m (lower panel) compared to observed wind direction from the 3D sonic anemometer during offshore winds from 27 to 28 May 2023. Data from Arome Arctic is shown in red lines, data from the 3D sonic anemometer in blue lines.*

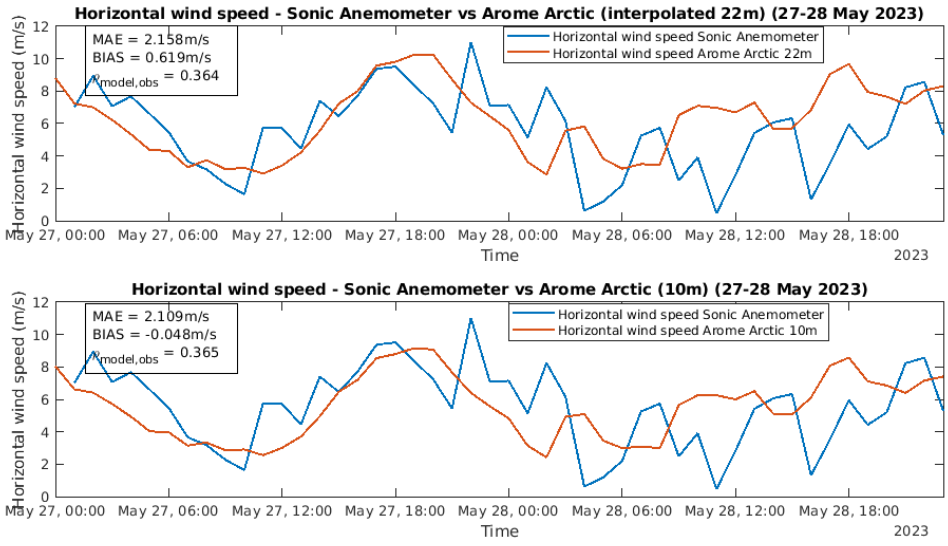

Figure 49: *Wind speed from Arome Arctic at 22 m (upper panel) and at 10 m (lower panel) compared to observed wind speed from the 3D sonic anemometer during offshore winds 27 and 28 May 2023. Data from Arome Arctic are shown in red lines, data from the 3D sonic anemometer in blue lines.*

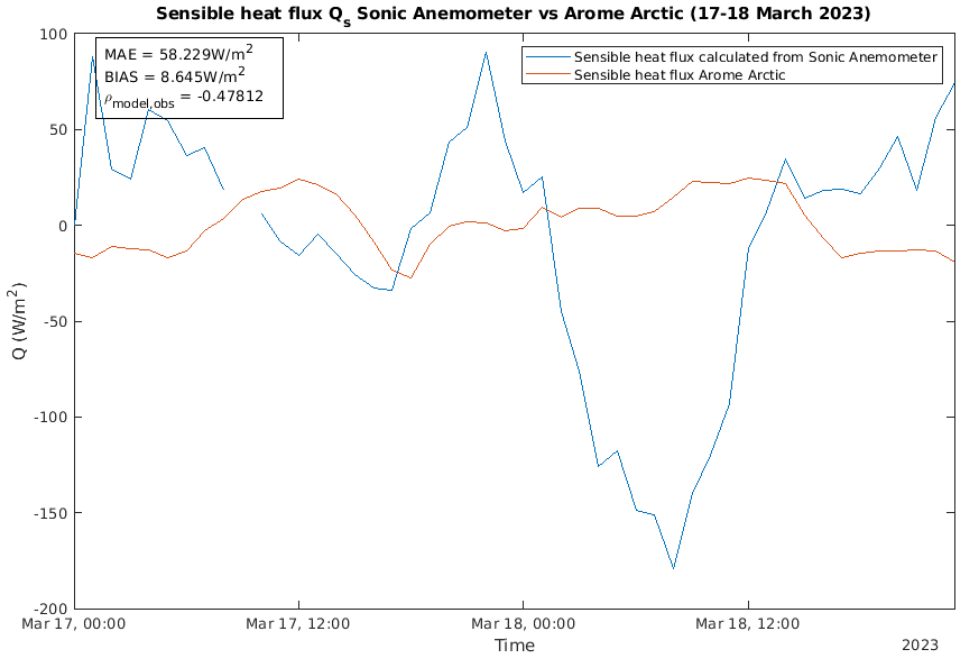

Figure 50: *Sensible heat flux from Arome Arctic (in red) and observations from the 3D sonic anemometer (in blue) during offshore winds 17 and 18 March 2023.*

of offshore flow conditions, under which vertical wind velocity predictions are generally more reliable than during southwesterly flow events. For this reason, a short sensible heat flux analysis for the two offshore-flow cases are presented in the next section.

4.10.3 Sensible heat flux analysis for the two offshore flow cases

Since the vertical velocity is more reliable during offshore flow compared to weather situations when the horizontal wind is from other directions, the sensible heat flux is calculated for offshore-flow periods and the result is visualized in Figures 50 and 51. The figures illustrate raw measurements from the 3D sonic anemometer in combination with Arome Arctic model data during the offshore-flow events of 17–18 March and 27–28 May 2023. Negative sensible heat flux typically signifies statically stable atmospheric conditions, whereas positive values are indicative of instability. As shown in Figure 50, the model does not reproduce the pronounced negative sensible heat flux observed during the morning of 18 March, highlighting difficulties in accurately simulating the stability regime. During winter months, when snow covers the ground, strong static stability can develop at night and in the early morning under clear-sky conditions over land. In off-

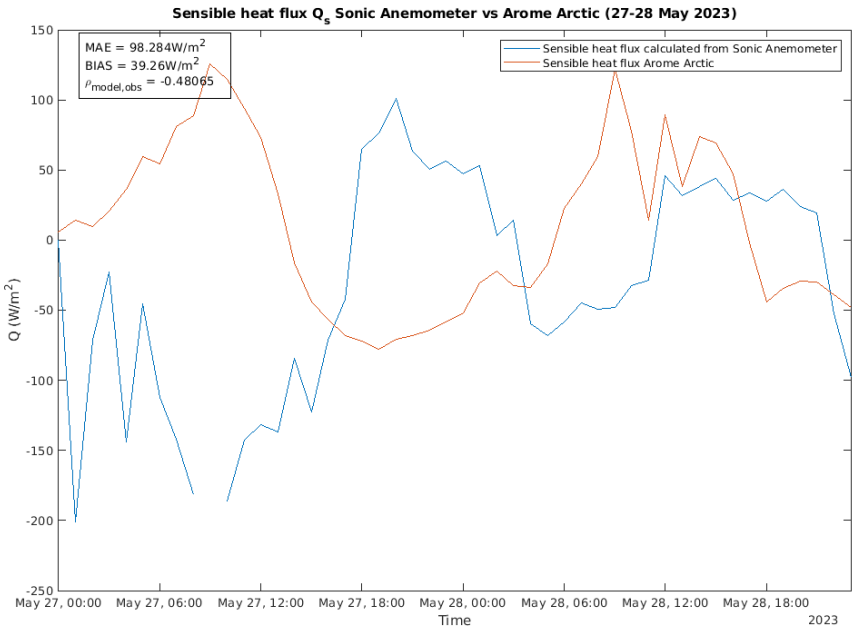

Figure 51: *Sensible heat flux from Arome Arctic (in red) and observations from the 3D sonic anemometer (in blue) during offshore winds 27 and 28 May 2023.*

shore flow conditions, this stable regime can influence the measurement site where the 3D sonic anemometer is located, which occurred during certain periods on 17 and 18 March. On the other hand, when land surfaces are largely snow-free and warmed by solar radiation under mostly clear-sky conditions during late spring and summer, an unstable regime can develop over land. During offshore flow, this leads to opposite conditions at the measurement site, with positive sensible heat fluxes instead of the negative values typically associated with stable regimes (Figure 51). In addition, during onshore flow conditions, the advection of relatively cold air from the sea toward the measurement site can increase static stability, resulting in negative sensible heat flux values, as observed at the beginning of 27 May (Figure 51).

However, several factors may contribute to the relatively low correlation between the modelled and observed sensible heat flux during such events. These include limited resolution of atmospheric stability in the model and strong local variations in sensible heat flux that are not accurately captured by the model system. Moreover, the extracted model data is bilinearly interpolated from nearby grid points and is thus dependent on the surface characteristics of these grid points. As an example, Figure 52 displays the sensible heat flux in Arome Arctic at 27 May 1200 UTC. The red cross displays the location of

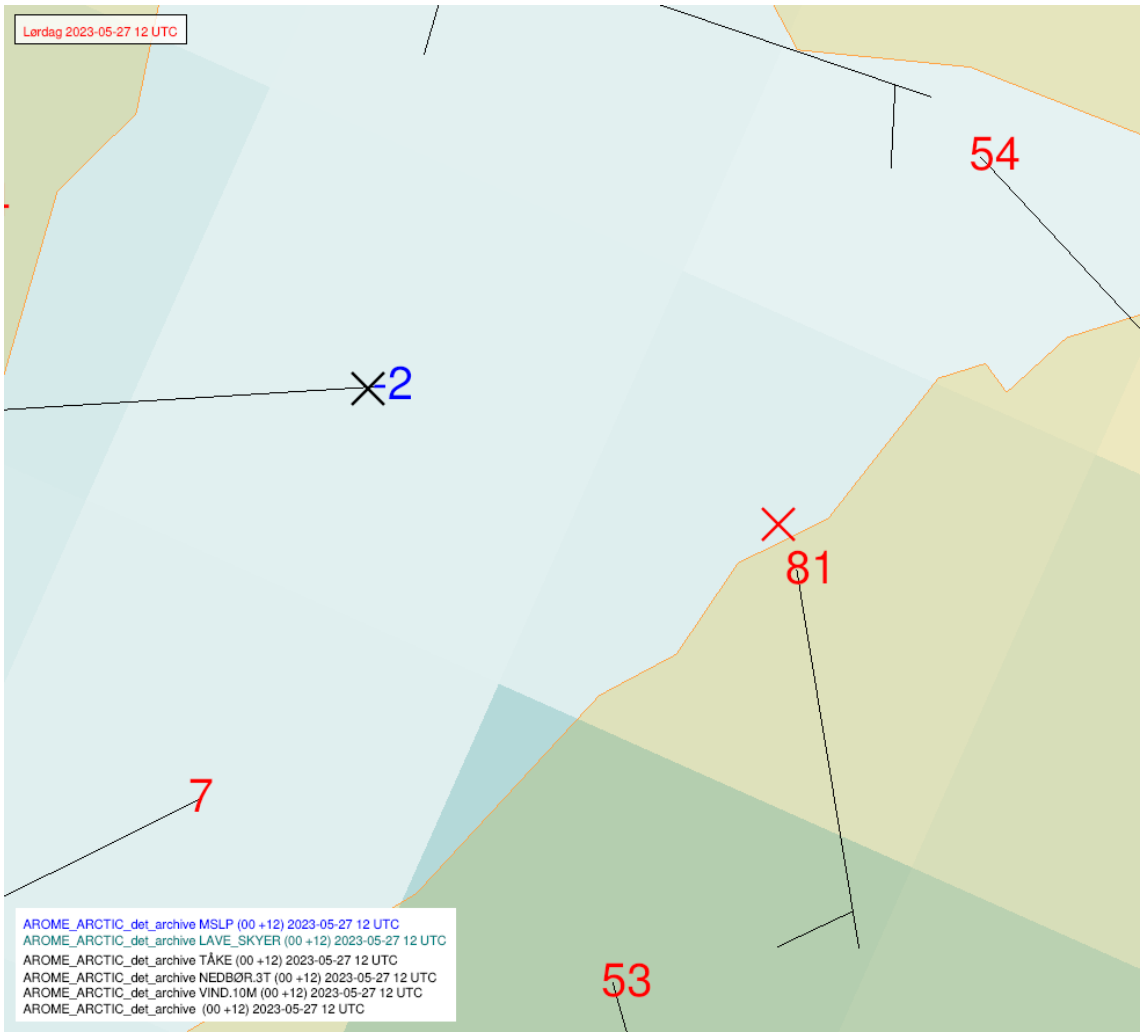

Figure 52: *Sensible heat-flux values (positive in red and negative in blue) from grid points in Arome Arctic 27 May 2023 at 1200 UTC. The red cross marks the position of the feeding barge, while the black cross marks a position with mostly sea characteristics.*

the feeding barge which is used to extract the data from the model. On the other hand, the numbers in the figure represent the grid points where the sensible heat flux is calculated, and these points are dependent on the underlying physiography, particularly whether the grid point in consideration consists of land or sea characteristics or so-called land or sea tiles. The extracted sensible heat flux will in this situation be mostly influenced by the closest data point on land closest to the red cross. In order to address this challenge, a grid point that reflects mostly oceanic conditions is also selected and plotted (black cross in Figure 52) to see whether the correlation between the observed and modelled sensible heat flux is stronger when the observation point is compared to a sea point instead of a

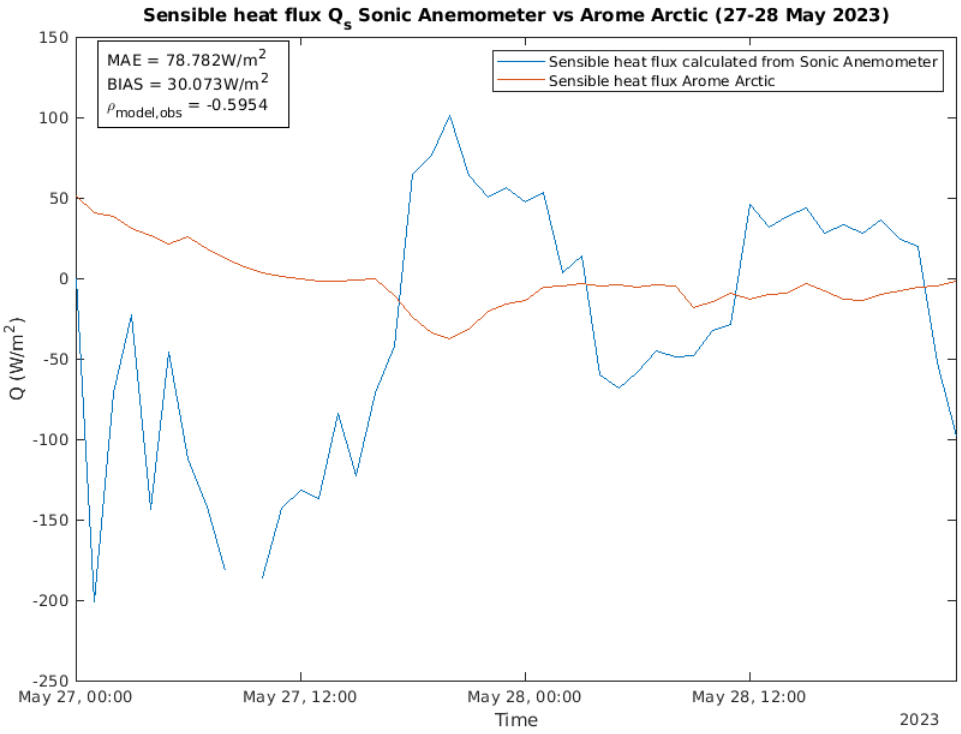

Figure 53: *Sensible heat flux from Arome Arctic (in red) at the location of the black cross with sea characteristics in Figure 52 and observations from the 3D sonic anemometer (in blue) during offshore winds 27-28 May 2023.*

point mostly influenced by land characteristics.

Figure 53 demonstrates a comparison of sensible heat flux between the observation site and the nearest sea grid point in the Arome Arctic model. At this model location, the large positive sensible heat flux values observed at the beginning of both days (as shown in Figure 51) are not reflected. Additionally, the model does not capture the observed positive values during nighttime at this point. Nonetheless, these results highlight the strong sensitivity of the modelled sensible heat flux to the surface characteristics of the specific grid cell under consideration.

Furthermore, to assess whether the correlation between modelled and observed sensible heat flux improves when using a grid point characterized by sea surface properties, Figure 54 shows a comparison of sensible heat flux between the observations and the corresponding sea grid point in the Arome Arctic model for the case of 17 to 18 March 2023. Compared to the previous comparison (Figure 50), the model appears to better capture the peak in sensible heat flux during the late evening of 17 March when using the

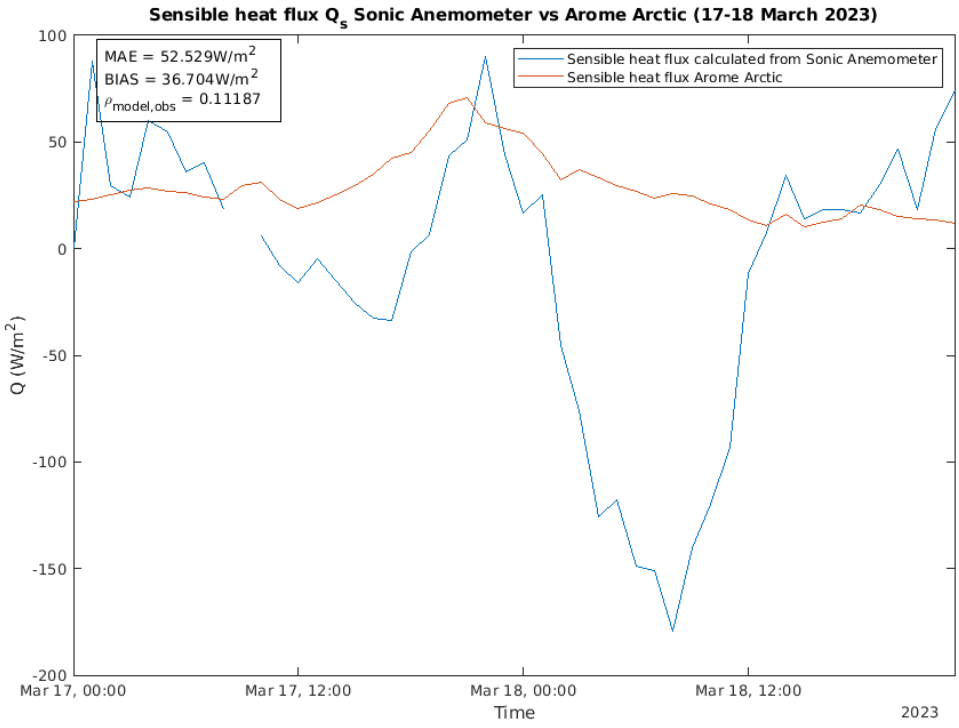

Figure 54: *Sensible heat flux from Arome Arctic (in red) at the location of the black cross with sea characteristics in Figure 52 and observations from the 3D sonic anemometer (in blue) during offshore winds 17-18 March 2023.*

sea-characterized grid point. However, the model still fails to reproduce the pronounced negative flux observed during the morning of 18 March.

5 Results from 1 July 2023 to 14 November 2023

Since the evaluation of the first period shows deficiencies in the data from some of the observed variables, only data from the most reliable quantities are inspected and presented for this next period. However, there are some missing data in August and October which should be considered when applying the data.

5.1 Data from the AWS

Figure 55 presents the temperature, dew-point temperature, air pressure, and relative humidity from the AWS from 1 July 2023 to 14 November 2023. It is clear that the temperature and the dew-point temperature is decreasing from September and throughout this period, with some warmer periods in between, which seems natural and reliable going from summer towards winter.

Figure 56 shows the longwave and shortwave radiation from the net radiometer, in conjunction with temperature and relative humidity from the AWS. The data indicate that the incoming shortwave radiation significantly decreases during the period along with the temperature. This reduction in short wave radiation is due to lower sun elevation angle and even lack of sunshine in the study area during late autumn and early winter, resulting in lower temperatures compared to the summer time. However, similar to Figure 9 in Section 4.1, Figure 56 indicates that the longwave radiation coming from below is higher than the longwave radiation coming from the atmosphere except during a warm

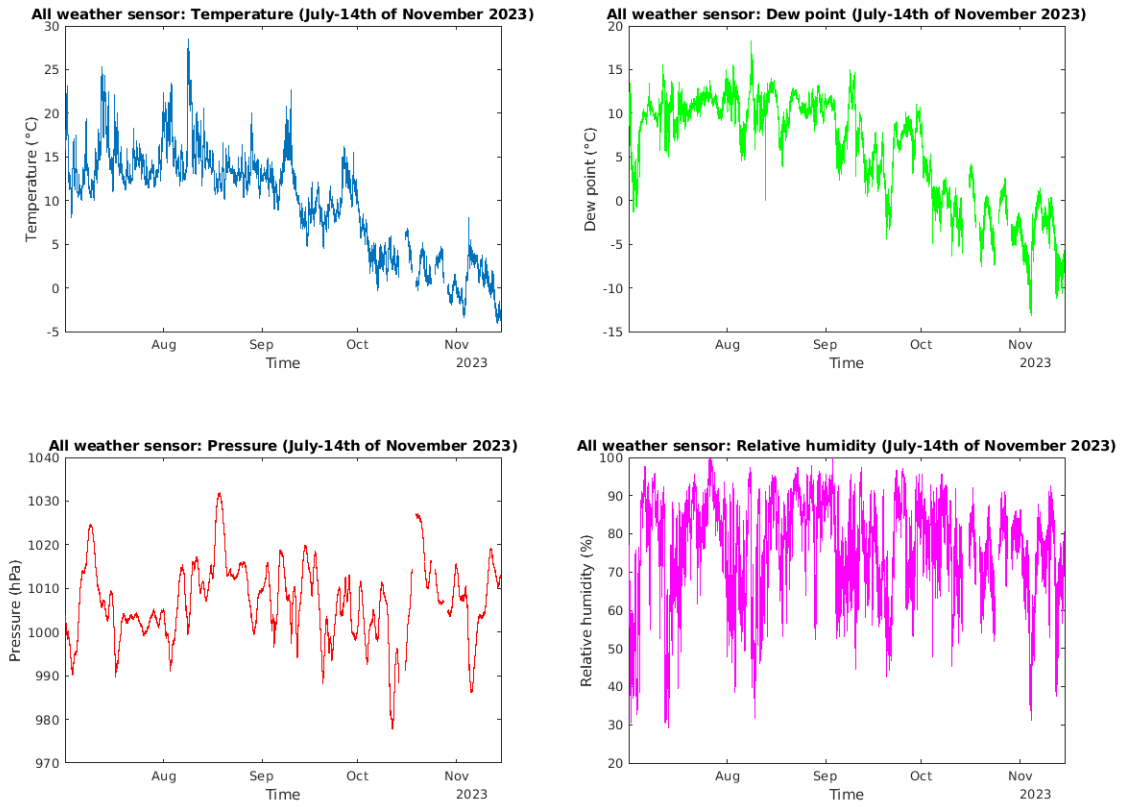

Figure 55: *Temperature (in blue), dew-point (in green), air pressure (in red), and relative humidity (in pink) from the AWS from 1 July to 14 November 2023.*

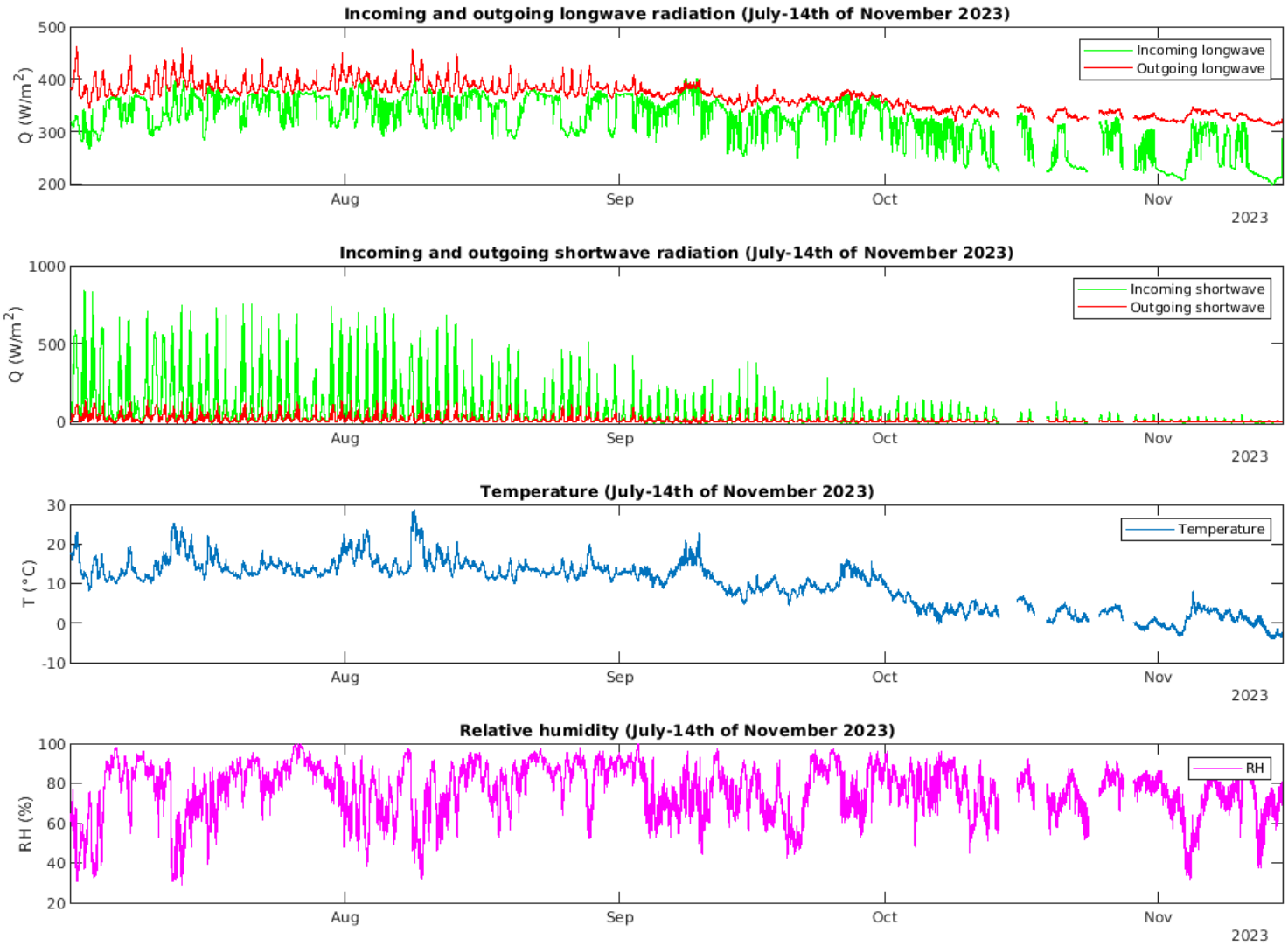

Figure 56: *Longwave and shortwave radiation from the net radiometer, in conjunction with temperature and relative humidity from the AWS for the period 1 July to 14 November 2023.*

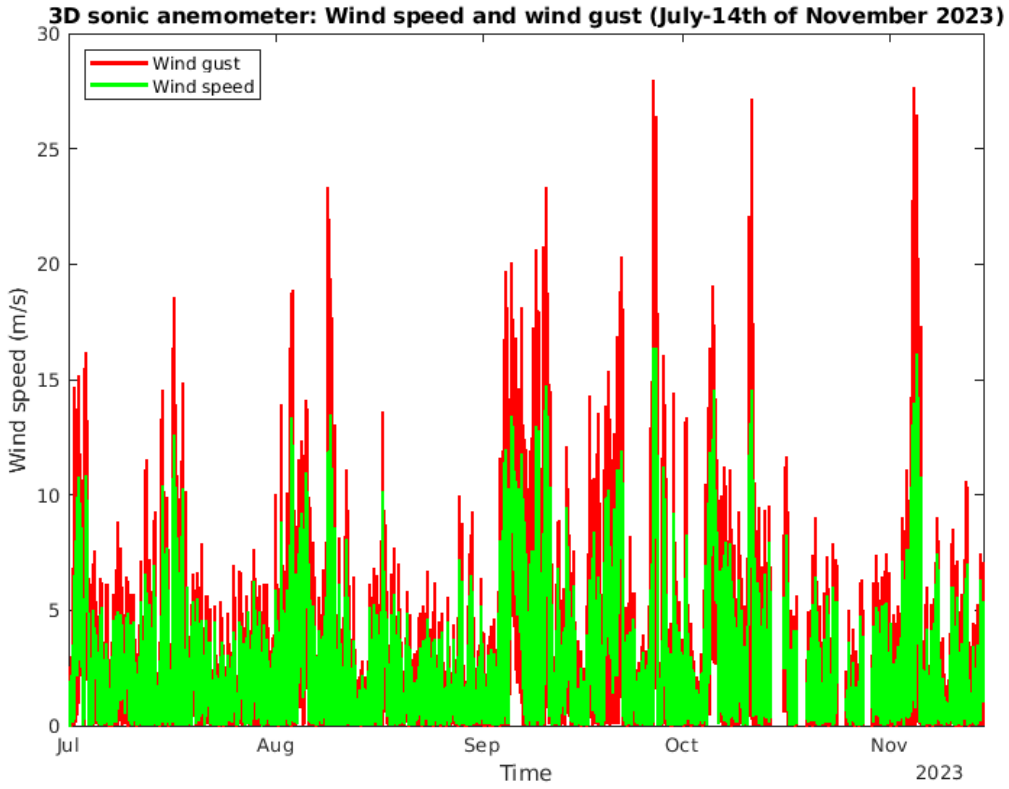

Figure 57: *Horizontal wind speed (in green) and wind gust (in red) from the 3D sonic anemometer for the period 1 July to 14 November 2023.*

period in September where the atmosphere has higher temperature than the sea, but also higher temperature (and longwave radiation) than the feeding barge below the instrument (Figure 29).

5.2 Wind speed and wind direction

Figure 57 displays the 10 minute mean horizontal wind speed together with the wind gusts from the 3D sonic anemometer. Similar to Figure 10, there are wind gusts above 20 m/s, but no observations of mean wind speed above 20 m/s. This indicates a high degree of wind variability and turbulent conditions during some time periods.

Figure 58 presents the wind direction and wind speed derived from the AWS. It illustrates, similar to Figure 57, high wind speeds in some periods in September, October, and November.

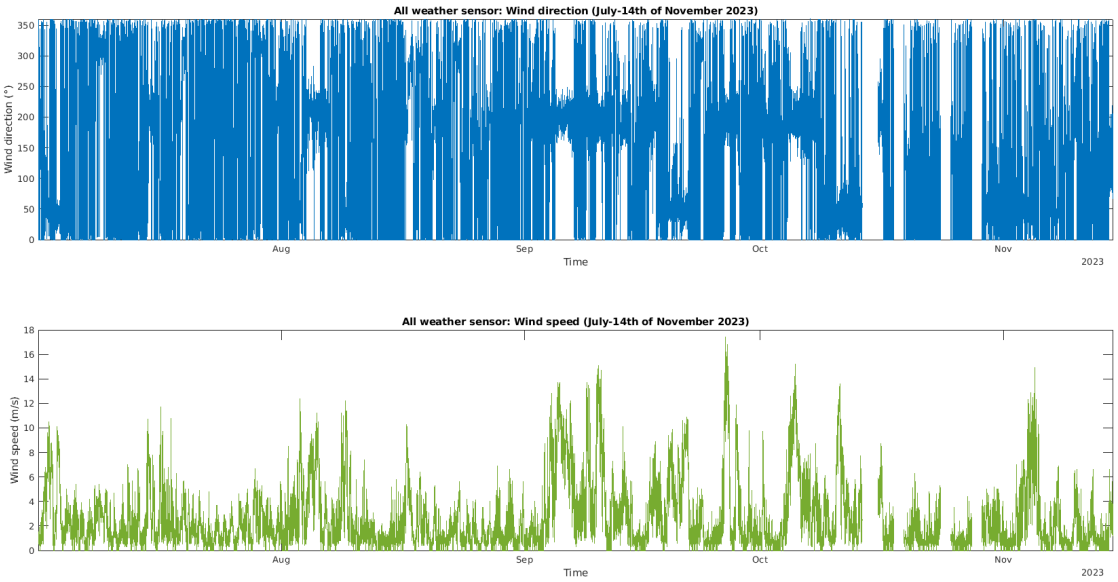

Figure 58: *Wind direction (upper panel) and wind speed (lower panel) from the AWS for the period 1 July to 14 November 2023.*

5.3 Case-based analyses of vertical wind speed in offshore flow events

Figures 59, 60, and 61 highlight three periods characterized by offshore flow. The purpose is to further examine whether the feeding barge disturbance, which is likely associated with southwesterly winds (see Section 4.3), could also occur during offshore flow events in this second time period.

5.3.1 Offshore flow case: 1 and 2 July 2023

Figure 59 displays the instantaneous vertical wind component, here called vertical wind gust, and the wind direction during 1 and 2 July 2023. The strongest negative vertical velocities are between the afternoon to midnight of 1 July before the wind backs slightly more north during 2 July. The period before the wind backs north, has, similar to the cases in the period from March to June, a mirroring magnitude in the positive and negative vertical velocities. This indicates that the observed vertical velocities are not only related to the feeding barge disturbance, but might also be due to the presence of mountain waves during easterly flow.

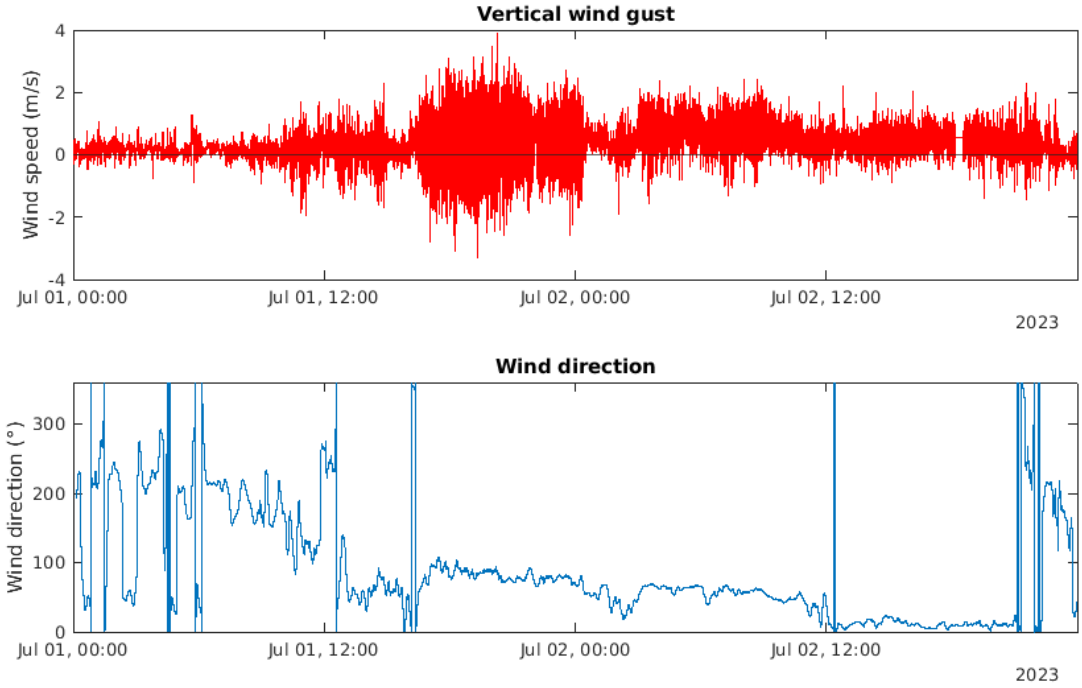

Figure 59: *A case comparison of vertical wind gust (upper panel) and wind direction (lower panel) during 1 and 2 July 2023.*

5.3.2 Offshore flow case: 19 to 22 September 2023

Figure 60 illustrates the vertical wind gusts during a period of predominantly offshore flow from 19 to 22 September 2023. The data show pronounced negative vertical velocities accompanied by positive velocities of similar magnitude, which may indicate the presence of mountain wave activity under these conditions. The repeated pattern across various time periods suggests that these observations represent a persistent aspect of offshore wind conditions, rather than isolated anomalies.

5.3.3 Offshore flow case: 10 to 12 October 2023

Figure 61 shows vertical wind velocities and wind direction for the period 10 to 12 October 2023. The observed pattern further reinforces the findings from Figures 60 and 59, with distinct similarities in the magnitudes of negative and positive vertical velocities during easterly flow. However, after 12 October 00:00 UTC, a period of easterly winds occurs with less pronounced fluctuations in the vertical wind component. This further demonstrates that offshore flow is not necessarily associated with mountain waves, which are typically characterized by fluctuating vertical velocities that affect the feeding barge.

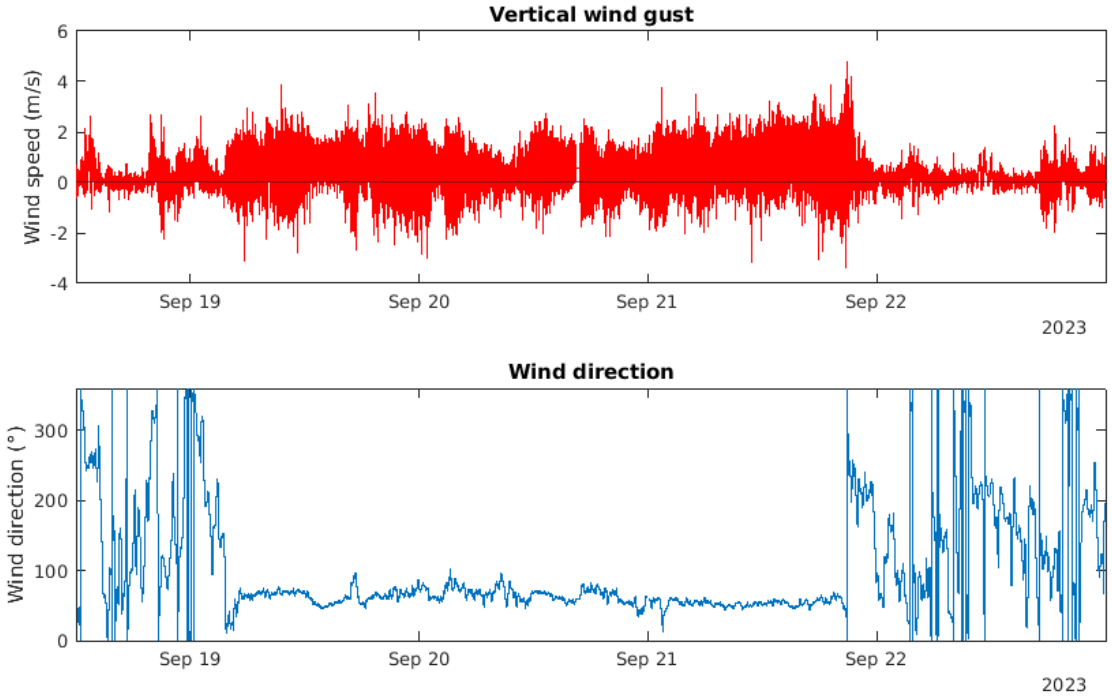

Figure 60: *A case comparison of vertical wind gust (upper panel) and wind direction (lower panel) in the period 19 to 22 September 2023.*

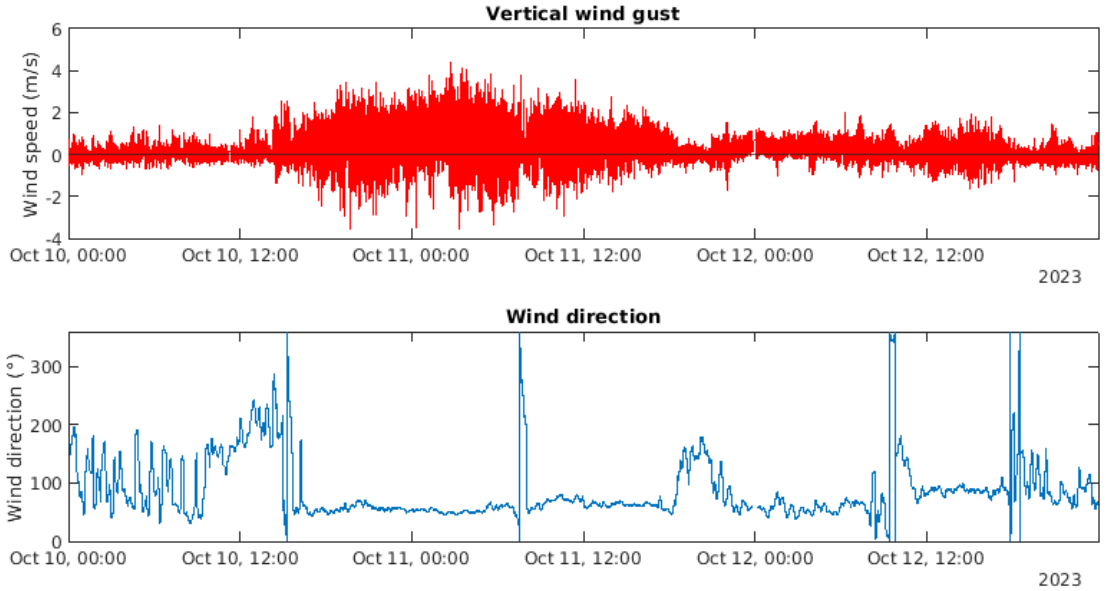

Figure 61: *A case comparison of vertical wind gust (upper panel) and wind direction (lower panel) in the period 10 to 12 October 2023.*

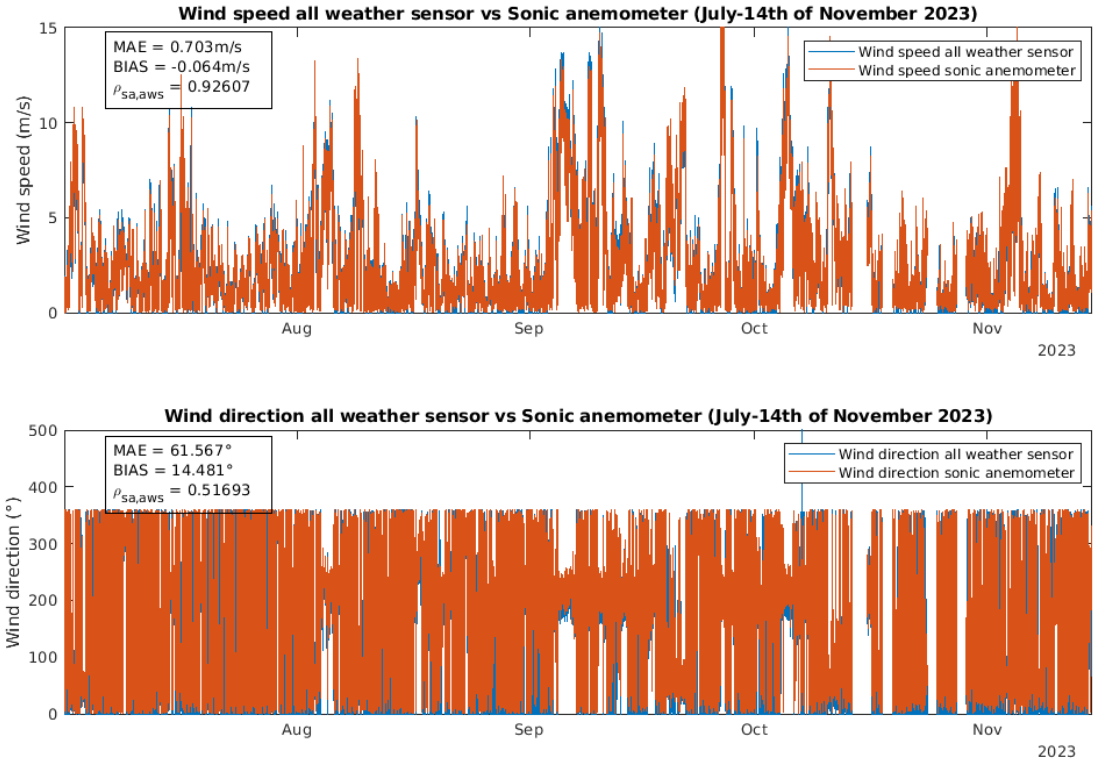

Figure 62: *Comparison of the wind speed (upper panel) and wind direction (lower panel) between the 3D sonic anemometer (in red) and the AWS (in blue) in the period 1 July to 14 November 2023.*

5.4 Horizontal wind comparison

Figure 62 shows wind speed and direction measurements from both the 3D sonic anemometer and the AWS for the time period under consideration. Compared to the March–June period (Figure 21), the absolute differences between the wind measurements from the two instruments are slightly larger, and the correlation is somewhat weaker. Nevertheless, the correlation coefficient for wind speed remains high, at 0.93.

For the wind direction comparison, the same method from Jiménez and Dudhia (2013), as discussed in Section 4.4, is applied. For this time period the 3D sonic anemometer is backed 15 degrees relative to the AWS wind direction, which is evident when inspecting the wind roses in Figure 63. This is a lower BIAS compared to the BIAS observed in the period from March to June, however the MAE for the wind direction during this time period is higher than the MAE from June to March (62 degrees versus 43 degrees). This suggests that during the last period there is a greater variability in wind direction which is typical for the summer time period. Note that the high-frequency peak of weak winds

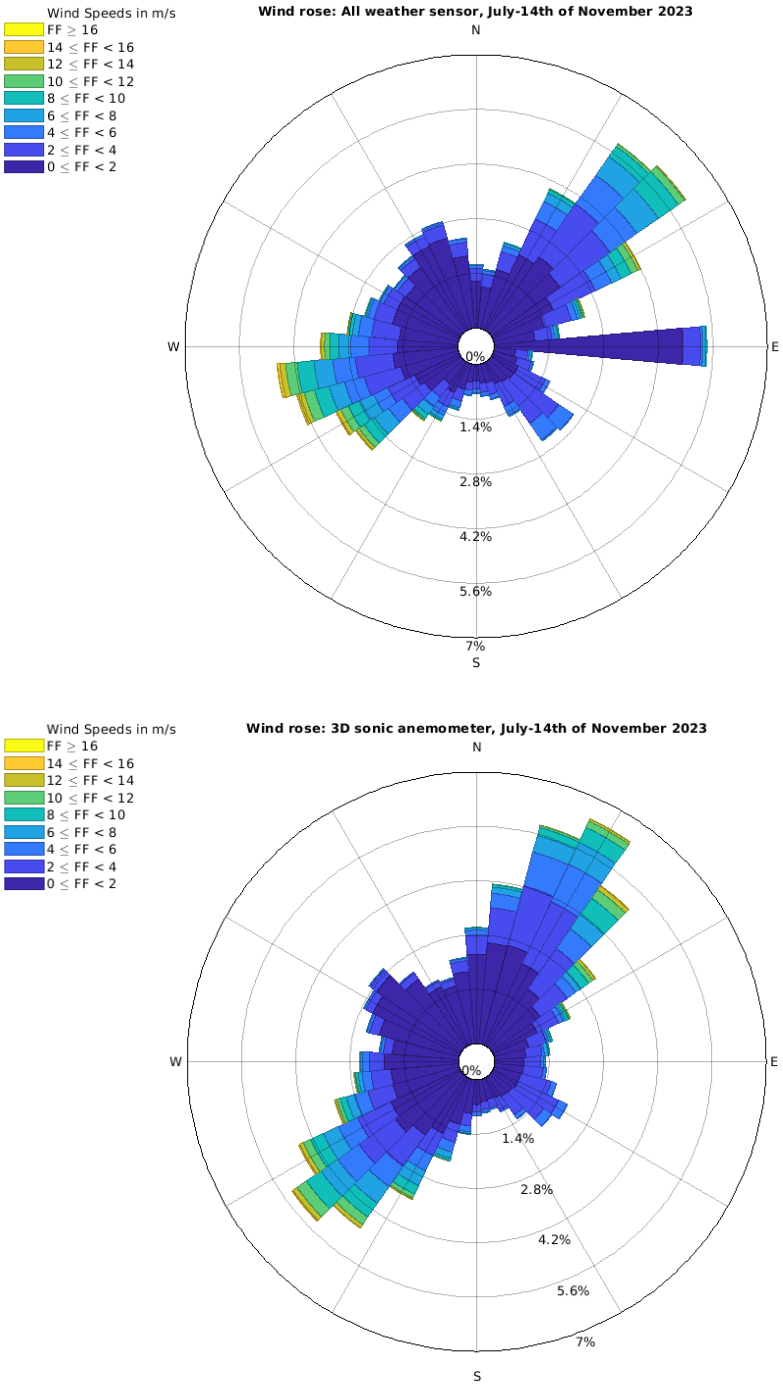

Figure 63: *Wind rose based on wind direction and wind speed from the AWS (upper panel) and the 3D sonic anemometer (lower panel) in the period 1 July to 14 November 2023. The wind rose is retrieved by using the MATLAB (The MathWorks Inc., 2023) function from Pereira (2023).*

from the east in the AWS is probably due to some local disturbances on the feeding barge affecting the AWS wind direction, but not the 3D sonic anemometer. This is also apparent in the wind rose from the previous period (see Figure 22).

5.5 Case-based analyses of TKE in offshore flow events

Due to the unrealistic high positive vertical velocities observed during southwesterly flow, this section presents the TKE only from some selected offshore flow events, as is also presented in Section 5.3.

5.5.1 Offshore flow case: 1 and 2 July 2023

Figure 64 presents $\sqrt{\text{TKE}}$, wind direction, and wind speed for 1 and 2 July 2023. A notable increase in both $\sqrt{\text{TKE}}$ and wind speed is observed during the period of easterly flow, from midday on 1 July until midnight, before the wind direction begins to gradually shift toward the north. After midnight, $\sqrt{\text{TKE}}$ decreases while wind speed continues to increase, with the wind backing further to the north, particularly during the afternoon of

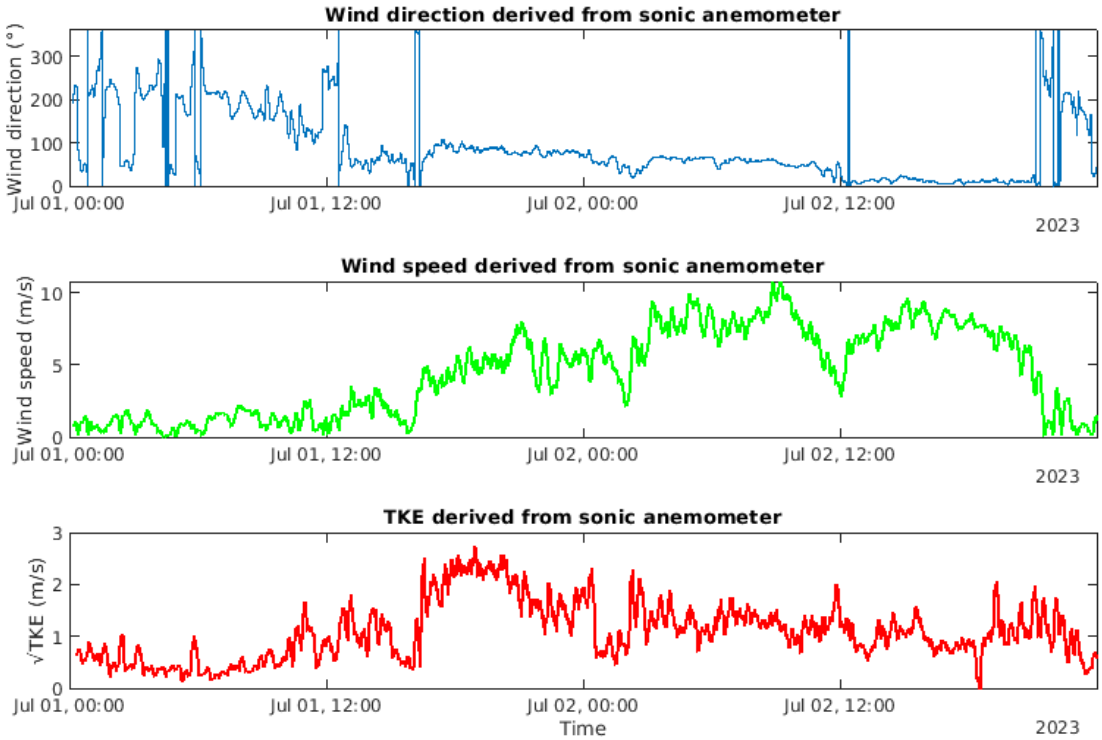

Figure 64: *Wind direction (in blue), wind speed (in green), and $\sqrt{TKE}$ (in red) for 1 and 2 July 2023.*

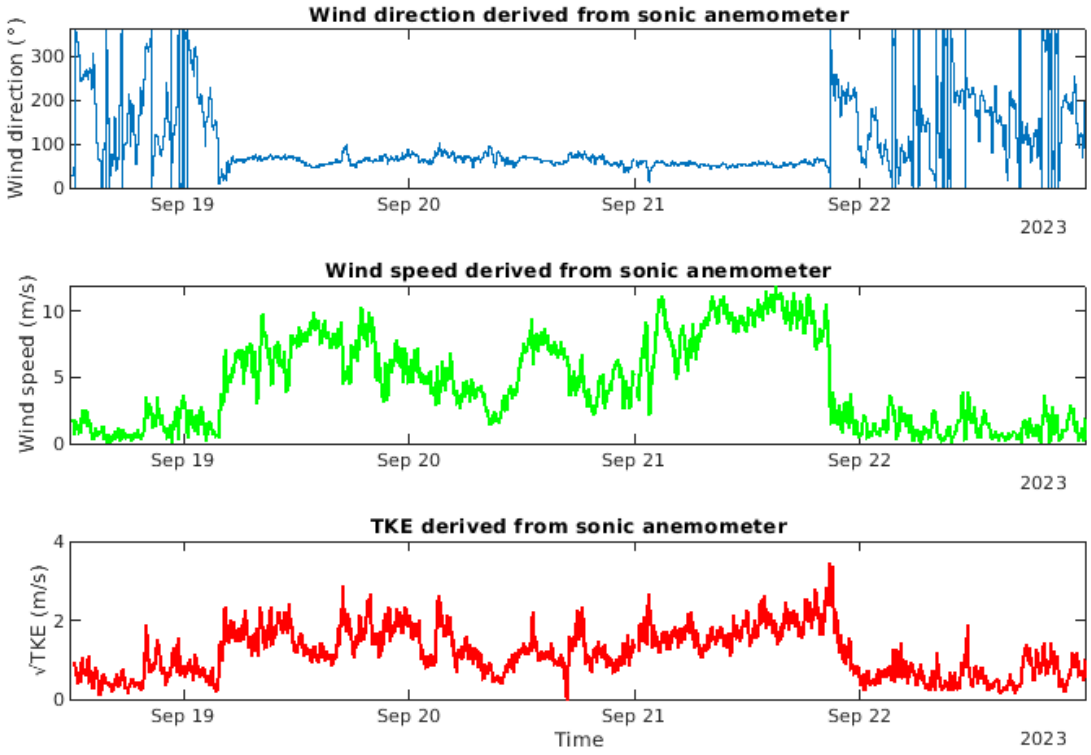

Figure 65: *Wind direction (in blue), wind speed (in green), and* $\sqrt{TKE}$ *(in red) in the period 19 to 22 September 2023.*

2 July. As shown in Figure 59, strong negative vertical velocities occur primarily before midnight during the easterly flow, while weaker negative velocities are seen afterward, coinciding with a more northeasterly to northerly wind direction. This supports the interpretation that mountain waves are likely present during periods of easterly flow in this specific case.

5.5.2 Offshore flow case: 19 to 22 September 2023

Figure 65 depicts the $\sqrt{\text{TKE}}$, the wind direction, and the wind speed for the period 19 to 22 September 2023. Throughout most of this period, relatively stable offshore flow is present, and a clear association is observed between this persistent northeast to easterly flow and elevated values of both wind speed and $\sqrt{\text{TKE}}$. A marked decrease in $\sqrt{\text{TKE}}$ and wind speed occurs toward the end of 21 September, coinciding with a shift in wind direction and a transition in the flow regime.

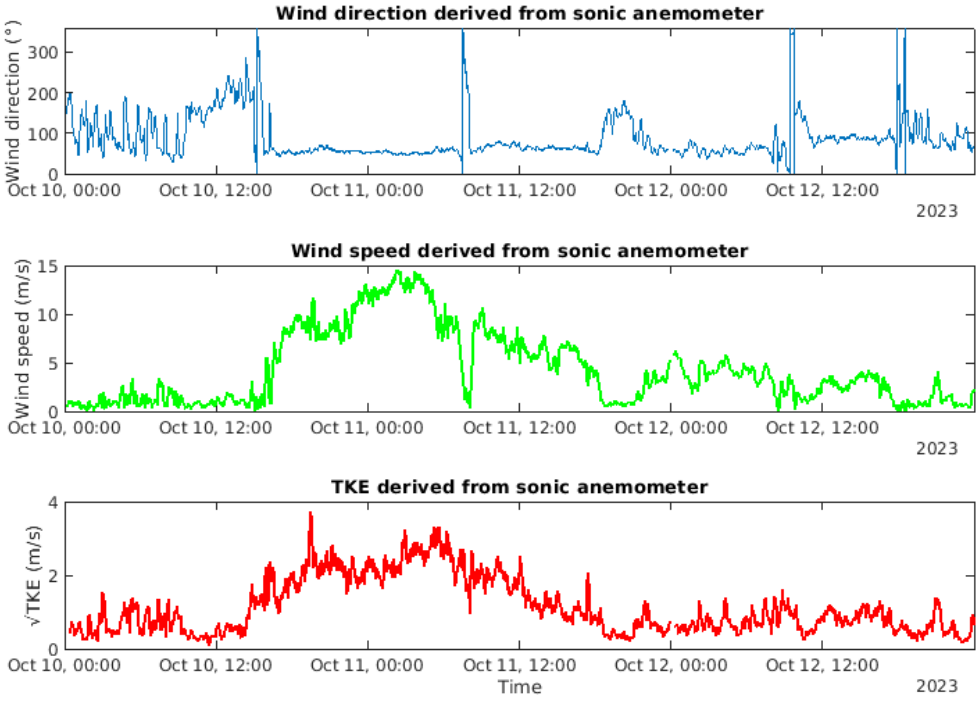

Figure 66: *Wind direction (in blue), wind speed (in green), and* $\sqrt{TKE}$ *(in red) in the period 10 to 12 October 2023.*

5.5.3 Offshore flow case: 10 to 12 October 2023

Similarly, Figure 66, which depicts wind direction, wind speed, and $\sqrt{\text{TKE}}$, shows elevated values of both wind speed and $\sqrt{\text{TKE}}$ from noon on 10 October until the evening of 11 October. However, as noted in Section 5.3.3, a period of easterly winds occurs early on 12 October that is not associated with mountain wave activity. Notably, this period also corresponds to lower $\sqrt{\text{TKE}}$ values. The consistency of these observations across multiple time periods supports the hypothesis that offshore winds often, but not always, generate mountain waves and enhance turbulent conditions. When considered alongside the earlier observations of vertical wind velocities in Figures 59, 60 and 61, these results suggest that $\sqrt{\text{TKE}}$ values during offshore flow provide a more reliable representation of turbulence compared to those obtained during southwesterly wind conditions.

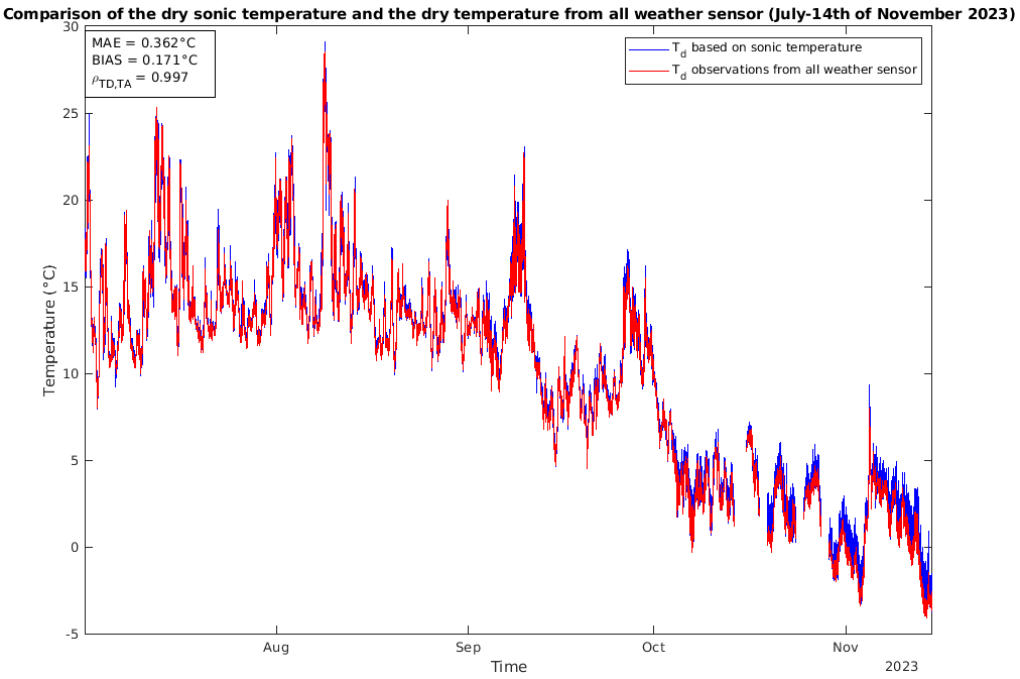

Figure 67: *The dry temperature (T_d) derived from the 3D sonic anemometer and the AWS (in blue) and the measured temperature from the AWS (in red) compared for the period 1 July to 14 November 2023.*

5.6 Dry temperature comparison

Figure 67 compares the calculated dry temperature derived from the T_s from the 3D sonic anemometer and the RH from the AWS (see Section 3.3), and the temperature measured by the AWS. As is shown in the figure, the mean absolute difference is 0.36°C. This is a slightly higher value than in the period from March to June (see Figure 26), but the correlation coefficient between the temperatures is still high (0.997) for this second time period in consideration.

5.7 Model verification

5.7.1 Horizontal wind

The wind roses in Figure 68 illustrate wind direction and wind speed from the Arome Arctic model at 22 m and 10 m heights and can be compared to the wind rose based on data from the 3D sonic anemometer shown in the lower panel of Figure 63. A comparison of these figures reveals that the observed wind from the 3D sonic anemometer shows a higher frequency of northeasterly and southwesterly directions relative to the wind direc-

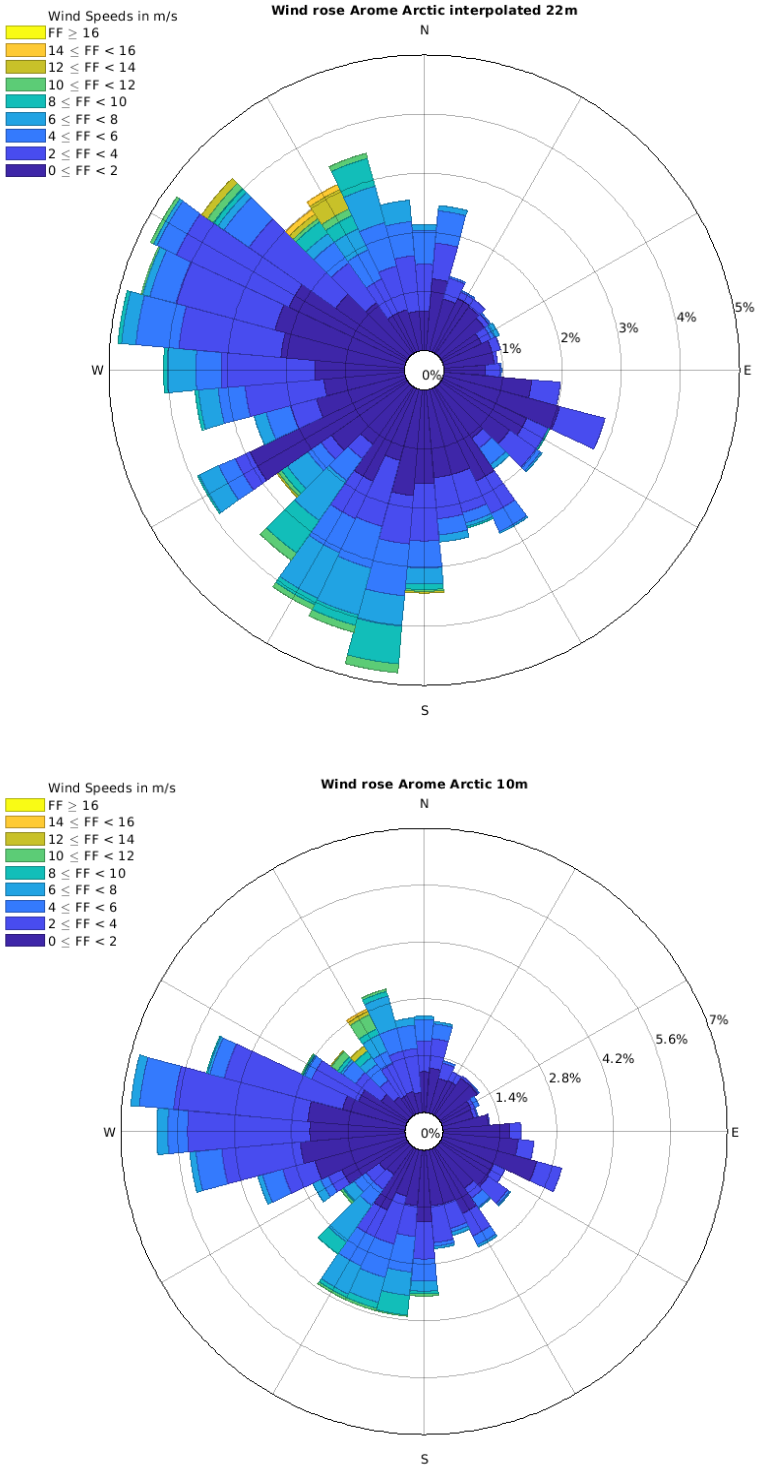

Figure 68: *Wind rose based on wind direction and wind speed from Arome Arctic with the output value at 22 m (upper panel) and at 10 m (lower panel) for the period 1 July to 14 November 2023.*

tion in the model. These differences in wind direction frequency between observation and model are likely caused by the coarse topographic resolution in the 2.5 km model, which does not adequately represent the steep and complex terrain near the observation site (Figures 1 and 5). For example, the mountain range located west of Skjærvika likely blocks westerly winds more effectively than what is represented in the model. Moreover, the model appears to underestimate local effects such as the northeasterly sea breeze frequently observed at this location during summer, along with terrain-induced wind modifications. This is reflected in the underrepresentation of northeasterly winds in the model data shown in Figure 68. In addition, a comparison between model output at different heights shows that the 22 m wind exhibits similar frequencies from the west-northwest and south-southwest, while the 10 m wind shows a noticeably higher frequency from the west-northwest.

Figure 69 presents wind speed from the Arome Arctic model at 22 m and 10 m, evaluated against wind speed observations from the 3D sonic anemometer at 22 m. The modelled wind speed at 22 m shows slightly higher MAE and larger positive BIAS compared to the 10 m model wind. Consistent with the previous period, the general trend indicated by the BIAS is that the model tends to overestimate horizontal wind speeds relative to observations. However, visual inspection of the time series suggests that the model underestimates wind speeds during stronger wind events. When filtering out observed wind speeds below 8 m/s (results not shown), the BIAS and MAE for the 22 m model wind are -0.3 m/s and 1.86 m/s, respectively, while the 10 m model wind yields a BIAS of -0.59 m/s and an MAE of 1.79 m/s.

Figure 70 shows wind gusts from the Arome Arctic model at 22 m and 10 m, evaluated against wind gusts derived from the 3D sonic anemometer, using the method described in Section 3.8. Similar to the previous period, the model generally overestimates wind gusts compared to observations. Since wind gusts are parameterized based on the mean wind speed and are therefore highly correlated with it, errors in the modelled mean wind speed directly influence the accuracy of the modelled gusts. Overestimated gust values are particularly associated with modelled southeasterly winds, where the smoother model topography leads to stronger mean wind speeds than what is observed in reality. This issue is discussed further in Section 5.8 and illustrated in Figures 85 and 88.

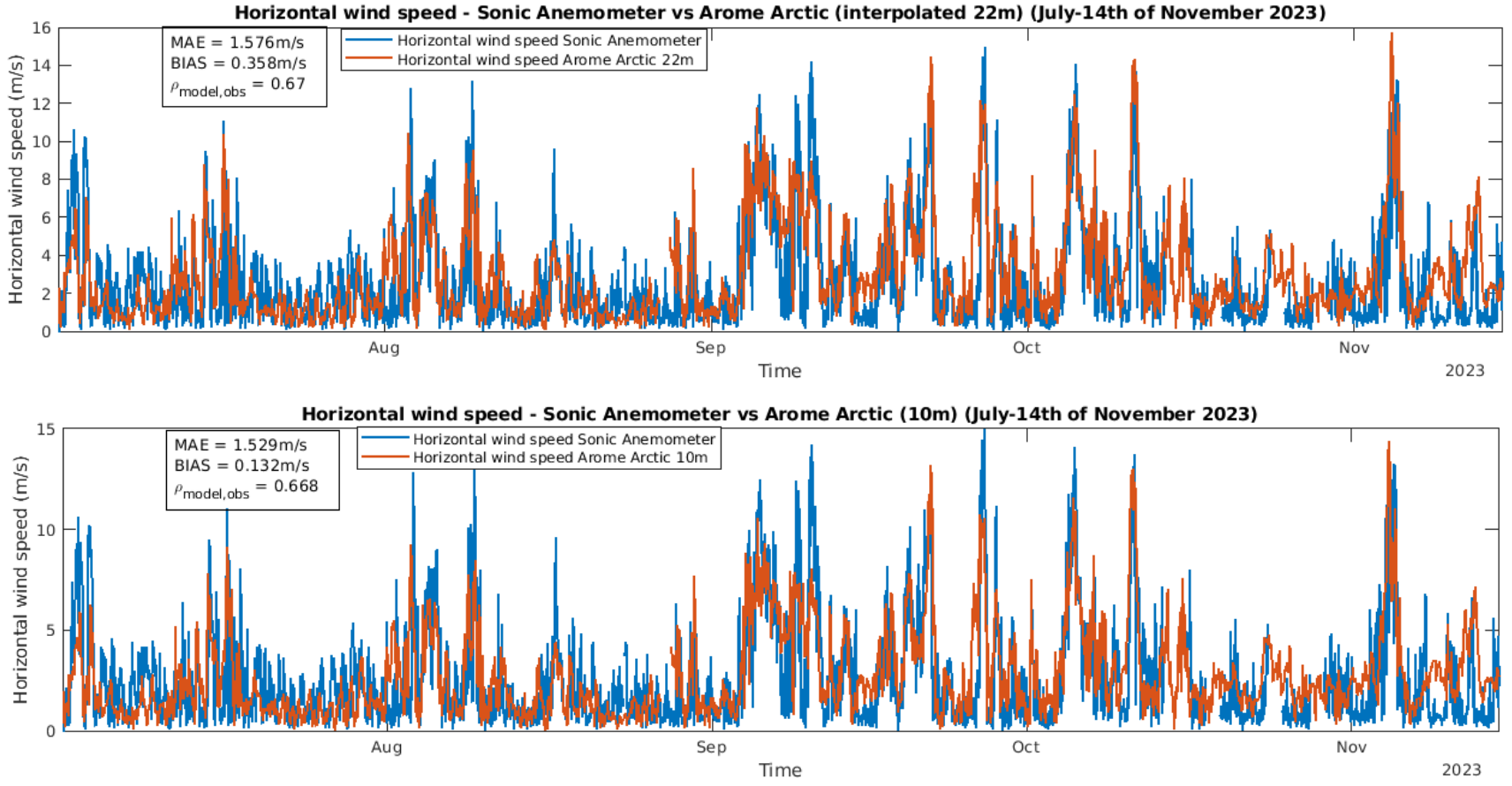

Figure 69: *Horizontal wind speed from Arome Arctic (in red) and observations from the sonic anemometer (in blue), on top with the interpolated value (22 m) and below with the output value at 10 m, for 1 July to 14 November 2023.*

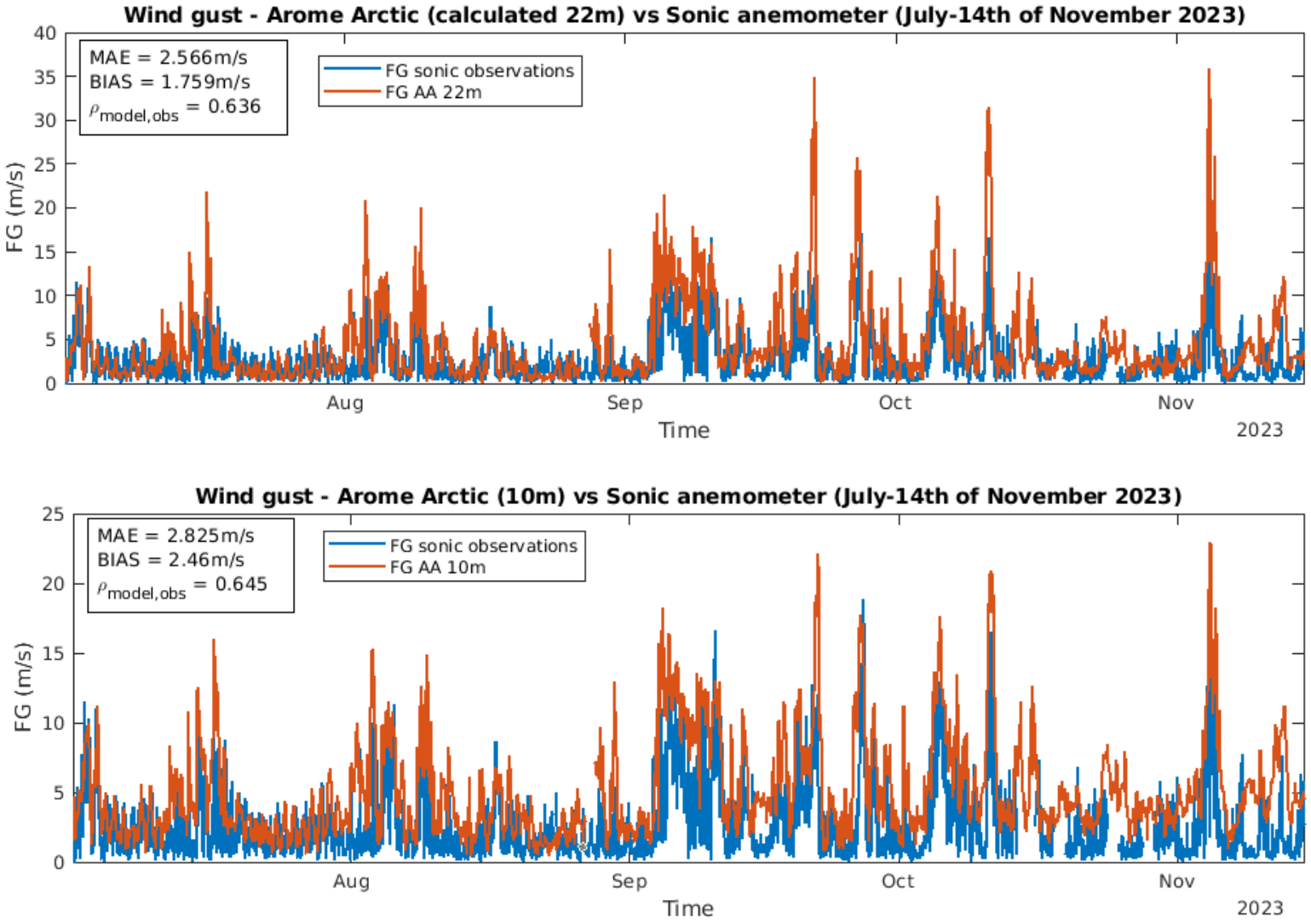

Figure 70: *Wind gust from Arome Arctic (AA, in red) and observations from the sonic anemometer (in blue), on top with the interpolated value (22 m) and below with the output value at 10 m in the period 1 July to 14 November 2023.*

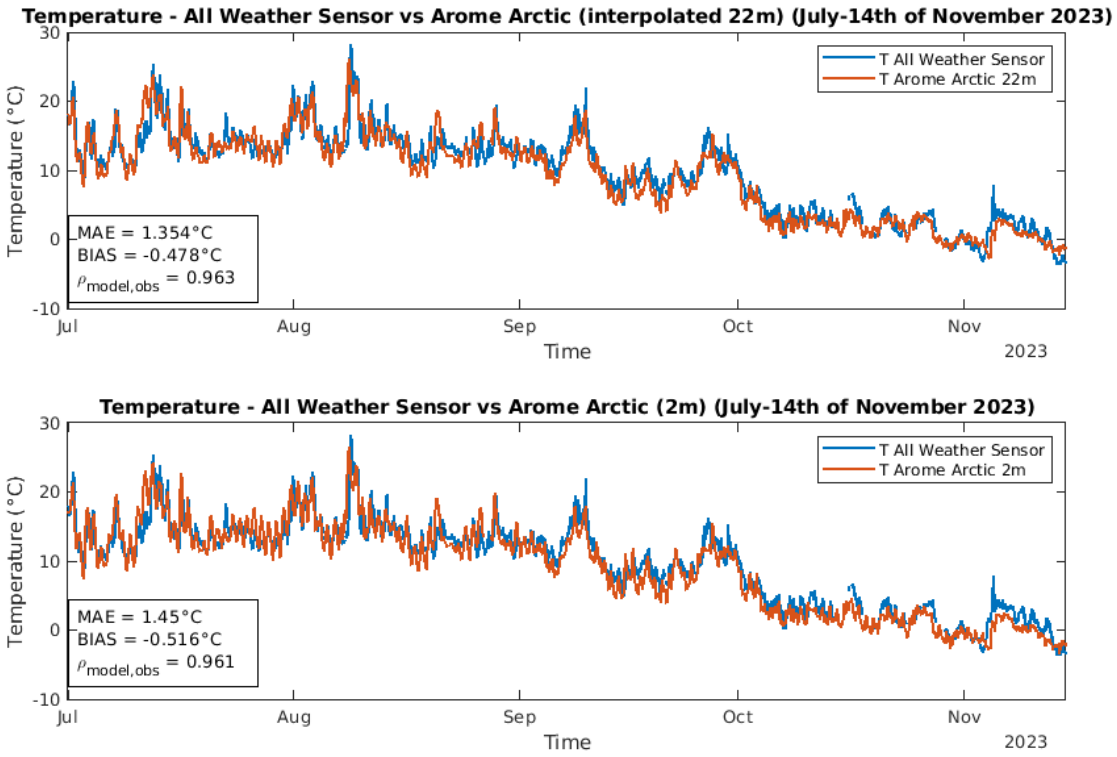

Figure 71: *Temperature from Arome Arctic (in red) and observations from the AWS (in blue), on top with the interpolated value (22 m) and below with the output value at 2 m in the period 1 July to 14 November 2023.*

5.7.2 Temperature

Figure 71 presents temperature data from the Arome Arctic model at 22 m and 2 m heights, evaluated against temperature observations from the AWS. The results indicate that the model exhibits an average negative BIAS of $-0.5°C$ during the time period under consideration. The BIAS values at 22 m and 2 m differ slightly but remain relatively close in magnitude. Despite this systematic underestimation, the model shows a high correlation coefficient of 0.96, indicating that it captures the temporal variability in observed temperature well.

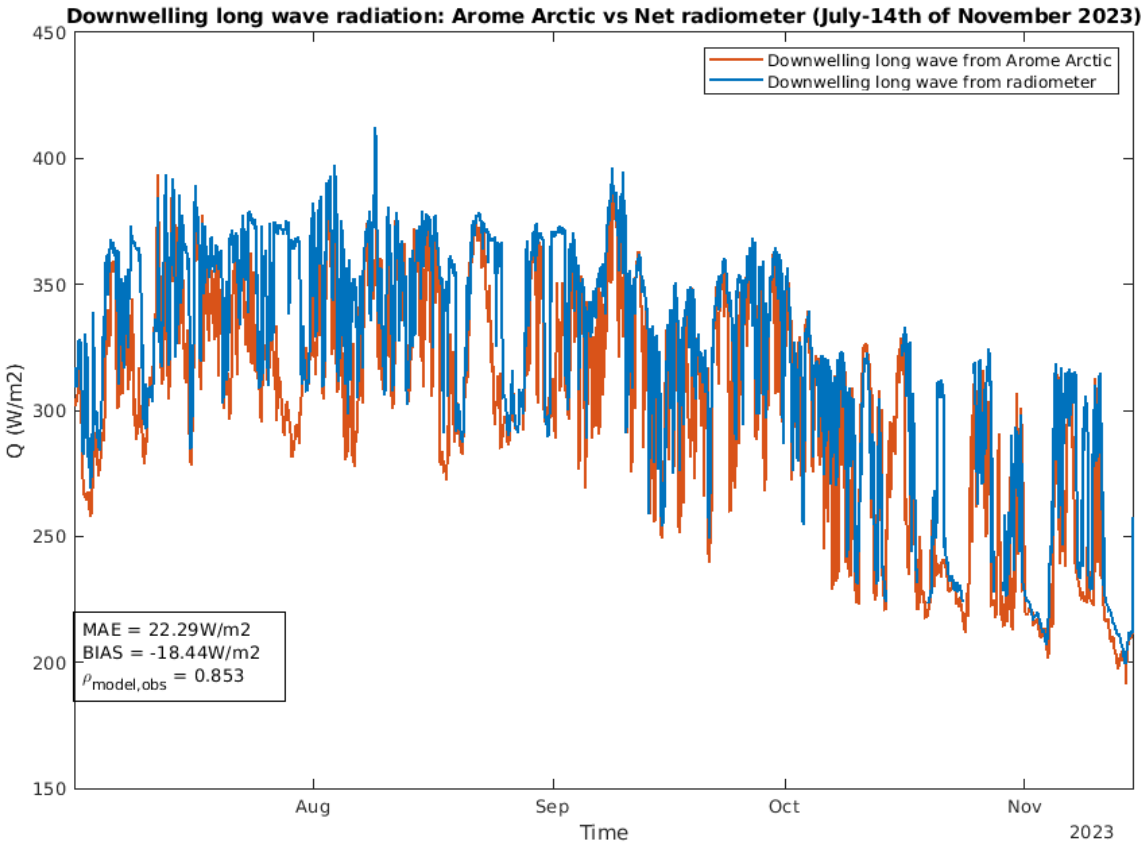

Figure 72: *Incoming longwave radiation from Arome Arctic (in red) and observations from the net radiometer (in blue).*

5.7.3 Incoming longwave radiation

Figure 72 displays the incoming longwave radiation from the Arome Arctic model alongside measurements from the net radiometer. Consistent with the previous period, the model generally underestimates the incoming longwave radiation compared to observations. As noted earlier, this discrepancy may result from the model underestimating temperature or inaccuracies in cloud cover representation. During the earlier period, the model underestimated temperature by 0.8°C (Figure 35), whereas in the current period under consideration, the negative temperature BIAS is reduced to 0.5°C (Figure 71). Despite this smaller negative temperature BIAS, the model exhibits a larger negative BIAS for incoming longwave radiation in the later period (Figures 36 and 72). This suggests that factors other than temperature BIAS, such as insufficient cloud cover or other model limitations, likely contribute more significantly to the underestimation of longwave radiation.

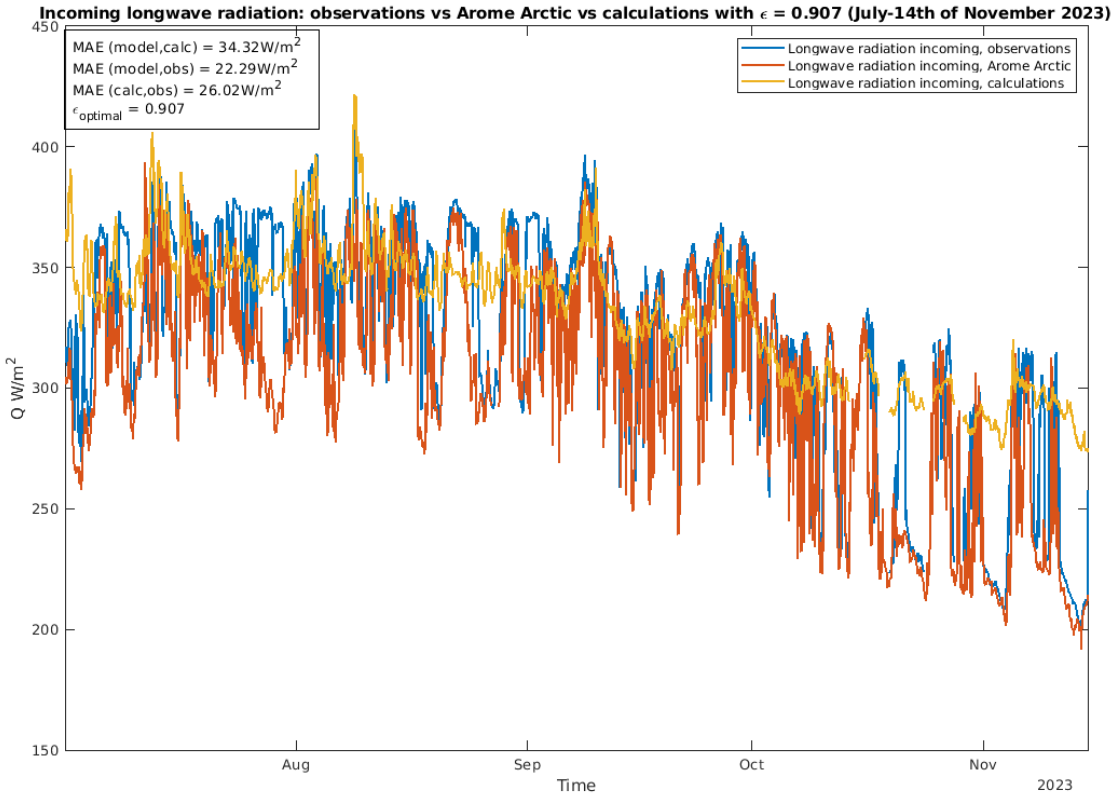

Figure 73: *Incoming longwave radiation; observed (in blue), calculated (in yellow), and from Arome Arctic (in red). MAE and BIAS between these are included, as well as the optimal emissivity, $\varepsilon_{optimal}$, used for the calculations.*

Figure 73 shows the calculated, observed, and modelled incoming longwave radiation. The calculated longwave radiation follows the methodology described in Section 3.6. The optimal emissivity for this period that provided the smallest MAE between the calculated and the observed radiation is found to be $\varepsilon_{\text{optimal}} = 0.907$.

Similar to the earlier period, sub-freezing temperature events during this period are further analyzed to determine the optimal emissivity for temperatures below 0°C (Figure 74). As shown in the figure, the optimal emissivity value determined by minimizing the MAE is $\varepsilon_{\text{optimal}} = 0.697$, which is close to the value of 0.735 found in the earlier period (Section 4.9.5, Figure 38). The mean emissivity for both periods combined is 0.72, considerably lower than that for the general period and more consistent with the value of 0.7 applied in MINCOG. The BIAS between modelled and observed longwave radiation is -8.16 W m^{-2}, indicating that the model tends to underestimate incoming longwave radiation. The BIAS between calculated and observed longwave radiation is -7.72 W m^{-2},

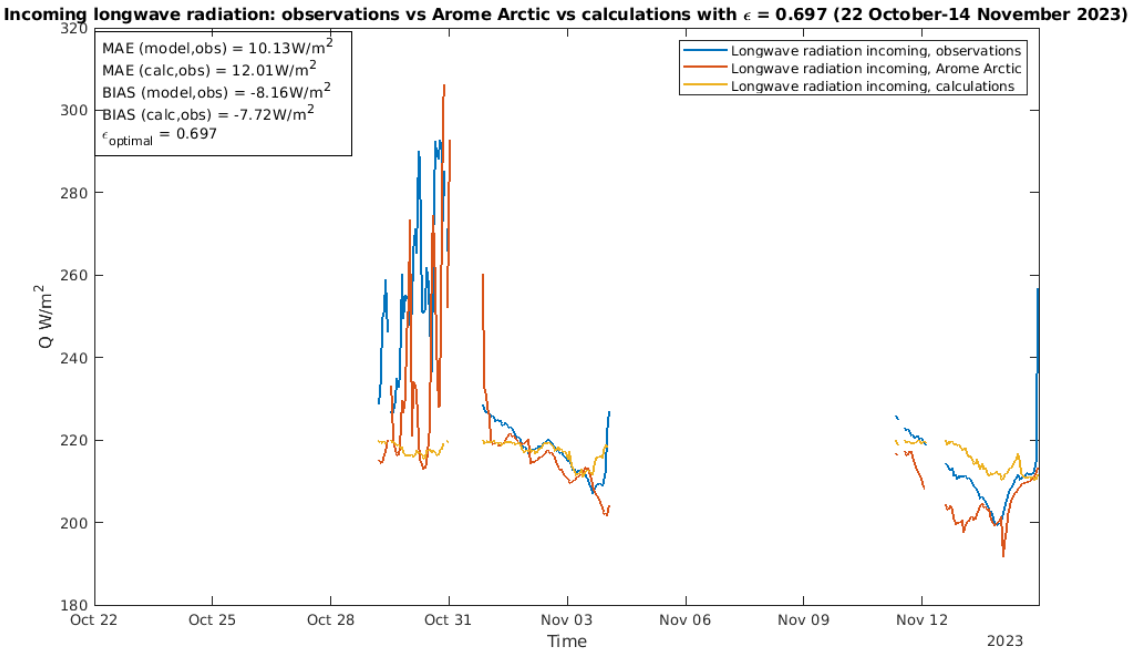

Figure 74: *Incoming longwave radiation; observed (in blue), calculated (in yellow), and from Arome Arctic (in red) when the temperature is below 0°C in the period 1 July to 14 November 2023. MAE and BIAS between these are included, as well as the optimal emissivity, $\varepsilon_{optimal}$, used for the calculations.*

demonstrating that the calculated LW_{in} for this period aligns more closely with observations compared to the earlier period (Figure 38).

5.7.4 Incoming shortwave radiation

Figure 75 shows the incoming shortwave radiation from Arome Arctic verified against the incoming shortwave radiation from the net radiometer. Similar to the earlier period, the positive BIAS indicate that the model predicts higher values of shortwave radiation than what is recorded by the net radiometer. As already discussed for the previous period, the underestimation in SW may be due to underestimation of low clouds or the missing shadow effect from nearby mountains in the model. Most likely it may be a combination of both factors.

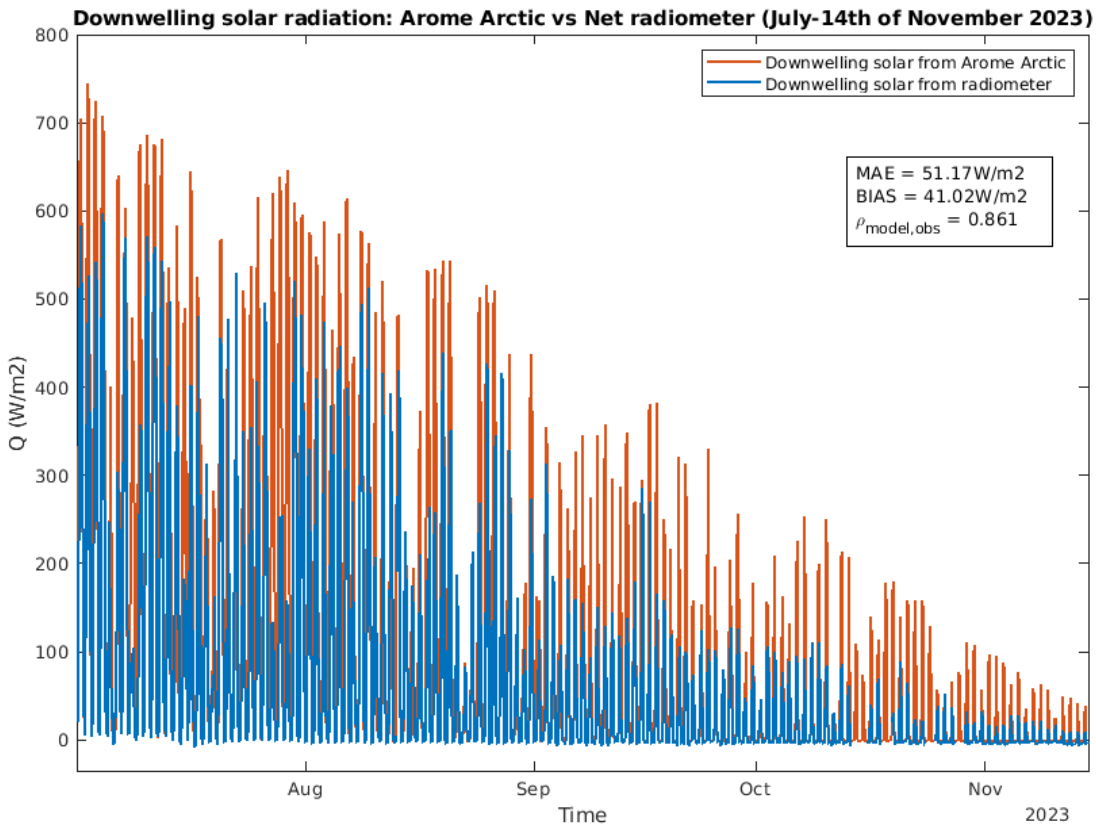

Figure 75: *Incoming shortwave radiation from Arome Arctic (in red) and observations from the net radiometer (in blue), 1 July to 14 November 2023.*

5.7.5 Precipitation

Figures 76 and 77 present the hourly and 24-hour accumulated precipitation, respectively. As observed in the figures and consistent with the earlier period, the 24-hour accumulated precipitation exhibits a stronger correlation with observations than the hourly accumulated precipitation. This difference is likely attributable to the lower predictability of short-term (hourly) precipitation fluctuations compared to daily totals. Throughout this period, the model generally shows a slight tendency to overestimate precipitation based on the BIAS values. Specifically, 24-hour accumulated precipitation is predominantly overestimated. However, two notable exceptions occur at the beginning and end of September, where the AWS records significantly higher 24-hour precipitation totals than the model. These instances highlight that during certain high-precipitation events, the model may underestimate 24-hour totals. Conversely, several cases of underestimation are also evident.

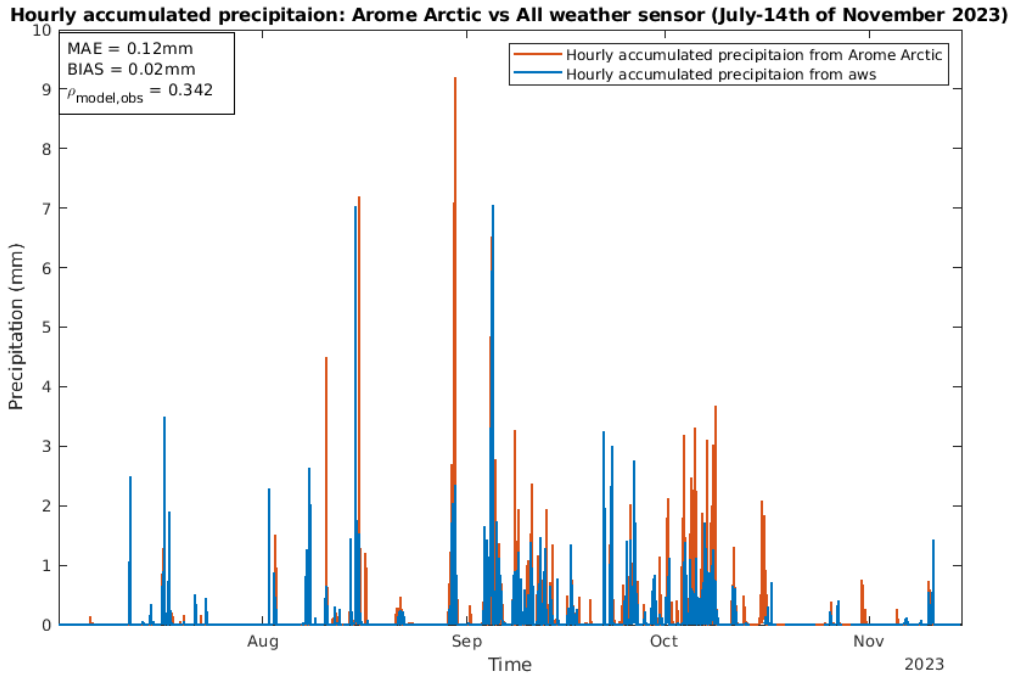

Figure 76: *Hourly accumulated precipitation from Arome Arctic (in red) and observations from the AWS (in blue), 1 July to 14 November 2023.*

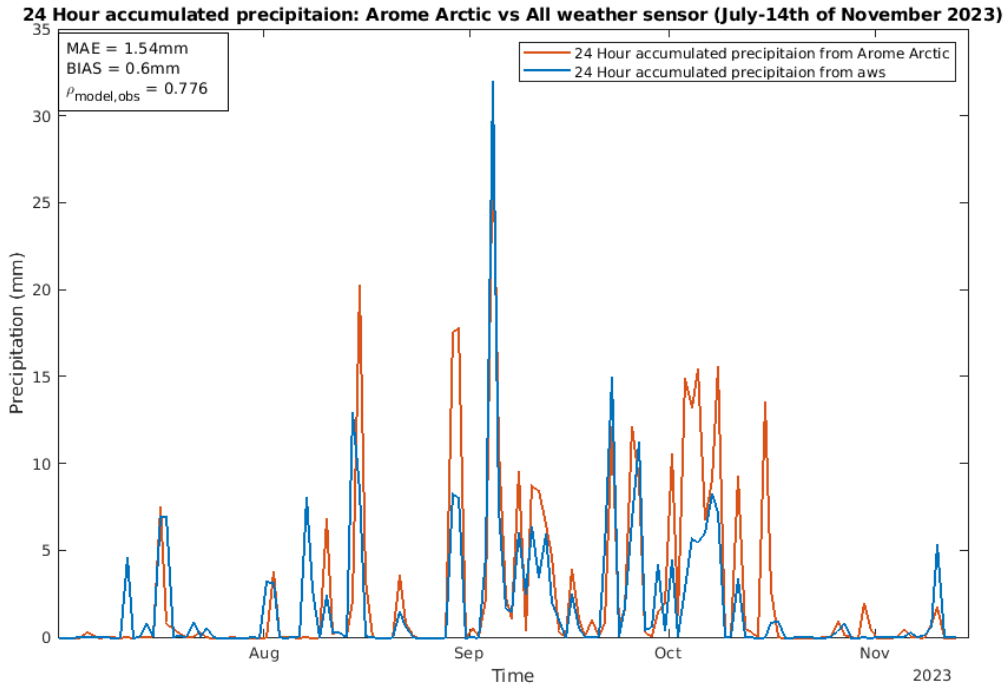

Figure 77: *24-hour accumulated precipitation from Arome Arctic (in red) and observations from the AWS (in blue), 1 July to 14 November 2023.*

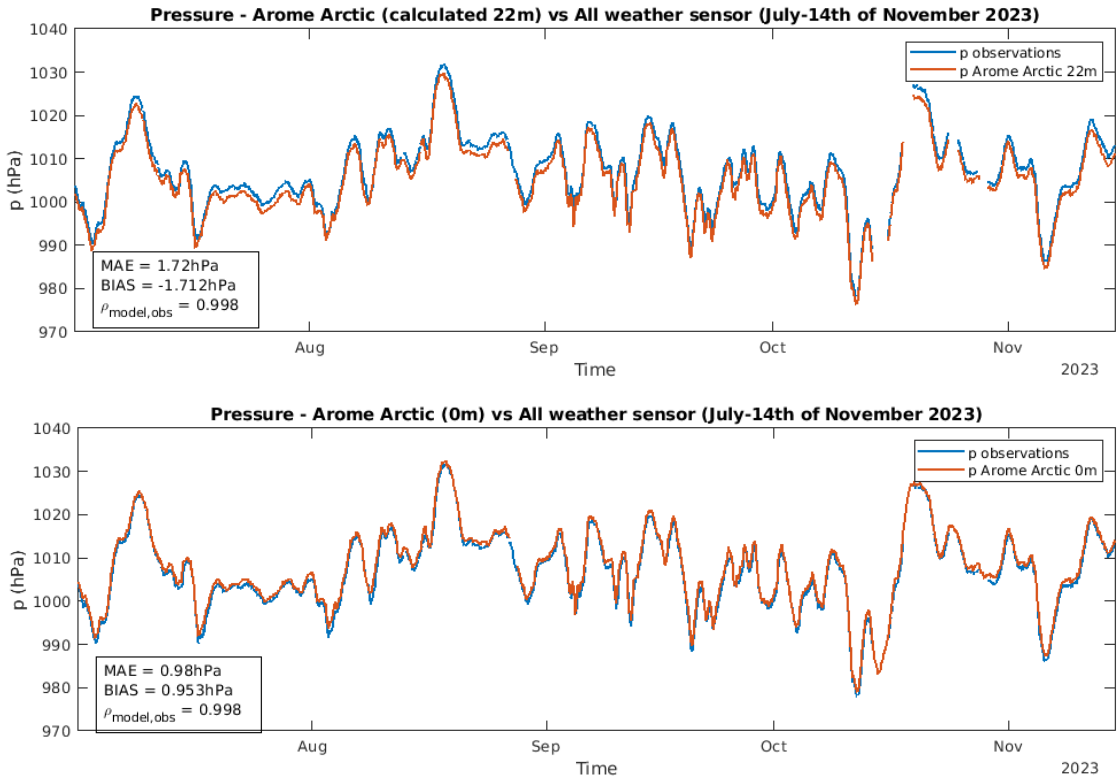

Figure 78: *Pressure from Arome Arctic (in red) at 22 m (above) and at 0 m (below), in conjcuntion with the observed pressure at 22 m (in blue), in the period 1 July to 14 November 2023.*

5.7.6 Pressure

Figure 78 shows pressure from Arome Arctic at 22 m and at surface level (0 m), verified against pressure measurements from the AWS. The low BIAS and MAE, combined with a high correlation coefficient of 0.998, indicates that the model produces relatively accurate pressure compared to the observed values. However, similar to the earlier period, the use of mean sea level pressure (MSLP) from the model results in a positive BIAS of approximately 1 hPa, whereas the interpolated pressure at 22 m height produces a negative BIAS of about -1.7 hPa. The total pressure difference of around 2.7 hPa between the surface and 22 m aligns with an approximate decrease of 1 hPa per 8 m elevation, which corresponds to the typical pressure reduction in a standard reference atmosphere. This suggests that the model generally underestimates pressure at this location, with a consistent negative BIAS observed across both periods.

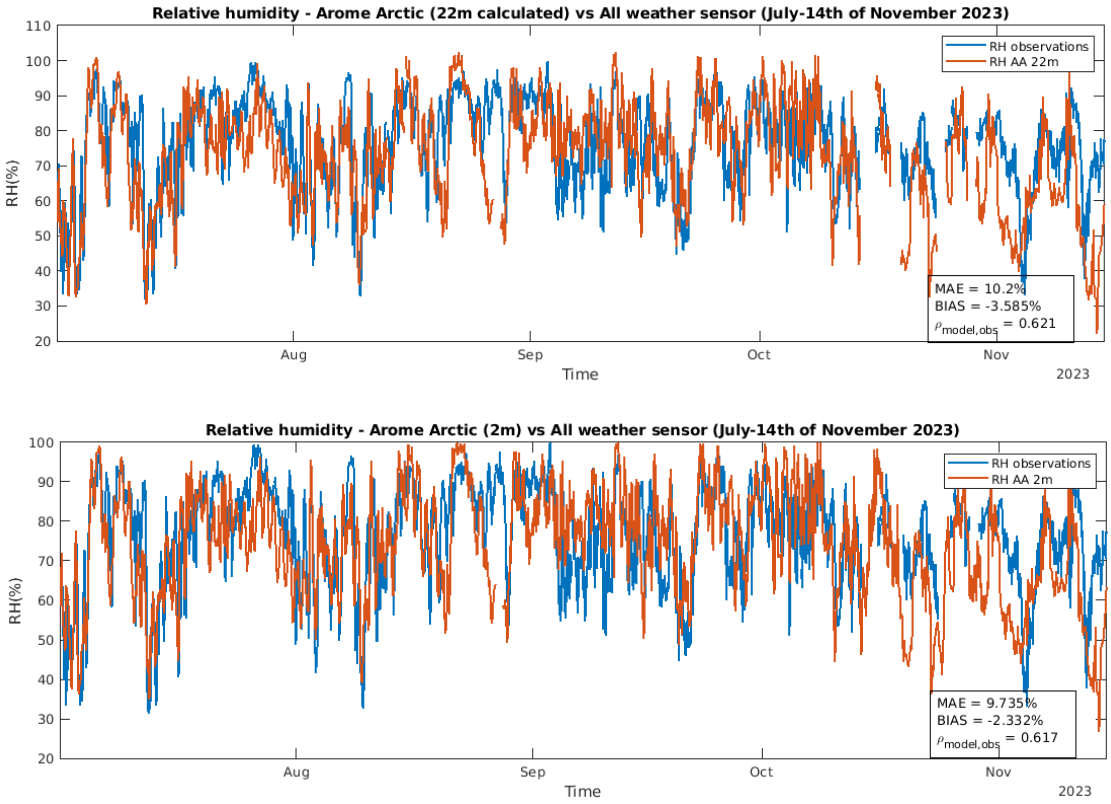

Figure 79: *Relative humidity from Arome Arctic (AA, in red) and observations from the AWS (in blue). In the top panel with the output value at 22 m and the lower panel with the calculated value at 2 m for 1 July to 14 November 2023.*

5.7.7 Relative humidity

Figure 79 presents relative humidity from Arome Arctic at 22 m and 2 m heights, evaluated against relative humidity measured by the AWS at 22 m. During this period, the BIAS indicates a general underestimation of relative humidity by the model, in contrast to the earlier period where a positive BIAS was observed (Figure 43). The earlier overestimation was suggested to be linked to a negative temperature BIAS. However, since the temperature BIAS remains negative in the current period, this may not explain the observed underestimation in relative humidity. One possible explanation is an underestimation of the sea breeze within the model, as indicated by wind rose data in Figure 68 and the lower panel of Figure 63.

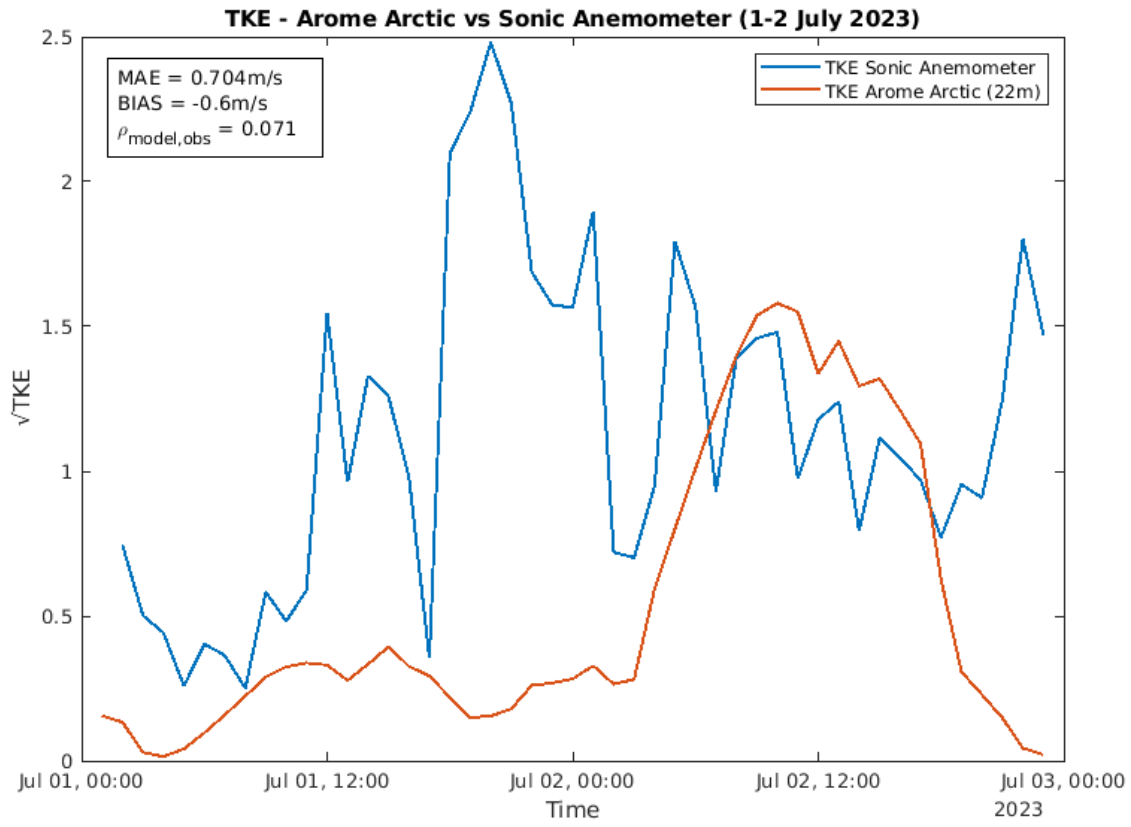

Figure 80: *$\sqrt{TKE}$ from Arome Arctic (in red) and observations from the 3D sonic anemometer (in blue) for 1 and 2 July 2023.*

5.8 Model verification of offshore flow case studies

This section provides model verification of the case studies discussed in sections 5.3 and 5.5 by looking at the modelled $\sqrt{\text{TKE}}$, wind direction, and the wind speed compared to the observations.

5.8.1 Offshore flow case: 1 and 2 July 2023

Figure 80 presents $\sqrt{\text{TKE}}$ from Arome Arctic interpolated to 22 m, verified against $\sqrt{\text{TKE}}$ calculated from the 3D sonic anemometer, along with corresponding values of MAE, BIAS, and the Pearson correlation coefficient for 1 and 2 July 2023. In this case, earlier sections discuss whether $\sqrt{\text{TKE}}$ is influenced by potential mountain wave activity before midnight between 1 and 2 July, and that the reduction in activity after midnight likely results from a change in wind direction toward the north (Figures 59 and 64).

In order to further assess the weather conditions during this period, the observed wind

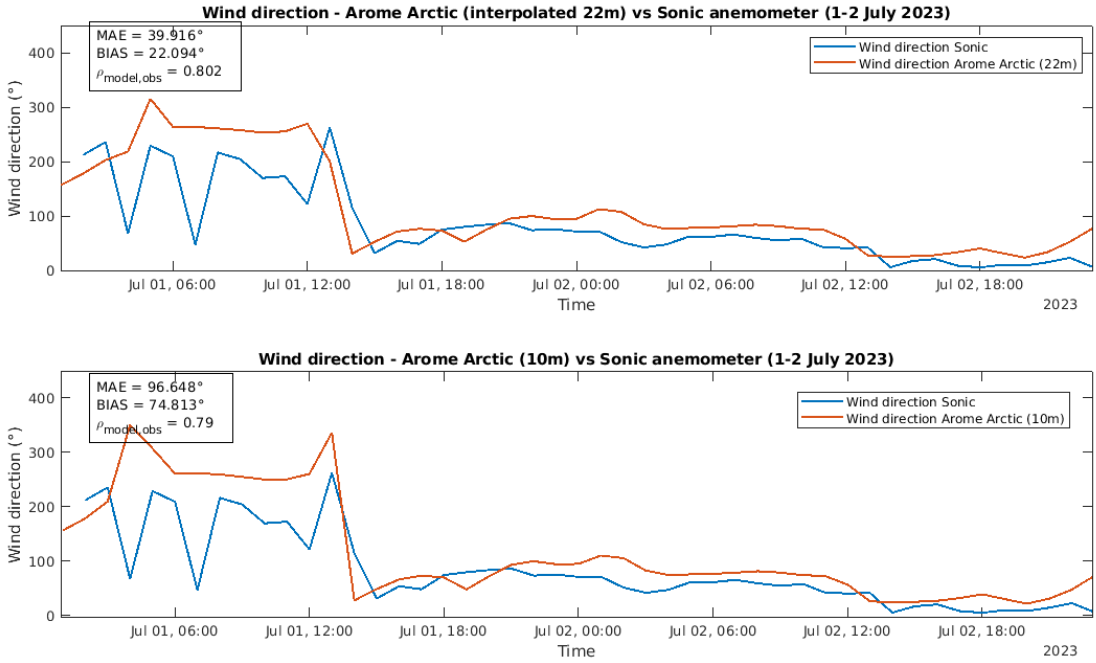

Figure 81: *Wind directions from Arome Arctic (in red) and observations from the 3D sonic anemometer (in blue) for 1 and 2 July 2023. In the upper panel for 22 m, and in the lower panel for 10 m.*

direction, wind speed, and wind gust are compared with Arome Arctic output at 22 m and 10 m (Figures 81, 82 and 83). In general, there is a relatively strong correlation between modelled and observed wind direction. Similarly, modelled horizontal wind speed shows strong agreement with the observations, although during offshore flow, the predicted winds are occasionally weaker than the observed values. In contrast, for the wind gust shown in Figure 83, the model predicts stronger gusts at 22 m than at 10 m before midnight. However, gusts at 10 m correspond more closely with the observed values than those predicted at 22 m.

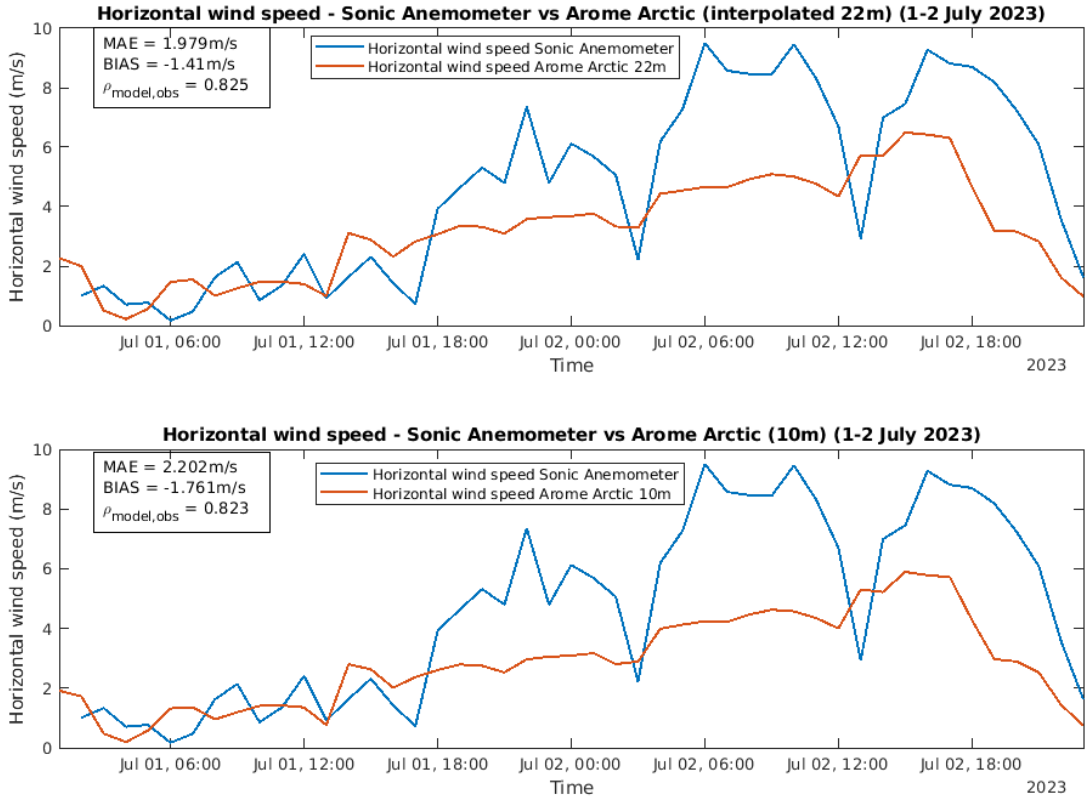

Figure 82: *Wind speed from Arome Arctic (in red) and observations from the 3D sonic anemometer (in blue) for 1 and 2 July 2023. In the upper panel for 22 m, and in the lower panel for 10 m.*

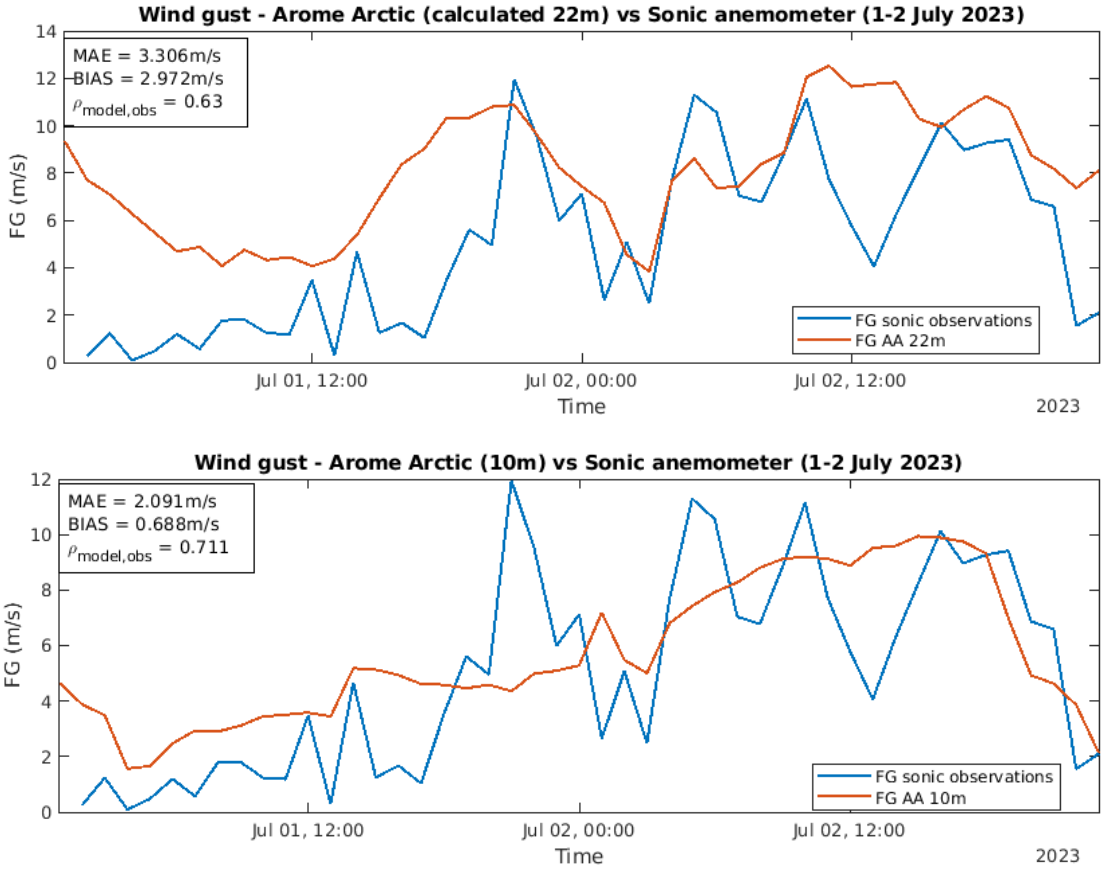

Figure 83: *Wind gust from Arome Arctic (in red) and observations from the 3D sonic anemometer (in blue) for 1 and 2 July 2023. In the upper panel for 22 m, and in the lower panel for 10 m.*

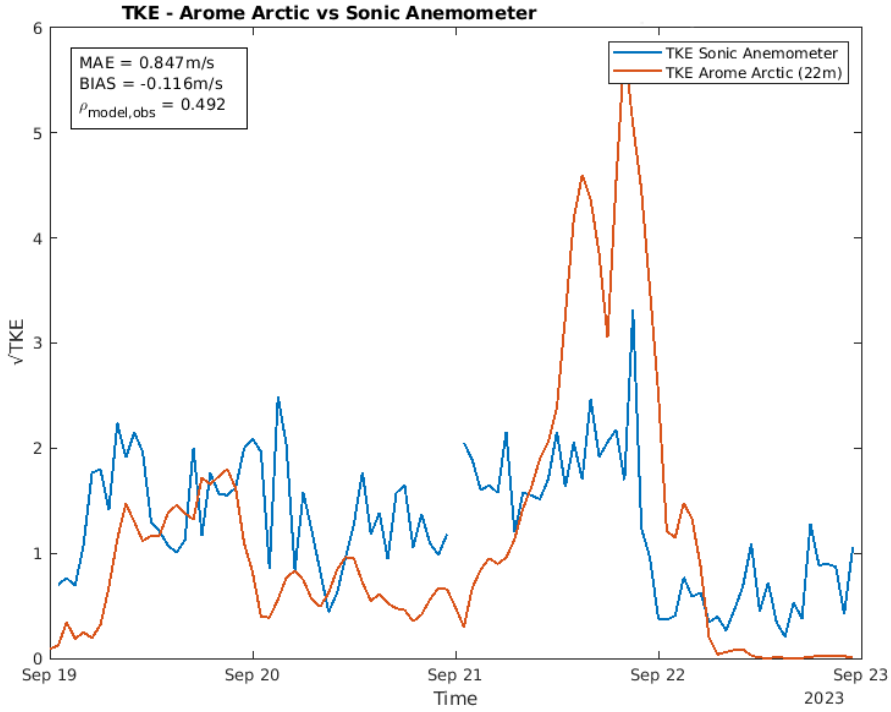

Figure 84: *$\sqrt{TKE}$ from Arome Arctic (in red) and observations from the sonic anemometer (in blue) in the period 19 to 22 September 2023.*

5.8.2 Offshore flow case: 19 to 22 September 2023

Figure 84 presents $\sqrt{\text{TKE}}$ from Arome Arctic at 22 m, verified against $\sqrt{\text{TKE}}$ calculated from measurements by the 3D sonic anemometer during offshore flow from 19 through 22 September 2023. A prolonged and relatively steady offshore flow is observed from early 19 September to late 21 September, coinciding with a clear increase in $\sqrt{\text{TKE}}$ during the same period (see Figures 60 and 65). As shown in Figure 84, the model predicts higher $\sqrt{\text{TKE}}$ values than those measured by the 3D sonic anemometer between 21 and 22 September. However, for the remainder of the period, modelled turbulence levels are generally lower than observed values, resulting in an overall negative BIAS in $\sqrt{\text{TKE}}$ of approximately -0.12 m/s.

Figures 85 and 86 illustrate the observed wind direction and wind speed together with Arome Arctic output at 22 m and 10 m for the same period. As shown in Figure 85, the modelled wind direction tends to originate more from the southeast, while the observations indicate winds primarily from the east and northeast. Nevertheless, both the wind speed in Figure 86 and the $\sqrt{\text{TKE}}$ in Figure 84 indicate the presence of strong winds and turbulent conditions during offshore flow in both the model and the observations.

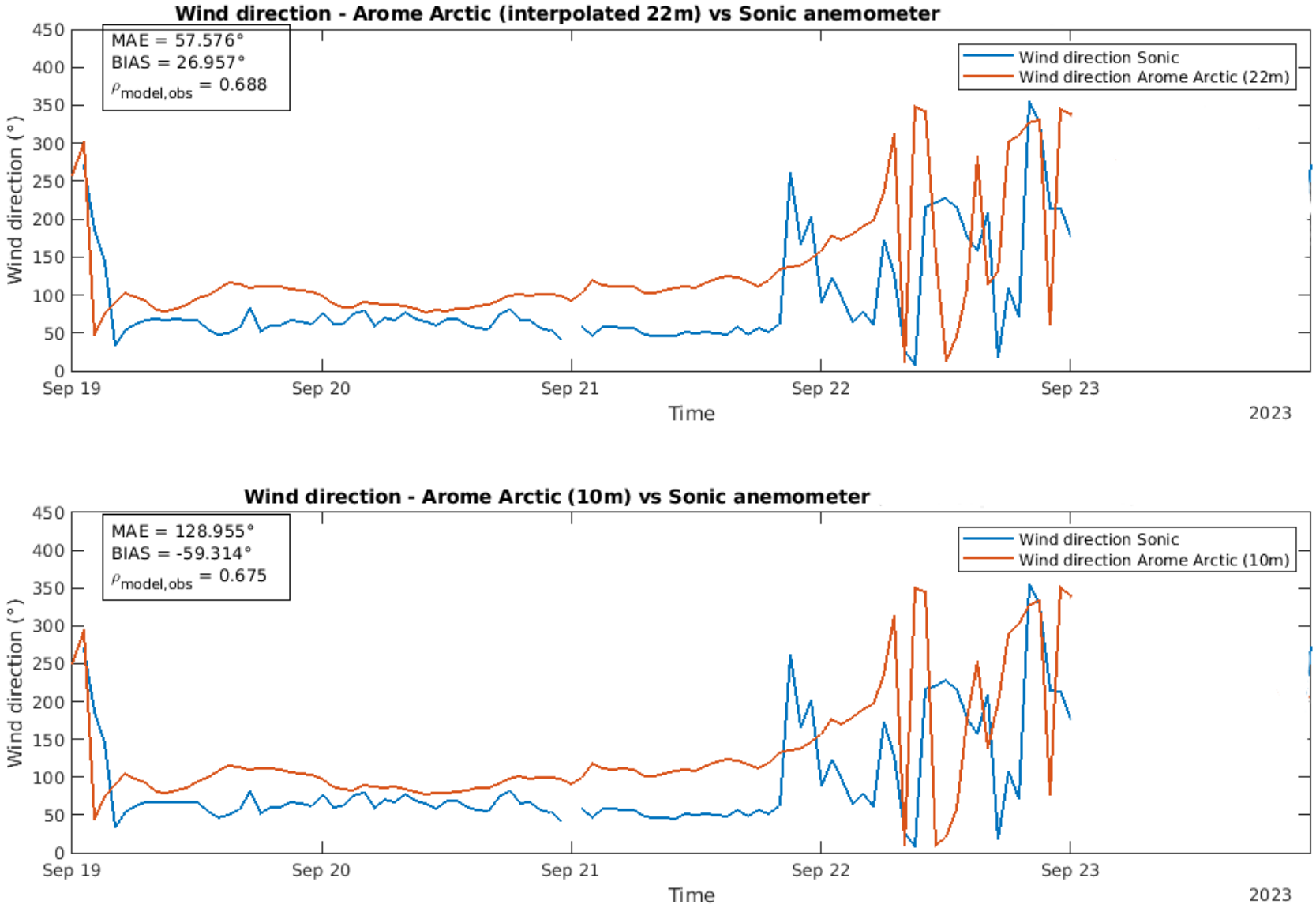

Figure 85: *Wind directions from Arome Arctic (in red) and observations from the 3D sonic anemometer (in blue) in the period 19 to 22 September 2023. In the upper panel for 22 m, and in the lower panel for 10 m.*

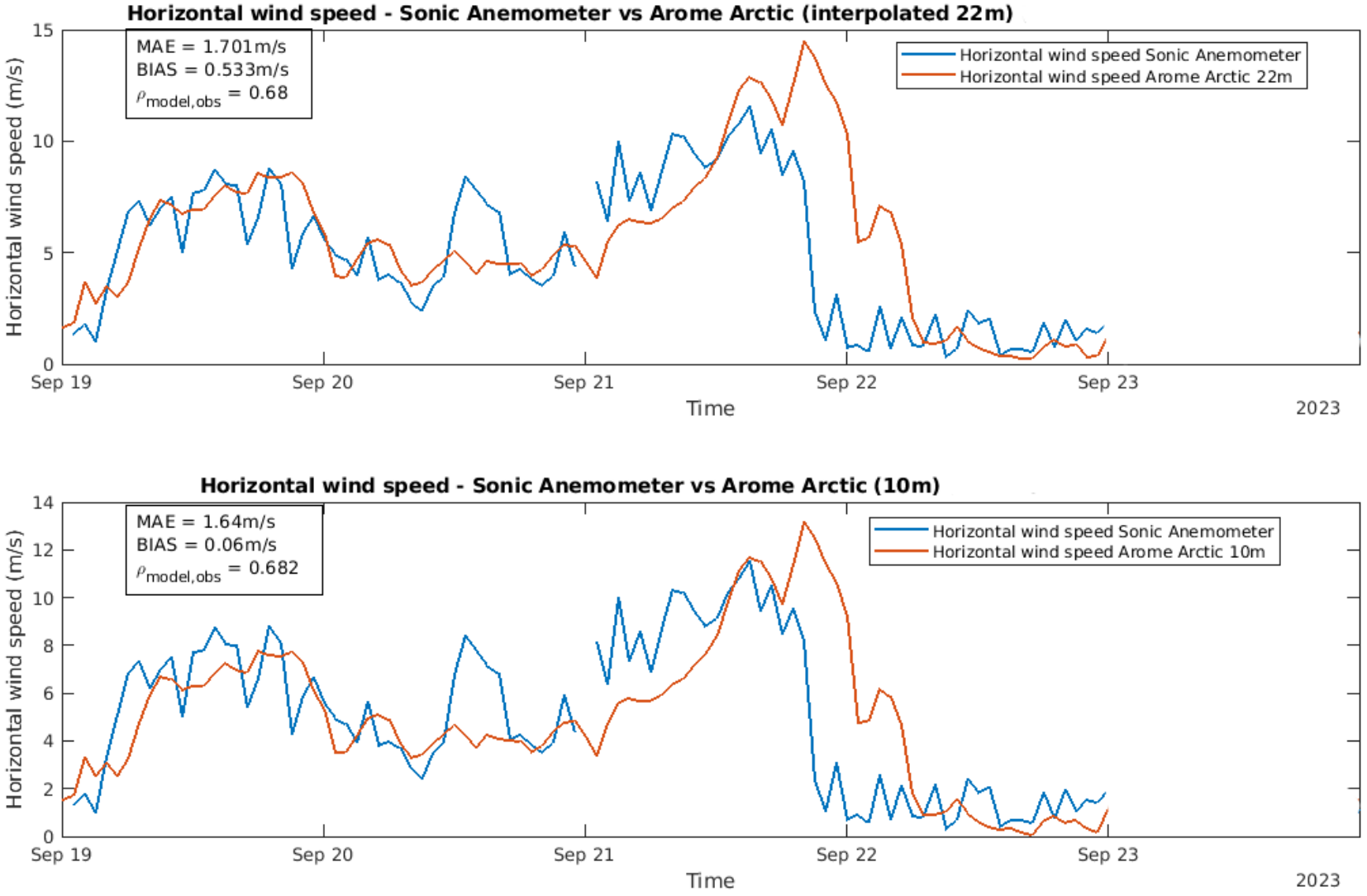

Figure 86: *Wind speed from Arome Arctic (in red) and observations from the 3D sonic anemometer (in blue) in the period 19 to 22 September 2023. In the upper panel for 22 m, and in the lower panel for 10 m.*

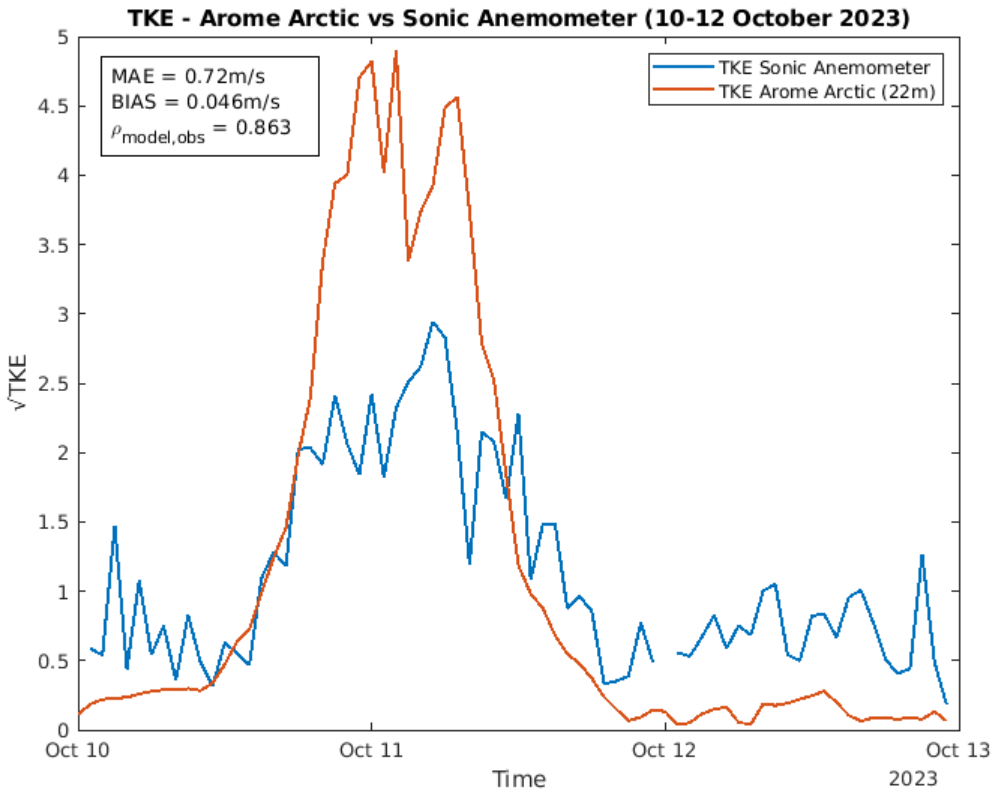

Figure 87: *$\sqrt{TKE}$ from Arome Arctic (in red) and observations from the sonic anemometer (in blue) in the period 10-12 October 2023.*

5.8.3 Offshore flow case: 10 to 12 October 2023

Figure 87 shows $\sqrt{\text{TKE}}$ from Arome Arctic at 22 m alongside $\sqrt{\text{TKE}}$ derived from the 3D sonic anemometer at the same height for the period between 10 and 12 October 2023. As in the previously discussed case from September (Section 5.8.2), the model predicts relatively elevated $\sqrt{\text{TKE}}$ values compared to those calculated from observations during offshore flow.

Figures 88 and 89 compare the observed wind direction and wind speed with Arome Arctic output at 22 m and 10 m for the same case. As shown in Figure 88, the modelled wind direction tends more toward the southeast than what is recorded by the sensor. This difference is most likely related to the spatial resolution of the model, which does not adequately represent the surrounding terrain. The model underestimates the height of the mountain west of the site, which may result in stronger flow from the southeast, while the observed winds are somewhat weaker and originate from the northeast to east. Although

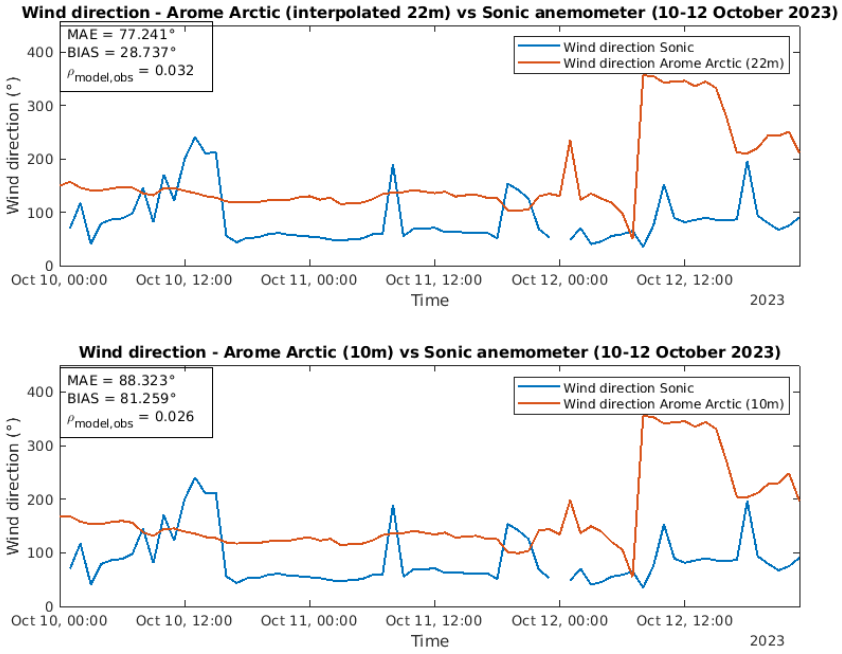

Figure 88: *Wind directions from Arome Arctic (in red) and observations from the sonic anemometer (in blue) in the period 10-12 October 2023. In the upper panel for 22 m, and in the lower panel for 10 m.*

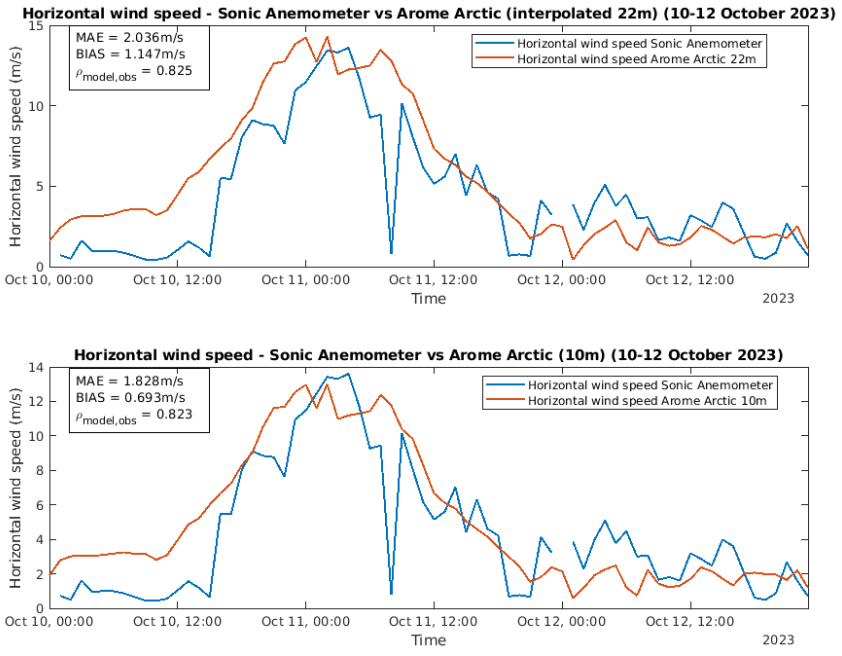

Figure 89: *Wind speed from Arome Arctic (in red) and observations from the sonic anemometer (in blue) in the period 10-12 October 2023. In the upper panel for 22 m, and in the lower panel for 10 m.*

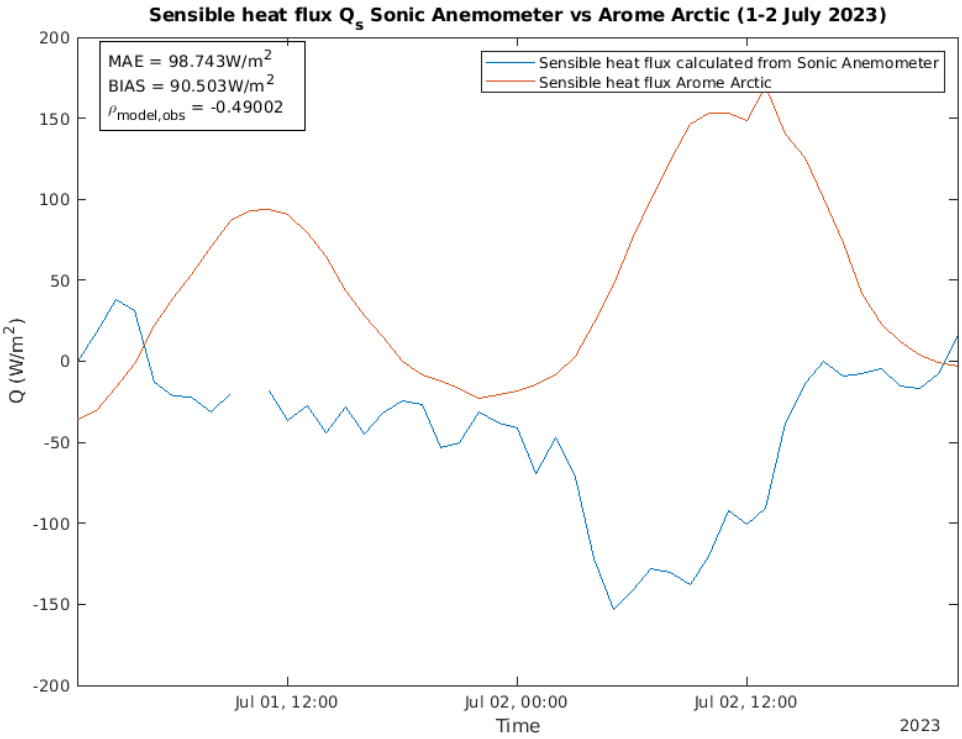

Figure 90: *Sensible heat flux from Arome Arctic (in red) and observations from the sonic anemometer (in blue) in the period 1 to 2 July 2023.*

both $\sqrt{\text{TKE}}$ and wind speed are overestimated in the model, the observations still indicate periods of turbulent conditions and strong winds, even though the wind direction remains more northeasterly to easterly than predicted, which is more southeasterly in the model (Figures 87 and 89).

All three cases indicate that the model and the observations share, to some extent, similar turbulent weather conditions during offshore flow. These results, together with the consistent findings from the earlier period (15 March to 30 June 2023) discussed in Section 4.10, provide strong support for the conclusion that vertical wind velocities and the corresponding $\sqrt{\text{TKE}}$ values tend to be more reliable during offshore flow compared to conditions dominated by southwesterly flow.

5.8.4 Sensible heat flux analysis for the three offshore flow cases

Figures 90, 91, and 92 show the sensible heat flux derived from the 3D sonic anemometer, along with the corresponding values from Arome Arctic, for the three previously discussed offshore flow cases. Similar to the two offshore flow cases from the earlier

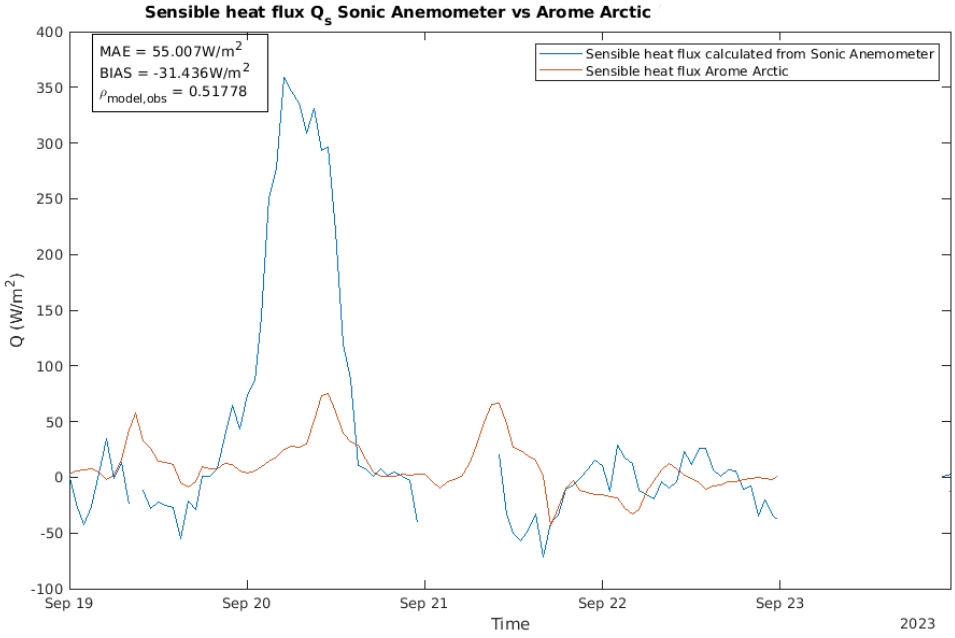

Figure 91: *Sensible heat flux from Arome Arctic (in red) and observations from the sonic anemometer (in blue) in the period 19-22 September 2023.*

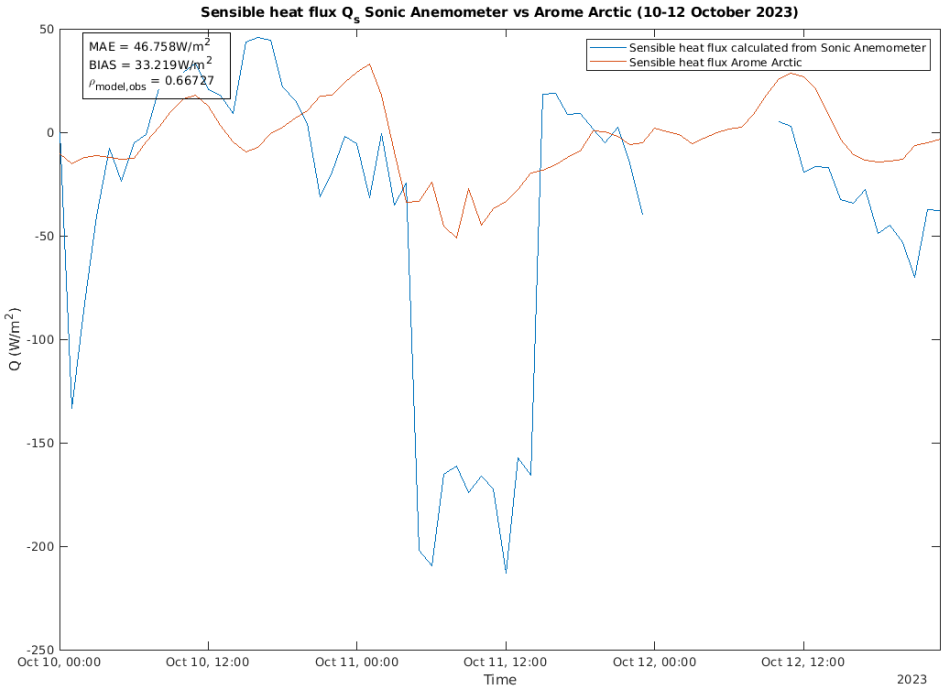

Figure 92: *Sensible heat flux from Arome Arctic (in red) and observations from the sonic anemometer (in blue) in the period 10-12 October 2023.*

period described in Section 4.10.3, the model does not reproduce the relatively strong negative and positive observed values. In the July case, the model predicts a clearly too high positive value, whereas the observations indicate negative sensible heat flux. For the September case, the model captures the correct sign of the flux; however, the observed positive peak of up to 350 W m^{-2} is substantially underestimated. In the October case, the large negative peak approaching -200 W m^{-2} in the observations is represented by only about -50 W m^{-2} in the model.

6 Conclusions

This report provides a comprehensive analysis of data collected at the fish-farm weather station located in Skjærvika, Gratangen, in comparison with model data from two periods: 15 March to 30 June 2023, and 1 July to 14 November 2023. Measurements from the All-weather sensor (AWS), including temperature, humidity, wind speed, atmospheric pressure, and precipitation, appear to be generally reliable throughout the periods considered. For instance, a strong correlation is found between the AWS temperature readings and the dry temperature derived from the sonic temperature measured by the 3D sonic anemometer and the relative humidity from the AWS. Wind speed measurements from the two instruments also show good agreement, with a correlation coefficient exceeding 0.92 in both periods. A tendency is observed where the AWS records higher wind speeds during the strongest wind events, whereas the 3D sonic anemometer shows slightly higher wind speeds on average. However, the differences between the instruments are minor overall.

Regarding precipitation, further analysis is required to assess the reliability of the measurements. This includes evaluating the precipitation amount and type using Doppler radar technology from the AWS, before drawing definitive conclusions about the quality of the observed precipitation. In particular, concerns may arise with snow measurements, as discussed by Gay (2016). Interestingly, although the operational Arome Arctic model shows an overall positive BIAS of approximately 0.6 mm for 24-hour accumulated precipitation across both periods, it underestimates the two most extreme precipitation events where more than 30 mm in 24 hours was recorded by the AWS.

For wind direction, the AWS data are affected by magnetic declination and interference from metal structures on the barge, reducing their reliability. Therefore, wind direction measurements from the 3D sonic anemometer are used instead. This under-

lines the importance of avoiding wind sensors with built-in compasses in environments with significant metallic interference, where magnetic disturbances may compromise data accuracy.

The horizontal wind direction and speed recorded by the 3D sonic anemometer appear reliable across various weather conditions. In contrast, the vertical wind component cannot be considered trustworthy during southwesterly flow, as disturbances caused by the feeding barge result in artificially elevated vertical velocities. Consequently, turbulent kinetic energy (TKE) and sensible heat flux, both dependent on vertical velocity, are generally unreliable under these conditions. However, during offshore flow, the vertical wind measurements appear unaffected by the barge, suggesting that both TKE and sensible heat flux derived from the 3D sonic anemometer may be considered valid for such cases. Offshore flow case studies indicate that limitations in horizontal resolution and in the spatial representation of land and sea tiles, particularly the influence of surrounding grid cells, negatively affect the simulation accuracy of turbulent kinetic energy and sensible heat flux. These findings underline the need for caution when interpreting model output in areas with complex topography and heterogeneous surface characteristics, where even small errors in wind direction or in the representation of land and sea surfaces can significantly degrade the accuracy of turbulence-related parameters.

For the radiation data, both outgoing shortwave radiation and outgoing longwave radiation are influenced by the presence of the feeding barge. As a result, these measurements do not provide sufficiently clean information from the sea to be used, for example, in estimating sea surface temperature. In contrast, the measurements of incoming shortwave radiation and incoming longwave radiation appear reliable. Comparison of the observed incoming shortwave radiation with model output reveals that the shadowing effect caused by the mountain is not adequately represented. Additionally, deficiencies in cloud cover representation in the model lead to a positive bias in shortwave radiation for both periods examined. For longwave radiation, a negative bias is observed, which may result from underrepresentation of low clouds and a model atmosphere that is too cold. During the second period, the model atmosphere is also too dry, potentially contributing to the negative bias in longwave radiation, whereas during the first period a small positive bias in relative humidity is present.

The verification results from this study generally show a negative temperature BIAS of approximately -0.5°C to -0.8°C in the model at this location, even after applying height correction to match the temperature measurement height (22 m) instead of using

the standard 2 m model output. Observed temperature fluctuations are well captured, as indicated by a correlation coefficient of 0.96 for both periods considered. For wind speed and wind gusts, there is generally a positive BIAS in both periods; however, the strongest winds tend to be underestimated. The importance of applying height correction when verifying pressure observations is highlighted by the change from a positive BIAS to a negative BIAS when comparing pressure calculated at 22 m height with mean sea level pressure. A correlation coefficient close to 1 (0.998) further demonstrates that the model accurately represents observed pressure fluctuations.

Finally, this study has identified that an emissivity value of 0.7, as used by the MINCOG model (Samuelsen et al., 2017) for estimating outgoing longwave radiation from 2 m temperature, may be appropriate during the cold season when assessing the impact of longwave radiative cooling in a spray-icing model. To the authors' knowledge, this represents the first evaluation of this parameter over an ocean surface in this region. The results clearly indicate that an emissivity of 1, as applied in studies such as Lozowski et al. (2000), while suitable for warmer temperatures, underestimates the radiative cooling effect in spray-icing models at temperatures below 0°C. In the spray-icing model presented by Kulyakhtin (2014), the longwave radiation cooling term is omitted based on the claim that it accounts for only 9% of the net cooling from sensible heat flux. However, the current findings suggest that the radiative cooling term is larger than previously assumed and should likely be included in such models. However, it may be preferable to use the outgoing longwave radiation directly from the model rather than relying on this simplified parameterization, in order to achieve a more accurate estimation of the longwave radiation term in a spray-icing model.

Acknowledgements

Gratitude goes to the Research Council of Norway for the financial support through the project “Multidisciplinary approach for spray icing modelling and decision support in the Norwegian maritime sector” (SPRICE). This project is funded under the MAROFF-2 Programme [Grant Number: 320843]. Gratanglaks is also acknowledged for letting the SPRICE project use their facilities for conducting the measurements applied in the current study.

References

Bolton, D. 1980. The computation of equivalent potential temperature. *Monthly weather review*, 108(7):1046–1053. doi: 10.1175/1520-0493(1980)108<1046:TCOEPT>2.0.CO;2. URL http://dx.doi.org/10.1175/1520-0493(1980)108<1046:TCOEPT>2.0.CO;2.

Dhar, S., Naseri, M., Khawaja, H. A., Edvardsen, K., and Zhu, T. 2024. Design, development and deployment of a novel sea spray collector for sea-spray flux measurements. *Cold Regions Science and Technology*, 218:104096. ISSN 0165-232X. doi: https://doi.org/10.1016/j.coldregions.2023.104096. URL https://www.sciencedirect.com/science/article/pii/S0165232X23003270.

Gay, S., Justin; Landolt. Analyzing Accuracy of the Lufft WS600 in Remotely Measuring Precipitation Events. Poster, 2016. URL https://digitalcommons.calpoly.edu/star/374. Accessed 21 August 2025.

Jiménez, P. A. and Dudhia, J. 2013. On the ability of the wrf model to reproduce the surface wind direction over complex terrain. *Journal of Applied Meteorology and Climatology*, 52(7):1610 – 1617. doi: https://doi.org/10.1175/JAMC-D-12-0266.1. URL https://journals.ametsoc.org/view/journals/apme/52/7/jamc-d-12-0266.1.xml.

Kulyakhtin, A. 2014. *Numerical Modelling and Experiments on Sea Spray Icing*. PhD thesis, NTNU - Norwegian University of Science and Technology. [Available online at http://hdl.handle.net/11250/277036 Accessed 29 June 2017.].

Køltzow, M., Casati, B., Bazile, E., Haiden, T., and Valkonen, T. 2019. An nwp model intercomparison of surface weather parameters in the european arctic during the year of polar prediction special observing period northern hemisphere 1. *Weather and Forecasting*, 34(4):959 – 983. doi: https://doi.org/10.1175/WAF-D-19-0003.1. URL https://journals.ametsoc.org/view/journals/wefo/34/4/waf-d-19-0003_1.xml.

Lozowski, E. P., Szilder, K., and Makkonen, L. 2000. Computer simulation of marine ice accretion. *Philosophical Transactions of the Royal Society of London. Series A:*

Mathematical, Physical and Engineering Sciences, 358(1776):2811–2845. doi: 10.1098/rsta.2000.0687. URL https://doi.org/10.1098/rsta.2000.0687.

Lufft. 2022. User Manual Smart Weather Sensors. techreport 50, OTT HydroMet Fellbach GmbH, Fellbach, Germany.

Mathisen, T. I. 2023. User guideturbulence predictions at norwegian airports. techreport 1, Norwegian Meteorological Institute, Oslo, Norway. URL https://www.ippc.no/ippc/help/UserGuide-TurbulencePredictionsatNorwegianAirports(Englishversion1.0).pdf. Accessed 21 August 2025.

Müller, M., Batrak, Y., Kristiansen, J., Køltzow, M. A. , Noer, G., and Korosov, A. 2017. Characteristics of a convective-scale weather forecasting system for the european arctic. *Monthly Weather Review*, 145(12):4771 – 4787. doi: https://doi.org/10.1175/MWR-D-17-0194.1. URL https://journals.ametsoc.org/view/journals/mwre/145/12/mwr-d-17-0194.1.xml.

Newman, S. M., Smith, J. A., Glew, M. D., Rogers, S. M., and Taylor, J. P. 2005. Temperature and salinity dependence of sea surface emissivity in the thermal infrared. *Quarterly Journal of the Royal Meteorological Society*, 131(610):2539–2557. doi: https://doi.org/10.1256/qj.04.150. URL https://rmets.onlinelibrary.wiley.com/doi/abs/10.1256/qj.04.150.

Pereira, D. Wind rose, 2023. URL https://www.mathworks.com/matlabcentral/fileexchange/47248-wind-rose. Accessed 21 August 2025.

Samuelsen, E. M. 2017. *Prediction of ship icing in Arctic waters – Observations and modelling for application in operational weather forecasting*. PhD thesis, UiT – The Arctic University of Norway, Tromsø. http://hdl.handle.net/10037/11801 Accessed 21 August 2025.

Samuelsen, E. M., Edvardsen, K., and Graversen, R. G. 2017. Modelled and observed sea-spray icing in Arctic-Norwegian waters. *Cold Regions Science and Technology*, 134:54 – 81. ISSN 0165-232X. doi: https://doi.org/10.1016/j.coldregions.2016.11.002. URL http://www.sciencedirect.com/science/article/pii/S0165232X16303275.

The MathWorks Inc. MATLAB version: 9.14.0 (R2023a), 2023. URL https://www.mathworks.com. Accessed 21 August 2025.

Thies. 2022. Ultrasonic Anemometer 3D. Instruction for Use. 4.383x.xx.xxx. techreport 021507, Adolf Thies GmbH Co. KG, Hauptstraße 76 · 37083 Göttingen · Germany.